博 士 学 位 論 文

Doctoral Dissertation

Effect of conditional glass former oxides WO_3, Ga_2O_3, and

V_2O_5 addition on thermal stability and proton mobility of

proton-conducting phosphate glasses （プロトン伝導性リン酸塩

ガラスの熱安定性とプロトン移動度への条件付きガラス形成

酸化物 WO_3, Ga_2O_3, および V_2O_5 添加の効果）

東北大学大学院環境科学研究科

Graduate School of Environmental Studies, Tohoku University

先進社会環境学専攻　　　　　　　　　　　専攻 major ／
コース course

学籍番号 Student ID No.	C0GD1501
氏　名 Name	Aman Sharma

指　導　教　員 Supervisor at Tohoku Univ.	小俣孝久　教授	
研 究 指 導 教 員 Research Advisor at Tohoku Univ.	鈴木一誓　講師	
審　査　委　員 （○印は主査） Dissertation Committee Members Name marked with "○" is the Chief Examiner	○　　小俣孝久　教授	
	1　　川田達也　教授	2　　福山博之　教授
	3　　鈴木一誓　講師	4
	5	6

Table of Contents

Chapter 4 Experimental Investigation of Effect of V$_2$O$_5$ Addition on Proton Mobility and Thermal Stability in Proton-Conducting Phosphate Glasses 57

Chapter 5 Experimental Investigation of Effect of Ga$_2$O$_3$ Addition on Proton Mobility and Thermal Stability in Proton-Conducting Phosphate Glasses 79

Chapter 1 Introduction

1-1 Global warming and its consequences

Global warming is an ongoing and severe issue that poses catastrophic consequences for the planet. It stands as the most significant environmental challenge humanity is currently confronted with. One evident and immediate impact of global warming is the rise in the average global temperature. This rise is directly linked to human activities, specifically the increased concentration of greenhouse gases in the atmosphere since the industrial revolution. These gases trap heat and subsequently lead to elevated surface temperatures. The National Oceanic and Atmospheric Administration (NOAA) has reported that the global average temperature has increased by 0.8°C over the past century [1]. Since temperature records began in 1880, the hottest recorded year was 2016, with a temperature 0.99°C warmer than the mean of the previous fifty years [2].

Another prominent effect of global warming is the occurrence of extreme weather events in various regions worldwide. These events may include wildfires, in addition to unusual hot or cold weather patterns. For example, California experienced its largest, most destructive, and costliest wildfires between 2017 and 2019, despite not experiencing severe drought conditions [3]. Numerous published studies provide evidence of the devastating impact of global warming on human lives, costly damages, and ecosystems [4,5]. These destructive consequences are expected to escalate over time, potentially reaching a large scale. Therefore, it is crucial to take action and seek solutions that can mitigate long–term damages.

Conducting a thorough analysis of the fundamental causes is vital in order to identify the underlying issues. As previously mentioned, the primary cause of global warming is the presence of greenhouse gases, which contribute to the greenhouse effect. These gases, such as carbon dioxide (CO_2), methane (CH_4), nitrous oxide (N_2O), and etc., exist in the Earth's atmosphere. Due to their chemical properties, they absorb or reflect the infrared radiation emitted by warm surfaces, preventing it from escaping into space and causing the Earth's atmosphere to heat up [6]. Human activities, particularly since the advent of the industrial revolution in the late 18th century, have had a significant impact on the natural environment. Over the past century, the concentration of carbon dioxide (CO_2) in the atmosphere has notably increased, primarily due to the combustion of fossil fuels like coal, natural gas, and oil. Additionally, activities such as deforestation for industrial and agricultural purposes, marine pollution through ocean dumping, and environmental degradation from surface mining, all contribute to a decrease in the Earth's capacity to naturally absorb carbon dioxide (CO_2). These activities also contribute to global warming, although to a lesser extent. The Intergovernmental Panel on Climate Change (IPCC) report "Climate Change 2014-Mitigation of Climate Change" emphasizes that the burning of fossil fuels for energy and electricity generation, driven by rapid population and economic growth globally, has played a major role in this trend, particularly in recent decades [7].

Fossil fuels play a significant role in meeting industrial and domestic energy needs, powering various aspects of our lives such as homes, vehicles, and machinery. For example, Japan heavily relies on conventional energy sources like natural gas, petroleum products, and coal, which are imported from different countries [8]. In 2010, fossil fuels accounted for 81.7% of Japan's energy supply. However, this percentage increased by 5.7% in 2017 due to the Great East Japan Earthquake in 2011. This unfortunate natural disaster resulted in the destruction of the Fukushima Daiichi Nuclear power station, raising concerns about the safety of nuclear power generation in Japan. Consequently, most of the nuclear power plants in Japan were shut down, reducing nuclear power generation to 1.4% in 2017 from 11.2% in 2011. As a result, thermal power generation, which relies on fossil fuels, was increased to compensate for the nuclear power shortfall [8] (Figure 1−1). Therefore, it is not feasible to replace fossil fuels with nuclear energy as a power source in the near future.

Due to its limited domestic natural resources, Japan heavily depends on fossil fuel imports, which accounted for 87.4% of its supply in 2017. The country has always faced challenges in terms of its own oil and natural gas reserves. In the same year, Japan's energy self-sufficiency ratio was only 9.6%, significantly lower than that of other developed countries [9].
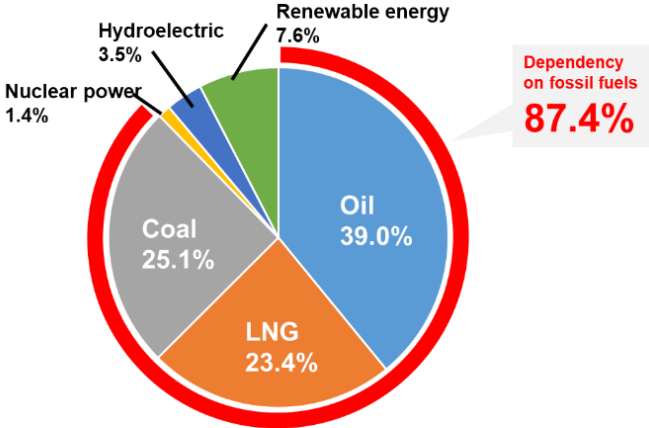
Figure 1-1 Japan`s domestic supply of primary energy, FY2017.

Over the past century, the burning of fossil fuels has had a severe impact on the environment and human health, contributing to air and water pollution, as well as global warming [10]. Fossil fuel consumption continues to rise each year, and it is expected that competition for these finite resources will intensify in the future. The significant increase in fossil fuel consumption can be attributed to the rapid economic growth and technological advancements in developed countries, as well as the emergence of economies like China and India. This has led to a substantial increase in global fossil fuel consumption. Following the nuclear tragedy in 2011, greenhouse gas emissions in Japan reached a peak of 1.4 billion tons in fiscal year 2013 [11]. Out of this total, approximately 1.2 billion tons consisted of carbon dioxide (CO_2) emissions from energy sources, with around 573 million tons attributed to electric

power generation, and the remainder from other sectors [12]. The CO_2 emissions from electric power generation alone accounted for about 40% of the total emissions in fiscal year 2013, highlighting the need for attention and action. However, emissions levels have been reduced since 2013, and in fiscal year 2017, greenhouse gas emissions dropped below the levels recorded in fiscal year 2010, before the Great East Japan Earthquake. Japan has been making continuous efforts to achieve emission reduction targets in line with energy policy standards comparable to other nations.

To address these challenges, several measures are being pursued in Japan:

- Development of highly efficient technologies to replace fossil fuel-based power generation and promote alternative energy sources that do not rely on fossil fuels.
- Improving Japan's energy self-sufficiency rate, which currently stands at less than 10%, by establishing and promoting new forms of unconventional energy for power generation.

One viable solution to these problems is the use of renewable energy, which has gained socio-economic importance and is actively promoted worldwide. Governments and energy policymakers are showing interest in harnessing solar power, wind power, geothermal energy, and hydroelectric power to combat the climate change crisis. However, it's important to note that these renewable energy sources have certain limitations, such as the requirement for large areas of land, specific weather conditions, and relatively low energy density. Additionally, challenges like community opposition and limited scalability can affect their ability to provide a constant power supply [12,13]. Nonetheless, these renewable energy sources remain crucial and play a supportive role in sustainable development efforts.

Fuel cell power generation stands out as a promising solution to overcome the limitations of renewable energy sources mentioned earlier, while also offering high energy density. The concept of fuel cells dates back to the mid-19th century when Sir William Grove introduced them as an energy conversion system. Subsequently, Professor Friedrich from the University of Basle made significant discoveries regarding fuel cells in 1829 [14]. However, their development did not progress significantly during the early stages due to the abundance and affordability of primary energy sources such as coal and oil. It was in the early 20th century, with the increasing demand for electricity and the transition from conventional to new energy sources, that fuel cells garnered substantial attention. Unlike thermal or nuclear power generation processes, which involve multiple energy conversions, fuel cells directly convert chemical energy into electrical energy, resulting in high power generation efficiency [15].

Figure 1−2 illustrates the schematic of a proton exchange membrane fuel cell, which uses a proton conductor as the electrolyte. The fuel, such as hydrogen, and oxygen do not collide at the anodic and cathodic sides, respectively, due to the separating electrolyte. At the anode, hydrogen is catalytically oxidized to produce protons and electrons. Since the electrolyte is a non-electronic conductor, the electrons flow through an external circuit from the anode to the cathode. Meanwhile, the protons migrate through the electrolyte to the cathode, where they react with oxygen and electrons to form water. The fuel cell's overall reaction involves the combination of hydrogen and oxygen to produce water, which is the sum of the anode and cathode reactions:

$$\text{Anode: } H_2(gas) \rightarrow 2H^+ + 2e^- \qquad\qquad E^{\circ}(anode) = 0 \qquad\qquad (1\text{--}1)$$

$$\text{Cathode: } \frac{1}{2}O_2(gas) + 2e^- + 2H^+ \rightarrow H_2O(liq.) \qquad E^{\circ}(cathode) = 1.229\,V \qquad (1\text{--}2)$$

$$\text{Overall: } 2H_2(gas) + O_2(gas) \rightarrow 2H_2O(liq.) \qquad E^{\circ}(cell) = 1.229\,V \qquad (1\text{--}3)$$

Nowadays, as the demand for electricity continues to rise, fuel cells have gained even more interest. The energy efficiency of thermal power generation through steam turbines is around 40% [16]. In contrast, fuel cells already exceed 40% efficiency [17]. Moreover, fuel cells can maintain high efficiency even at smaller scales of power generation, unlike conventional power generation methods. Since fuel cells do not require large spaces or complex machinery like thermal or nuclear power plants, their application can be expanded to distributed power sources, such as household co-generation systems, potentially reducing transmission losses. Another significant advantage of fuel cells is their minimal environmental impact. While conventional power generation sources emit harmful substances like carbon dioxide (CO_2), nitrogen oxides (NO_x), and sulfur oxides (SO_x), which contribute to air pollution, fuel cells do not emit any greenhouse gases into the atmosphere when hydrogen (H_2) is used as a fuel [18].
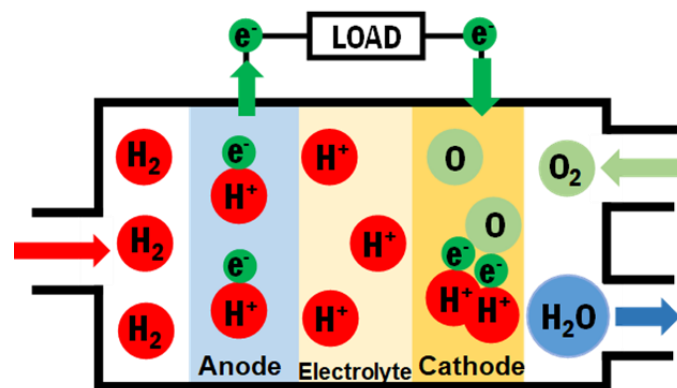
Figure1-2 Schematic of a proton exchange membrane fuel cell.

Fuel cells show great potential for powering automobiles/vehicles, aiming to improve the urban environment. Although hydrogen is being promoted as a fuel for fuel cells by governments and international organizations, its liquefaction presents challenges. As a result, the development of storage and transportation methods for hydrogen is still ongoing, and these challenges need to be addressed to meet the demands of a hydrogen society. Overcoming these technical hurdles is crucial. It is worth noting that fuel cells are not limited to hydrogen as their fuel source. Various fuels such as bio-alcohol or ammonia can also be utilized. These alternative fuels are easier to store and transport than hydrogen and contribute, albeit to a lesser extent, to reducing carbon dioxide emissions since they can be produced from biomass, thus promoting greater energy self-sufficiency. Currently, the primary focus of research and development in this power generation method is on fabricating more efficient fuel cells while simultaneously reducing production costs.

1-2 Types of fuel cells and their characteristics

Table 1−1 presents a list of various fuel cell types currently undergoing active development. The table includes information on key materials, operating temperatures, operational characteristics, and historical background.

Fuel cell systems are classified based on the type of electrolyte material used, which determines the temperature range, required catalysts, electrochemical reactions, and fuel requirements. The main types of fuel cells include Polymer Electrolyte Fuel Cell (PEFC), Phosphoric Acid Fuel Cell (PAFC), Molten Carbonate Fuel Cell (MCFC), and Solid Oxide Fuel Cell (SOFC) [19]. PAFC and MCFC use liquid-based electrolytes (phosphoric acid and molten carbonates, respectively), which can evaporate and corrode electrode materials, limiting their long-term operation [20,21]. On the other hand, PEFC and SOFC employ solid electrolytes and are actively researched. PEFC offers high power density, low weight, and volume compared to other fuel cells, but it requires expensive platinum (Pt) as a catalyst, adding to the system cost. It operates at room temperature to 80 °C [22,23]. SOFC, on the other hand, uses solid, non-porous compounds as electrolytes and achieves around 60% energy conversion efficiency. It operates at high temperatures (700 to 1000 °C), eliminating the need for expensive catalysts and allowing the use of a variety of fuels, which contributes to cost reduction [24]. However, SOFCs have drawbacks related to their high operating temperatures, such as slow startup and the need for expensive heat-resistant materials for system protection, making them more suitable for utility applications rather than transportation purposes [25].

A newly developed fuel cell technology that operates at intermediate temperatures ranging from 250 to 500 °C [26-29]. In the context of fuel cells, the temperature range of 250-500 °C is crucial because it allows for direct oxidation or splitting of biofuels into hydrogen using an integrated reformer. Therefore, this temperature range is strategically important as it enables efficient utilization of biofuels in fuel cell systems. The electrode kinetics are expected to be significantly enhanced, which could enable the use of non–noble metal catalysts. Compared to fuel cells with liquid electrolytes, solid proton conducting electrolytes offer several advantages. They are easier to handle, compact, suitable for mass production, and can be fabricated into thin films with excellent resistance to gas permeation. Compared to solid oxide fuel cells, the lower operational temperature of this intermediate temperature fuel cell (ITFCs) technology allows for a wider selection of materials for system construction and operation. Electrical conducting materials can include stainless steel, coated metals, graphite, and carbon composites, while non-conducting materials can include various types of thermal setting plastics, glass/ceramic fibers, and more. The compatibility of thermal expansion among these materials will be much less demanding due to lower operational temperature.

Table 1-1 Comparison of types of fuel cells and their working features

Types	Electrolytes (Charge carriers)	Catalysts (Anode/ Cathode)	Operating temp. / °C	Some technical features	Years of research	Ref.
Polymer Electrolyte Fuel Cell (PEFC)	Perfluorinated sulfonic acid membrane $(H_3O)^+$	Pt−C/Pt−C	60−80	+ High power density; rapid startup − Noble metal catalyst; CO intolerance	Since 1960s	[30-32]
Phosphoric Acid Fuel Cell (PAFC)	Concentrated H_3PO_4 (H^+)	Pt(Ru−C)/Pt −C	175−210	+ Suitable for stationary power generation; fuel flexibility − Slow kinetics and low power density; material corrosion; lifetime issues	1960s	[30]
Molten Carbonate Fuel Cell (MCFC)	Molten carbonate (CO_3^{2-})	Ni/NiO	550−650	+ Efficient fuel utilization; faster kinetics − Material corrosion; long startup times	Since late 1930s	[30]
Solid Oxide Fuel Cell (SOFC)	Solid oxides (O^{2-})	Ni/Perovskit es	700−900	+ No expensive catalysts required; faster kinetics; internal fuel reforming. − Slow startup; requires expensive heat–resistant materials	Since 1930s	[30]
Inorganic Proton Conductor Fuel Cell (PCFC)	CsH_2PO_4 (H^+)	Pt(WC)/Pt	200−300	+ Longer lifespan and lower cost; use various biofuels; potential use of non-noble catalyst. − Under early development	SAFC Since 1990s	[26]
	Proton conducting perovskites, tungstates, pyrochlores, $LaNbO_4$ and other families	-	400−700	+ Lower operation temperature and cost than existing SOFSs − poor chemical stability in H_2O and CO_2 containing atmosphere	-	[33]

In comparison with proton exchange membrane (PEM) fuel cells, this technology offers improved cell cooling and heat recovery. The elimination of a two-phase water system (liquid and vapor) simplifies system construction and operation. The enhanced electrode kinetics of this technology increase fuel flexibility for both mobile and stationary applications, which is crucial for power systems based on renewable biofuels. Importantly, the higher operational temperatures and improved electrode kinetics make the use of non-noble metal catalysts feasible. Integrating the fuel cell stack with fuel processors becomes possible, leading to advanced features such as higher efficiency, smaller size, lighter weight, simplified construction, and operation, as well as cost-effectiveness in terms of capital and operation. Therefore, the realization of intermediate-temperature fuel cells is essential to promote the widespread use of fuel cells. Currently, the biggest barrier to the realization of ITFCs is the lack of electrolyte materials that exhibit high protonic conductivity in the intermediate temperature range. The temperature range of 250−500 °C is commonly referred to as the "Norby gap" (Figure 1−3) and represents a technological gap that has attracted significant research interest [34-35]. In fuel cells, the electrolyte's charge carriers should either be the reactant or product of the electrode reactions to prevent concentration polarization at the electrodes. Proton (H^+) or oxide ion (O^{2-}) are commonly used, and in some cases, ions containing protons (such as ammonia NH_4^+ or H_3O^+ on Nafion® membranes) or oxide ions (such as CO_3^{2-} in molten carbonates) can be utilized [36]. For intermediate temperature fuel cells (ITFCs), two main types of solid ion-conductive electrolytes are considered: oxide ion conductors and proton

conductors as discussed above. However, oxide ion conductors face limitations due to the strong Coulomb force between the divalent oxide ions and cations, resulting in low conductivity. Proton conductors, on the other hand, have monovalent charge carriers and offer higher conductivity in the desired temperature range [37]. Proton conductors are particularly attractive for ITFCs due to their low operating temperatures (between 250 °C and 500°C), which are suitable for both chemical reactions and energy conversion processes, leading to cost reduction and longer lifespan for interconnecting materials [38]. When aiming for intermediate temperature operation, proton conductors are considered the most suitable electrolyte materials.
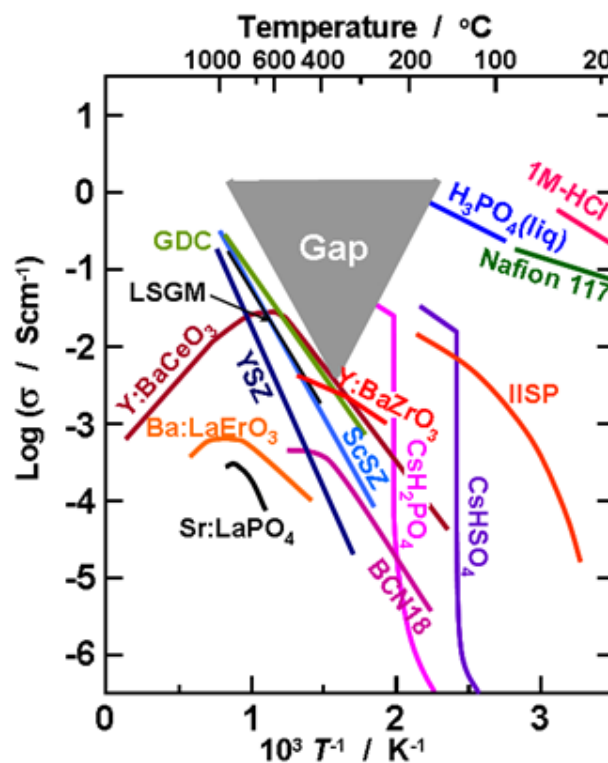

Figure 1-3 Conductivity as a function of inverse temperature represents so called the "Norby gap".

Kreuer et al has highlighted two main difficulties in the development of proton conductor systems operating in the intermediate temperature range [39].

- The first challenge is related to the limited number of compound families that have been reported to exhibit proton conductivity. The compounds capable of accommodating protons are restricted to specific families of compounds, which restricts the options for developing new materials with proton conductivity [39].

- The second problem involves the inherent properties of the species responsible for proton conductivity. These properties impose constraints on the operational temperature range and the chemical and electrochemical stability of the materials when in contact with other materials. To further advance the available materials for practical applications, it is necessary to optimize all

7

relevant properties, taking into consideration both high and low temperature proton conducting materials [39].

As shown in Figure 1–3, polymer electrolyte membranes (PEMs) have been developed for fuel cell operation at temperatures below 100 °C, and YSZ, LSGM, and GDC have been developed for operation at temperatures above 600 °C, which have proton or oxide ion conductivities higher than 1×10^{-2} S cm^{-1}, which is required for fuel cell electrolytes. In contrast, no electrolyte material has yet been found that exhibits high conductivity in the intermediate-temperature range of 250–500 °C [34].

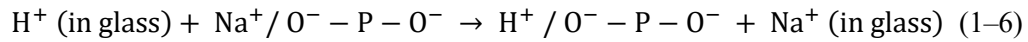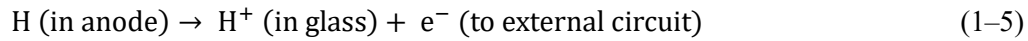## 1-3 Proton-conducting solid electrolytes suitable for ITFCs

Several high protons-conducting electrolytes have been reported. Solid acid compounds like CsH_2PO_4 and $CsHSO_4$ have shown protonic conductivity of approximately 1×10^{-2} S cm^{-1} at 200 °C [40−41]. CsH_2PO_4, in particular, has been used as an electrolyte in prototype fuel cell operations, achieving a maximum power density of 415 mW cm^{-2} at 240 °C, which is comparable to the available market maximum power density of single cells in cylindrical flat plate SOFCs [42]. However, CsH_2PO_4 suffers from dehydration above 230 °C and solubility in water, leading to a loss of proton conductivity and poor thermal and chemical stability, which limits its long-term stability in fuel cells [43].

Another class of proton conductors is Y_2O_3-doped $BaZrO_3$ (BZY) and Y_2O_3-doped $BaCeO_3$ (BCY), which are perovskite-type oxides. BZY and BCY exhibit conductivity ranging from 10^{-2} to 10^{-1} S cm^{-1} at temperatures of 500−600 °C, and prototype fuel cell testing achieved a power density of 335 mW cm^{-2} at 500 °C [44]. However, BZY and BCY develop hole conduction under oxidizing atmospheres, leading to energy efficiency reduction due to leakage current within the electrolyte [45−46]. The search for a suitable electrolyte material for intermediate temperature fuel cells (ITFCs) is still ongoing. The ideal electrolyte material should possess high conductivity in the intermediate–temperature range, excellent thermal stability, and high proton mobility. Currently, no material has been identified that fulfills all these criteria. Therefore, the development of a new electrolyte material remains a crucial task in advancing ITFC technology. Researchers continue to explore novel materials and conduct extensive studies to identify a material that can meet the requirements for an efficient and durable electrolyte in ITFCs.

Proton conductivity has also been observed in oxide glasses, where protons are held as OH groups in the glass structure. Phosphate glasses, in particular, have shown higher proton mobility due to the strong hydrogen bonding in the OH groups compared to silicate or borate glasses [47−48]. Efforts have been made to enhance the proton concentration in glass, as the conventional melt-quench method, which usually takes place at around 1200−1300 °C results in low proton conductivity due to the small proton concentration, typically around 10^{19-20} cm^{-3}. One approach to improve proton concentration is through low-temperature melting, where glass is melted at temperatures lower than usual. For example, $ZnO−P_2O_5$ glasses melted at around 800 °C have achieved higher proton concentrations of about 8×10^{20}

cm^{-3} [49]. However, this method is limited to compositions with high P$_2$O$_5$ content, restricting the search range for suitable compositions and limiting the conductivity to around 1×10^{-3} S cm^{-1} at maximum [49]. Another technique involves the sol-gel synthesis of ZrO$_2$−P$_2$O$_5$ glasses, which have demonstrated very high proton conductivity of approximately 1×10^{-2} S cm^{-1} at room temperature [50]. However, these glasses tend to dehydrate and lose their proton carriers at temperatures above 60 to 100 °C. Phosphate glasses produced using low-temperature synthesis methods such as low-temperature melting, and sol-gel suffer from limitations in composition range and the instability of protons at intermediate temperatures. These factors make it challenging to achieve high proton conductivity in the intermediate temperature range using these methods.

Recently, a new approach called the Alkali-Proton Substitution Method (APS method) has been developed by Ishiyama et al. [51]. In this method, a phosphate glass containing Na$^+$ ions are used as a precursor, and protons are electrochemically substituted into the glass. The APS substitution reaction proceeds by injecting protons into alkali glass, and it has shown promise in increasing proton concentration in glass electrolytes. The AP substitution reaction proceeds according to the following equation:

$$\frac{1}{2}H_2 \text{(in atmosphere)} \rightarrow H \text{ (in anode)} \tag{1–4}$$

$$H \text{ (in anode)} \rightarrow H^+ \text{ (in glass)} + e^- \text{ (to external circuit)} \tag{1–5}$$

$$H^+ \text{ (in glass)} + Na^+/O^- - P - O^- \rightarrow H^+/O^- - P - O^- + Na^+ \text{ (in glass)} \tag{1–6}$$

$$Na^+ \text{ (in glass)} + e^- \text{ (from external circuit)} \rightarrow Na \text{ (in cathode)} \tag{1–7}$$

The AP (Alkali-Proton) substitution method involves a specific process to inject protons into a glass electrolyte. The schematic diagram in Figure 1−4 illustrates the AP substitution reaction. The precursor glass contains Na$^+$ ions (Figure 1-4(i)). A palladium (Pd) anode is deposited to the upper surface, while a molten Sn cathode that dissolves metallic Na is attached to the lower surface of the glass sample. When a direct current (DC) voltage is applied between these surfaces in a hydrogen atmosphere, a potential difference is created. Specifically, when the top surface is positively charged, hydrogen dissolved in the anode (*Eq*. 1−4) undergoes oxidation to form protons (*Eq*. 1−5). These protons are then injected into the glass. The injected protons push Na$^+$ ions deeper into the glass in a pile-up manner (*Eq*. 1−6). Excess Na$^+$ ions on the cathode side are reduced by gaining electrons and discharged out of the glass (*Eq*. 1−7). This process continues as long as the mobility of the injected protons is sufficiently high, leading to the replacement of all Na$^+$ ions with protons in the glass (Figure 1−4).
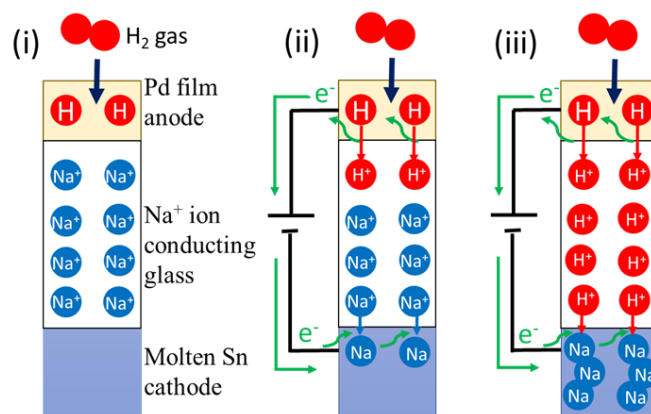
Figure 1-4 Schematic illustration of Alkali Proton Substitution (APS)

By using a precursor glass with a high concentration of Na ions, the AP substitution method enables the injection of a very high proton concentration, ranging from 10^{21} to 10^{22} cm^{-3} [51−54]. This surpasses the capabilities of conventional methods. In addition, as mentioned earlier, glasses synthesized at low temperatures by the sol-gel method lose proton carriers above 60~100 °C, but since AP substitution is usually performed at around 300 °C, the injected protons remain stable in the glass until around 300°C. Because of these advantages, proton-conducting phosphate glasses prepared by AP substitution are expected to exhibit high proton conductivity in the intermediate-temperature range. [51-54]. Ishiyama et al. successfully fabricated proton-conducting glasses using the AP substitution method. They used a precursor glass, such as the $35NaO_{1/2}−1WO_3−8NbO_{5/2}−5LaO_{3/2}−51PO_{5/2}$ glass (referred to as 1W glass) [53].

The AP substitution method offers the potential to realize high thermal stability and high proton mobility in the intermediate temperature range, essential for the application of proton-conducting glasses as electrolytes in fuel cells. The method allows for the fabrication of glasses with a wide range of compositions, and the suppression of softening, phase separation, and crystallization can be achieved by adjusting the chemical composition, leading to enhanced thermal stability. While high proton mobility is yet to be fully explored, the AP substitution method holds promise in achieving high proton carriers' concentration.

1-4 Relationship between oxides components vs. thermal stability and proton mobility in the proton–conducting phosphate glasses

Our group have previously reported that the mobility of proton carriers (μ_H) in a glass is influenced by the glass structure and the types of component oxides, such as glass network modifiers and intermediate oxides [55−57]. It has been observed that the proton mobility in phosphate glasses increases with the development of glass framework depolymerization. This occurs because the energy barrier for proton migration decreases as the depolymerization progresses. However, it has also been found that the

proton mobility starts to decrease when pyrophosphate ions ($P_2O_7^{4-}$) become a major component in the glass [58]. This decrease is attributed to the strong trapping of protons by $P_2O_7^{4-}$, leading to a high energy barrier for proton dissociation. In pseudo-binary systems composed of network modifier oxides and $PO_{5/2}$, it has been noted that the composition of a glass with $P_2O_7^{4-}$ as a major component corresponds to an oxygen-to-phosphorus (O/P) ratio of 3.5.

The type of network modifier or intermediate oxide is another factor affecting proton mobility. Previous research examined the proton mobility of glasses containing MgO and BaO as network modifiers (in the composition $35HO_{1/2}-5RO-3NbO_{5/2}-3LaO_{3/2}-2GeO_2-2BO_{3/2}-50PO_{5/2}$, where R represents Mg or Ba). It was found that the glass containing BaO exhibited thrice the proton mobility compared to the glass containing MgO. Characterization of O−H and P−O bonding using infrared absorption and X-ray photoelectron spectroscopy indicated that glasses containing network modifiers with low electronegativity, which are electronically positive, demonstrated higher proton mobility. This is attributed to the relatively larger ionicity of O−H bonds in glasses containing BaO compared to those containing MgO [57].

The reported results indicated that the substitution of alkali ions with protons in precursor glasses through the APS leads to a decrease in the glass transition temperature (T_g) by approximately 150−200°C [52-53]. This is because protons, with a coordination number of one, do not anchor the phosphate glass networks like alkali ions do. To maximize T_g, it was suggested to design the precursor glass composition with an adequate amount of network modifiers and intermediate oxides [59]. Components such as alkaline-earth oxides, Al_2O_3, Y_2O_3, La_2O_3, WO_3, Nb_2O_5, and Ta_2O_5 should be included in the glass composition. These components remain in the glass after the APS and contribute to raising T_g.

Based on the understanding obtained, Yamaguchi et al reported on the proton conductivity of a specific glass composition, $36HO_{1/2}-4NbO_{5/2}-2BaO-4LaO_{3/2}-4GeO_2-1BO_{3/2}-49PO_{5/2}$, prepared using the APS method [59]. This glass exhibited a proton conductivity of 1×10^{-3} S cm^{-1} at 280 °C. However, this conductivity level is still insufficient for the practical application of phosphate glasses in ITFCs. Typically, electrolytes used in fuel cells require an electrical conductivity higher than 1×10^{-2} S cm^{-1}. Therefore, it is necessary to further increase the proton conductivity to enable the use of proton-conducting phosphate glasses as electrolytes in ITFCs.

Previous investigation revealed that the mobility of proton carriers (μ_H) at the glass transition temperature (T_g) in the phosphate glasses remained relatively constant within a narrow range of 2×10^{-9} to 2×10^{-7} cm^2 V^{-1} s^{-1}, corresponding to a proton diffusion coefficient of approximately 4×10^{-10} cm^2 s^{-1} [60]. This almost constant diffusion coefficient at the T_g can be explained by the weak bonding of the glass network through hydrogen bonds and glass framework is barely preserved by the bridging hydrogen bonds. The glass transition temperature (T_g) of the proton-conducting glasses varies significantly, ranging from 150 to 650 °C. Similarly, the proton conductivity at 200 °C exhibits a wide range, spanning from 10^{-10} to 10^{-4} S cm^{-1}, while the concentration of proton carriers falls between 10^{19} and 10^{22} cm^{-3} [60]. Because the measured μ_H at T_g of the 36H-glass is 5.4×10^{-8} cm^2 V^{-1} s^{-1}, which falls

within the range of μ_H at T_g ranging from 2×10^{-9} to 2×10^{-7} cm^2 V^{-1} s^{-1}. This suggests that there is a possibility to further increase its proton conductivity by improving the μ_H at T_g. However, the exact determining factor of μ_H at T_g in proton conducting phosphate glasses has not been identified yet, and therefore, we currently lack the understanding of how to enhance μ_H at T_g.

The highest μ_H at T_g presumed in the proton-conducting phosphate glasses was approximately 2×10^{-7} cm^2 V^{-1} s^{-1}. Using the APS technique, the proton concentration (n_H) of around 10^{22} cm^{-3} can be achieved. Based on the relationship $\sigma_H = n_H \times e \times \mu_H$, the highest expected proton conductivity at T_g is estimated to be 3×10^{-4} S cm^{-1} [60]. Unfortunately, the current proton conductivity of the phosphate glass electrolyte falls below the threshold required for practical fuel cell applications. It is necessary to raise the operating temperature above the glass transition temperature (T_g). By increasing the working temperature above T_g, the proton conductivity can be enhanced. To enhance thermal stability, conditional glass former components such as Nb$_2$O$_5$, Ta$_2$O$_5$, MoO$_3$, WO$_3$, and V$_2$O$_5$ can be added to the glass composition. These components play a crucial role in strengthening the glass framework by tightly bridging the phosphate chains. By incorporating these conditional glass formers, the overall stability of the glass structure can be improved, allowing for higher operating temperatures and enhanced proton conductivity.

The successful description of proton conductivity in relation to the glass composition holds significant potential for improving the proton conductivity of phosphate glasses. By utilizing the established relationship between glass composition vs. μ_H at T_g and T_g, it will be easier to enhance the proton conductivity of these glasses. This advancement can have a substantial impact on the performance of electrochemical cells, including fuel cells, operating at intermediate temperatures.

1-5 Purpose of this study

The proton mobility and thermal stability of phosphate glasses were found to be influenced by both the glass structure and the oxide components present in the composition. However, a comprehensive understanding of these relationships is currently lacking. Gaining insights into these connections is crucial for enhancing proton mobility and thermal stability and facilitating the search for optimal glass compositions. With this context in mind, the objective of this thesis study was to establish a clear relationship between glass compositions, proton mobility, and thermal stability in proton-conducting phosphate glasses. The following steps were taken to achieve this objective:

1. Firstly, the study aimed to establish a correlation between the glass composition and two key parameters: μ_H at T_g and T_g. This was accomplished by employing a statistical analysis approach. Through careful analysis of the results, it was discovered that two oxide components, specifically WO$_3$ and GeO$_2$, played a significant role in simultaneously enhancing both μ_H at T_g and T_g. These oxides were found to strengthen the connections between phosphate chains in the glass, resulting in a three-

dimensional glass structure. This structural enhancement is believed to contribute to the observed improvements in proton conductivity within the glass electrolyte.

2. Building upon the findings mentioned above, the study sought to investigate the effect of oxide components addition on the μ_H at T_g and T_g in phosphate glass compositions. It has been reported that when conditional glass formers oxides were introduced into the glass composition, they tended to form strong cross-linking between the phosphate chains by creating P−O−M (M = conditional glass formers) heteroatomic linkages. To investigate this further, three specific conditional glass formers, namely WO_3, V_2O_5, and Ga_2O_3, were selected for experimental analysis. The goal was to examine the effect of their addition on μ_H at T_g and T_g and provide the information to optimize the glass compositions to design high proton-conducting phosphate glasses for future study.

1-6 Structure of this paper

This paper consists of Chapters 1 to 6 as outlined below:

Chapter 1 presents an overview of fuel cells' advantages over other power generation systems and explores the current state and challenges of intermediate-temperature fuel cells, considered the next-generation solution. The chapter outlines the challenges to obtain the high proton conducting phosphate glasses and understanding the relationship between the glass compositions vs. μ_H at T_g and T_g, hold promise to improve proton-conductivity in phosphate glasses.

Chapter 2, I employed a statistical analysis approach using a linear regression model to establish correlations between the composition of phosphate glasses and two key parameters: μ_H at T_g and T_g. The analysis revealed that the inclusion of two specific oxide components, WO_3 and GeO_2, played a significant role in simultaneously enhancing both μ_H at T_g and T_g. These oxides are reportedly known to strengthen the connections between phosphate chains with strong cross-linking, resulting in a three-dimensional glass structure. This highlights the crucial role of such cross-linking oxides in improving thermal stability and proton mobility.

Chapter 3, It was predicted that WO_3 is favorable components in phosphate glasses, which enhance both the μ_H and T_g, from the linear regression model. Therefore, we focused on the experimental investigation of WO_3 as an oxide component to enhance both proton mobility and thermal stability in xW-glass compositions ($35NaO_{1/2}−xWO_3−8NbO_{5/2}−5LaO_{3/2}−(52−x)PO_{5/2}$, where $x = 2, 4, 6$, and 8) after conducting APS. The substitution of WO_3 for $PO_{5/2}$ led to increased T_g and μ_H at T_g, validating the predictions of our linear regression model made in chapter 2. The elevated T_g was attributed to the presence of P−O−W linkages that strongly bridged the phosphate chains, while the improved μ_H at T_g was associated with enhanced proton migration paths through non-bridging oxygens (NBOs) within WO_6 octahedra. These results indicated towards the oxides, known for their strong cross-linking capability between phosphate chains and high coordination number in the glass can play a vital role in enhancing both thermal stability and proton mobility in the glass composition.

Chapter 4, chapter 3 clarified that addition of WO_3 into the glass compositions provided strong cross-linking between the phosphate chains, leading to enhanced thermal stability and proton mobility, simultaneously. WO_3 is widely recognized as a conditional glass former, known to make strong cross-linking between the phosphate chains. Similarly, V_2O_5 is also recognized as a conditional glass former that contributes to cross-linking through P−O−V linkages and highly coordinated in the glass. Therefore, I focused on investigating the effects of V_2O_5 on the thermal stability and proton mobility of phosphate glasses. The specific composition $30NaO_{1/2}−20VO_{3/2}−50PO_{5/2}$ after conducting APS was studied. Although, the addition of $VO_{5/2}$ into the glass usually results in electronic conduction, luckily the glass after APS was pure proton conductor. The experimental results confirmed the high T_g, enhancement can be attributed to the formation of tight cross-linkages between the phosphate ion chains through the formation of P−O−V heteroatomic linkages involving 6-fold coordinated vanadium (V) atoms. However, despite the positive influence on T_g, the addition of $VO_{5/2}$ in the glass composition led to low proton mobility. This can be attributed to the strong trapping of protons by NBOs related to V^{4+} or V^{5+} units (VO_x polyhedra) resulting in high proton dissociation energy. Similar to the case of WO_3, the increased T_g was attributed to the presence of P−O−V linkages that tightly bridged the phosphate chains. However, unlike the WO_3 case, the high μ_H was not observed.

Chapter 5, In previous chapters, the addition of WO_3 and V_2O_5 into the glass compositions provided strong cross-linking between the phosphate chains, leading to enhanced thermal stability. WO_3 facilitates proton transport, while V_2O_5 hampers it by trapping protons at VO_x polyhedra's oxygen sites, increasing dissociation energy and lowering proton mobility. Therefore, in the 3rd approach, I chose Ga_2O_3, also recognized as a conditional glass former that contributes to cross-linking through P−O−Ga linkages and highly coordinated in the glass. Building upon this knowledge, I further investigated the effect of Ga_2O_3 addition in xGa-glass compositions ($30NaO_{1/2}−xGaO_{3/2}−6NbO_{5/2}−(6−x)GeO_2−58PO_{5/2}$, where $x = 0, 2, 4,$ and 6) after conducting APS. Substituting GeO_2 with $GaO_{3/2}$ resulted in a significant increase in μ_H at T_g, while T_g showed a slight increase. The rise in T_g was attributed to P−O−Ga linkages tightly bridging the phosphate chains. In $GaO_{3/2}$, IR spectra indicated slightly stronger O-H bonding than the GeO_2 case, suggesting limited proton mobility when substituted with GeO_2. However, XPS analysis revealed more covalent P−O bonding, implying increased ionic O−H bond in −Ga−O−P−O−H linkages, leading to higher proton mobility. Overall, the reduced E_a and direct observation of O−H bond through IR spectra suggested reduced energy barrier for proton migration based on proton hopping mechanism. These findings emphasize the differences observed compared to the case of WO_3 but underscore the significance of conditional glass formers in improving both the thermal stability and proton mobility of phosphate glasses.

Chapter 6 concludes the thesis; The incorporation of specific conditional glass former oxides, namely WO_3, Ga_2O_3, and V_2O_5, has been found to have a significant impact on the thermal stability and proton mobility of proton-conducting phosphate glasses. These oxides act as strong cross-linking agents, leading to the formation of robust linkages between phosphate chains and the creation of a more three-

dimensional glass structure. As a result, the thermal stability of the glasses improves, as indicated by higher glass transition temperatures (T_g). Investigations into the mechanisms underlying the increase in μ_H at T_g have revealed interesting findings. For WO_3, the formation of $\equiv$P$-$O$-$W$-$O$-$P$\equiv$ linkages, utilizing the non-bridging oxygen (NBOs) of WO_6 units, provides pathways for enhanced proton migration. This leads to improved proton mobility in the glass. Similarly, Ga_2O_3 contributes to increased μ_H at T_g, although the exact mechanism is still unknown. Tentatively, this increase in proton mobility is attributed to a reduction in energy barrier for proton migration. However, the inclusion of $VO_{5/2}$ units in the glass composition has been observed to hinder μ_H at T_g. This can be attributed to the formation of $\equiv$P$-$O$-$V$-$O$-$P$\equiv$ linkages utilizing the NBOs of VO_x polyhedral associated with Vanadium (V) ions. The V$-$O$-$H bonds in these units exhibit strong proton trapping characteristics, resulting in low proton mobility. The choice of oxide components in proton-conducting phosphate glasses plays a crucial role in determining their properties. Overall, this research highlights the significance of conditional glass formers in designing high-performance phosphate glasses for intermediate-temperature fuel cells, contributing to the advancement of this next-generation power generation solution.

References

1. NOAA National Centers for Environmental Information 2018 State of the Climate: Global Climate Report for Annual 2017.
2. J. Hansen, D. Johnson, A. Lacis, S. Lebedeff, P. Lee, D. Rind, G. Russell, Science, 1981, **213,** 957–66.
3. Anon https://www.fire.ca.gov/incidents/2020.
4. N. Nauslar, J. Abatzoglou, P. Marsh, Fire, 2018, **1,** 18.
5. J. Callaghan, Trop. Cyclone Res. Rev., 2018, **7,** 164–71.
6. W. C. Wang, J. P. Pinto, Y. L. Yung, J. Atmos. Sci., 1980, **37,** 333–338.
7. R. P. M. E. Ottmar, S. Youba, J. C. Minx, E. Farahani, S. Kadner, K. Seyboth, A. Adler, I. Baum, S. Brunner, P. Eickemeier, B. Kriemann, J. Savolainen, S. Schlömer, T. Z. C. von Stechow, Climate Change 2014: Mitigation of Climate Change Cambridge, United Kingdom, New York, USA.
8. V. Vivoda, Energy Policy, 2012, **46,** 135–143.
9. Agency for Natural Resources and Energy- 2019 Edition Brochures.
10. A. Demirbas, Energy Sources, 2004, **26,** 225–36.
11. N. Greenhouse, G. Emissions, F. Year, P. Figures, E. Summary, M. Co, 2016 Japan's total greenhouse gas emissions in fiscal year (FY), **2016,** 1–4.
12. A. Evans, V. Strezov, T. J. Evans, Renew. Sustain. Energy Rev., 2009, **13,** 1082–1088.
13. M. D. Tarhan, J. Entrep. Organ. Divers., 2015, **4,** 104–120.
14. U. Bossel, European Fuel Cell Forum: Oberrohrdorf, 2000.
15. C. Santoro, C. Arbizzani, B. Erable, I. Ieropoulos, J. Power Sources, 2017, **356,** 225–244.
16. T. Ganapathy, N. Alagumurthi, R. P. Gakkhar, K. Murugesan, J. Eng. Sci. Technol. Rev., 2009, **2,** 123–130.
17. C. De Servi, S. Campanari, A. Tizzanini, C. Pietra, J. Eng. Gas Turbines Power, 2013, **135,** 1–11.
18. L. E. Klebanoff, J. W. Pratt, C. M. Leffers, K. T. Sonerholm, T. Escher, J. Burgard, S. Ghosh, Transp. Res. Part D Transp. Environ., 2017, **54,** 250–268.
19. Energy.gov. https://www.energy.gov/eere/fuelcells/types-fuel-cells.
20. N. Sammes, R. Bove, K. Stahl, Solid State Mater. Sci., 2004, **8,** 372–378.
21. K. Joon, J. Power Sources, 1996, **61,** 129–33.
22. L. Schlapbach, Nature, 2009, **460,** 809–811.
23. J. Tollefson, Nature, 2010, **464,** 1262–1264.
24. S. C. Singhal, Solid State Ionics, 2000, **135,** 305–313.
25. A. Weber, E. Ivers-Tiffée, J. Power Sources, 2004, **127,** 273–283.
26. C. R. I. Chisholm, D. A. Boysen, A. B. Papandrew, S. Zecevic, S. Cha, K. A. Sasaki, A. Varga, K. P. Giapis, S. M. Haile, Electrochem. Soc. Interface, 2009, **18**, 53-59.
27. D. J. L. Brett, A. Atkinson, N. P. Brandon, S. J. Skinner, Chem. Soc. Rev., 2008, **37,** 1568–1578.
28. B. Zhu, J. Power Sources, 2001, **93,** 82–86.
29. J. P. P. Huijsmans, F. P. F. Van Berkel, G. M. Christie, J. Power Sources, 1998, **71** 107–110.
30. J. M. Andujar, F. Segura, Renew. Sustain. Energy Rev., 2009, **13,** 2309–2322.
31. J. H. Wee, Renew. Sustain. Energy Rev., 2007, **11,** 1720–1738.
32. C. Stone, A. E. Morrison, Solid State Ionics, 2002, **152-153,** 1–13.
33. A. K. Azad, A. M. Abdalla, A. Afif, A. Azad, S. Afroze, A. C. Idris, J. Y. Park, M. Saqib, N. Radenahmad, S. Hossain, I. B. Elius, M. Al-Mamun, J. Zaini, A. Al-Hinai, M. S. Reza, J. T. S. Irvine, Sci. Rep., 2021, **11**, 19382.
34. T. Norby, Solid State Ionics, 1999, **125,** 1–11.
35. G. Harley, R. Yu, L.C. De Jonghe, Solid State Ionics, 2007, **178**, 769–773.
36. A. D. Chen, K. Du, W. Li, B. Deng, W. Li, H. Yin, D. Wang, J. Electroanal. Chem., 2022, **925**, 116900.

37. K. Huang, A. Zampieri, M. Ise, J. Electrochem. Soc., 2010, **157,** B1471.

38. A. Smirnova, Mater. Fuel Cells, 2008, 386–424.

39. K. D. Kreuer, Solid State Ionics, 1997, **97**, 1–15.

40. T. Uda, S. M. Haile, Solid-State Lett., 2005, **8,** 245–247.

41. V. G. Ponomareva, N. F. Uvarov, G. V. Lavrova, E. F. Hairetdinov, Solid State Ionics, 1996, **90,** 161–166.

42. 科学技術振興機構 低炭素社会戦略センター「低炭素社会づくりのための総合戦略とシナリオ」，p.30-34，平成24年7月.

43. M. S. Haile, C. R. I. Chisholm, K. Sasaki, D. A. Boysen, T. Uda, Faraday Discuss., 2007, **134** 17–39.

44. C. Duan, J. Tong, M. Shang, S. Nikodemski, M. Sanders, S. Ricote, A. Almansoori, R. O'Hayre, Science, 2015, **349** 1321–1326.

45. K. Nomura, H. Kageyama, Solid State Ionics, 2007, **178,** 661–665.

46. D. Han, Y. Noda, T. Onishi, N. Hatada, M. Majima, T. Uda, Int. J. Hydrogen Energy, 2016, **41,** 14897–14908.

47. Y. Abe, H. Shimakawa, L. Hench, J. Non. Cryst. Solids, 1982, **51,** 357–365.

48. G. Harley, L.C. De Jonghe, Solid State Ionics, 2010*,* **181,** 424–429.

49. H. Sumi, Y. Nakano, Y. Fujishiro, T. Kasuga, Solid State Sci., 2015, **45**, 5-8.

50. Y . Abe, G . Li, M. Nogami, T. Kasuga , L. L. Hench, J. Electrochem. Soc., 1996, **143**, 144-147.

51. T. Ishiyama, S. Suzuki , J. Nishii, T. Yamashita, H. Kawazoe, T. Omata , J. Electrochem. Soc., 2013, **160**, E143-E147.

52. T. Ishiyama, S. Suzuki , J. Nishii, T. Yamashita, H. Kawazoe, T. Omata, Solid State Ionics, 2014, **262**, 856-859.

53. T. Ishiyama, J. Nishii, T. Yamashita, H. Kawazoe, T. Omata, J. Mater. Chem. A, 2014, **2**, 3940-3947.

54. K Kawaguchi , T . Yamaguchi , T Omata, T . Yamashita H. Kawazoe J Nishii , Phys. Chem. Chem. Phys., 2015, **17**, 22855-22861.

55. T. Yamaguchi, T. Ishiyama, K. Sakuragi, J. Nishii, T. Yamashita, H. Kawazoe and T. Omata, Solid State Ionics, 2015, **275**, 62-65.

56. T. Yamaguchi, T. Ishiyama, K. Sakuragi, J. Nishii, T. Yamashita, H. Kawazoe, N. Kuwata, J. Kawamura and T. Omata, Solid State Ionics, 2016, **288**, 281-285.

57. T. Yamaguchi, Y. Saito, Y. Kuwahara, H. Yamashita, T. Ishiyama, J. Nishii, T. Yamashita, H. Kawazoe and T. Omata, J. Mater. Chem. A, 2017, **5**, 12385-12392.

58. T. Yamaguchi, T. Kataoka, S. Tsukuda, T. Ishiyama, J. Nishii, T. Yamashita, H. Kawazoe and T. Omata, Phys. Chem. Chem. Phys., 2017, **19**, 29669-29675.

59. T. Yamaguchi, S. Tsukuda, T. Ishiyama, J. Nishii, T. Yamashita, H. Kawazoe and T. Omata, J. Mater. Chem. A, 2018, **6**, 23628–23637.

60. T. Omata, T. Yamaguchi, S. Tsukuda, T. Ishiyama, J. Nishii, T. Yamashita and H. Kawazoe, Phys. Chem. Chem. Phys., 2019, **21**, 10744–10749.

Chapter 2 Understanding the Effect of Oxide Components on Proton Mobility and Thermal Stability in Phosphate Glasses

2-1 Introduction

In chapter 1, The research has uncovered a fascinating finding concerning the mobility of proton carriers (μ_H) in phosphate glasses at the glass transition temperature (T_g). The reported glasses exhibit a wide range of T_g values, spanning from 150 to 650 °C. Additionally, the proton conductivity at 200 °C displays a broad range of 10^{-10} to 10^{-4} S cm^{-1}, while the proton carrier concentration ranges between 10^{19} and 10^{22} cm^{-3} [1]. Notably, I have observed that the values of μ_H converge within a narrow range of 2×10^{-9} to 2×10^{-7} cm2 V^{-1} s^{-1} [1]. Remarkably, the 36H-glass demonstrates an μ_H at T_g value of 5.4×10^{-8} cm^2 V^{-1} s^{-1}, which lies in the middle of the observed μ_H range between 2×10^{-9} to 2×10^{-7} cm^2 V^{-1} s^{-1}. Based on this finding, it is suggested that by further improving the μ_H at T_g, the proton conductivity of the 36H-glass may be enhanced. However, a clear understanding of the main determining factors that affect μ_H at T_g in proton-conducting phosphate glasses is currently lacking. Consequently, effective strategies to enhance μ_H at T_g are still elusive.

Unlike crystalline materials, the composition of glasses can be continuously adjusted. As a result, various glass properties have been empirically described using weighted averages of the mole fractions of their respective components [2-4]. However, while it is important to comprehend the impact of fundamental properties such as O−H bonding, local structure surrounding protons, and short-range atomic structure of the glass framework on μ_H at T_g for a better understanding of proton conduction in phosphate glasses, it is also valuable to establish a relationship between glass composition and μ_H at T_g to enhance the performance of proton conducting phosphate glasses as electrolytes.

If I can successfully correlate proton mobility with glass composition, it will become easier to improve the proton conductivity of phosphate glasses by leveraging the established relationship between composition and μ_H at T_g. This achievement would have a significant impact on intermediate-temperature electrochemical cells, including fuel cells and steam electrolysis cells. Previous studies on proton conducting phosphate glasses prepared using the alkali-proton substitution (APS) method have involved multiple oxide components [1]. For instance, the 36H-glass incorporates eight oxides: $HO_{1/2}$, $NaO_{1/2}$, BaO, $LaO_{3/2}$, $NbO_{5/2}$, GeO_2, $BO_{3/2}$, and $PO_{5/2}$ [5]. Consequently, comprehending the role of individual oxide components on μ_H at T_g and the relationship between composition and μ_H at T_g is challenging.

To address these challenges, I have developed a statistical model that utilizes a descriptive approach to elucidate the μ_H at T_g of phosphate glasses based on their composition. I employed the mol% of respective component oxides as descriptors. Furthermore, I have also developed a model to describe T_g, as the thermal stability of proton conducting glasses is another crucial property, particularly when

considering the operating temperature of electrochemical devices involving these glasses. By analysing the obtained model, I discussed the influence of individual component oxides on μ_H at T_g and T_g itself.

2-2 Methodology

2-2-1 Dataset details

The training dataset for the measurement of μ_H at T_g and T_g values of proton conducting phosphate glasses employed in this study is sourced from a previous research report [1,5,6-12]. I worked with a dataset that consisted of the remaining 19 records [1,5,6-12], as summarized in Table 2-1. Each record in this dataset provided information on the glass composition in mol% as well as the experimentally determined μ_H at T_g and T_g. By making these adjustments to the original dataset, I aimed to focus specifically on records where the proton carriers were genuinely representative of the glass composition, thereby ensuring the reliability and relevance of the training data.

Table 2-1 Training dataset of the relationship between the glass compositions and the proton mobility μ_H at T_g and T_g.

	mol% of component oxide																
No.	$HO_{1/2}$	$NaO_{1/2}$	WO_3	$NbO_{5/2}$	$TaO_{5/2}$	MgO	BaO	$LaO_{3/2}$	$AlO_{3/2}$	$YO_{3/2}$	$GdO_{3/2}$	GeO_2	$BO_{3/2}$	$PO_{5/2}$	μ_H at T_g (cm^2 V^{-1} s^{-1})	T_g (°C)	Ref.
1	25	3	1	8	0	0	0	5	0	0	0	0	0	58	2.1×10^{-9}	200	6
2	24	8	1	8	0	0	0	5	0	0	0	0	0	54	5.5×10^{-9}	177	6
3	25	10	1	8	0	0	0	5	0	0	0	0	0	51	3.7×10^{-8}	190	7
4	32	6	1	8	0	0	0	5	0	0	0	0	0	48	3.7×10^{-8}	170	6
5	32	8	1	8	0	0	0	5	0	0	0	0	0	46	1.2×10^{-8}	167	6
6	28	2	1	8	0	0	0	5	3	3	0	0	0	50	2.0×10^{-8}	281	8
7	29	6	1	8	0	0	0	5	3	0	0	0	0	48	7.6×10^{-9}	224	8
8	30	5	1	8	0	0	0	5	0	3	0	0	0	48	4.1×10^{-9}	228	8
9	35	0	0	3	0	5	0	3	0	0	0	2	2	50	1.3×10^{-8}	192	9
10	32	3	0	3	0	0	5	3	0	0	0	2	2	50	6.8×10^{-9}	163	9
11	34	2	0	4	0	0	2	4	0	0	0	4	1	49	5.4×10^{-8}	180	5
12	38	2	0	0	4	2	0	4	0	0	0	2	1	47	2.7×10^{-8}	165	1
13	17	8	0	0	0	0	0	8	0	0	0	1	0	66	2.6×10^{-9}	227	10
14	12	13	0	0	0	0	0	6	0	0	0	6	0	63	1.3×10^{-8}	243	1
15	33	2	0	0	0	2	0	5	0	0	0	5	0	53	4.0×10^{-8}	182	1
16	31	4	0	0	0	2	0	0	0	0	5	5	0	53	1.2×10^{-8}	178	1
17	20	5	0	0	0	0	0	6	0	0	0	6	0	63	1.5×10^{-8}	252	11
18	28	7	0	0	0	2	0	0	0	0	5	5	0	53	1.4×10^{-8}	233	11
19	34	1	8	8	0	0	0	5	0	0	0	0	0	44	1.1×10^{-7}	231	12

2-2-2 Regression models and method

In this study, a linear combination model was employed to predict both log (μ_H at T_g) and T_g, using the mol% of respective oxides as predictors. The regression algorithm used for this analysis was based on linear regression as implemented in MATLAB (MathWorks, USA). Initially, I utilized a general linear

combination model that incorporates the mol% composition of individual oxides as predictors for both log (μ_H at T_g) and T_g, overtraining occurred due to the limited number of training data. The resulting model for log (μ_H at T_g) is presented as follows:

$$\log (\mu_H \text{ at } T_g) = -0.236388563x(\text{HO}_{1/2}) - 0.21732199x(\text{NaO}_{1/2}) - 0.128502192x(\text{WO}_3)$$
$$+ 0.671171102x(\text{NbO}_{5/2}) + 1.029198044x(\text{TaO}_{5/2}) + 1.374093231x(\text{MgO})$$
$$+ 1.306366399x(\text{BaO}) + 1.971135165x(\text{LaO}_{3/2}) - 0.201698121x(\text{AlO}_{3/2}) -$$
$$0.284685842x(\text{YO}_{3/2}) + 1.859907493x(\text{GdO}_{3/2}) + 0.754725434x(\text{GeO}_2) -$$
$$0.629475199x(\text{BO}_{3/2}) - 0.293206847x(\text{PO}_{5/2}) \tag{2-1}$$

Figure 2-1 displays a comparison between the experimentally observed values and the predicted values of μ_H at T_g. The root mean square error (RMSE) was calculated to be 0.2278, indicating a reasonably small deviation. However, as illustrated in Figure 2-2, the predicted values of log (μ_H at T_g) for the 55,296 phosphate glass compositions Ire found to be implausible, ranging from 10^{-29} to 10^{17} cm^2 V^{-1} s^{-1}, while the experimentally observed values fall within the range of 2×10^{-9} to 2×10^{-7} cm^2 V^{-1} s^{-1} [1]. This discrepancy suggests that overtraining may have occurred, potentially due to the limited number of training data available.

To address this issue, I employed principal components analysis (PCA) to fit a linear regression model and avoid overtraining. Five principal components Ire utilized, explaining 95% of the variance in the original data. The mathematical model can be expressed as follows:

$$log\left(\mu_H \text{ at } T_g \ /cm^2\,V^{-1}s^{-1}\right) = a_0 + \sum_{n=1}^{5} a_n PC_n \tag{2-2}$$

$$T_g/ \ °C = b_0 + \sum_{n=1}^{5} b_n PC'_n \tag{2-3}$$

$$PC_n = \sum_i c_i x_i \tag{2-4}$$

where PC_n and PC'_n represent the nth principal component explaining the variance of experimentally observed log (μ_H at T_g) and T_g, respectively. The model includes intercepts a_0 and b_0, coefficients a_n and b_n associated with each principal component, mol% of oxide i denoted as x_i, and its coefficient c_i. To validate the models and understand the effect of respective component oxides on μ_H at T_g and T_g, I performed predictions for 55,296 glass compositions. These compositions included various amounts of HO$_{1/2}$ (30, 33, and 36 mol%), WO$_3$ (0, 2, and 4 mol%), NbO$_{5/2}$ (0, 2, 4, and 6 mol%), MgO (0, 2, 4, and 6 mol%), BaO (0, 2, 4, and 6 mol%), LaO$_{3/2}$ (0, 2, 4, and 6 mol%), GeO$_2$ (0, 1, 2, 3, 4, and 5 mol%), BO$_{3/2}$ (0, 1, 2, and 3 mol%), and PO$_{5/2}$ (28-70 mol%). It is important to note that in these predictions, all compositions Ire assumed to form homogeneous glasses. This approach allowed us to examine the validity of the models and gain insights into the impact of different component oxides on μ_H at T_g and T_g within the specified scope of the study.

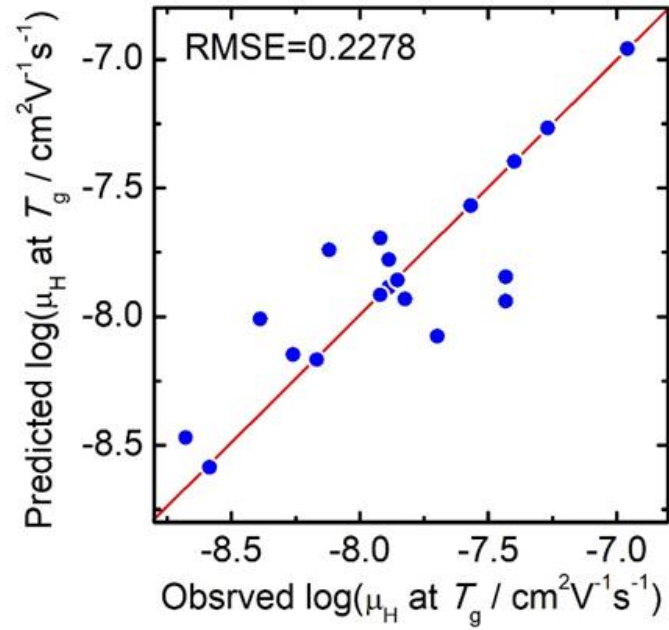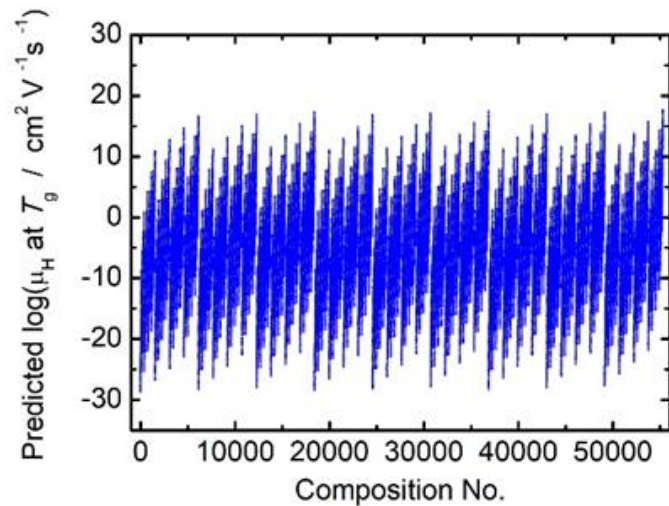**Figure 2-1** Comparison of experimentally observed and predicted values of μ_H at T_g.

Figure 2-2 Predicted values of log (μ_H at T_g) for the 55,296 phosphate glass compositions.

2-3 Results and discussion

2-3-1 Linear regression models for μ_H at T_g and T_g

After performing regression analysis, the relationships between log (μ_H at T_g) and T_g with the five principal components of glass composition were determined as follows:

$$\log (\mu_H \text{ at } T_g) = -7.8549 + 0.022233 \times PC_1 + 0.01167 \times PC_2 +$$
$$0.26874 \times PC_3 + 0.01727 \times PC_4 + 0.160456 \times PC_5 \qquad (2\text{-}5)$$

$$T_g = 204.368 - 1.622 \times PC'_1 + 1.282 \times PC'_2 - 2.350 \times PC'_3 + 7.897$$
$$\times PC'_4 + 5.630 \times PC'_5 \qquad (2\text{-}6)$$

The specific principal components for log (μ_H at T_g) and T_g are summarized in Tables 2-2 and 2-3, respectively.

Figure 2-3(a) and (b) depict a comparison between experimentally observed and predicted values of μ_H at T_g and T_g for the 19-training data. The root mean square error (RMSE) was calculated as 0.2775 for log (μ_H at T_g) and 23.6 °C for T_g. No systematic error was observed, and the fitting appeared reasonably good for both log (μ_H at T_g) and T_g.

Table 2-2 Five principal components obtained from the analysis of μ_H at T_g.

Principal components		PC_1	PC_2	PC_3	PC_4	PC_5
Proportion of variance		0.659	0.0183	0.061	0.026	0.021
Cumulative proportion		0.659	0.842	0.903	0.929	0.950
Factor loading	$x(HO_{1/2})$	0.69239	−0.32693	−0.07750	−0.19571	−0.15439
	$x(NaO_{1/2})$	−0.24549	0.28854	0.71623	−0.35865	−0.03489
	$x(WO_3)$	0.06837	0.15986	−0.11444	0.32222	0.77387
	$x(NbO_{5/2})$	0.16670	0.68417	−0.16598	0.28247	−0.30664
	$x(TaO_{5/2})$	0.02694	−0.5991	0.00355	−0.24336	0.04874
	$x(MgO)$	0.03954	−0.18457	0.01768	0.06160	−0.13778
	$x(BaO)$	0.02319	−0.04547	−0.02005	−0.12335	−0.09325
	$x(LaO_{3/2})$	−0.08309	0.19943	−0.33952	−0.50726	0.26128
	$x(AlO_{3/2})$	0.01281	0.06277	−0.04134	0.08739	−0.09090
	$x(YO_{3/2})$	0.01467	0.05828	−0.05950	0.09692	−0.09979
	$x(GdO_{3/2})$	−0.00319	−0.15212	0.31784	0.52266	−0.11954
	$x(GeO_2)$	−0.10164	−0.37370	0.21746	0.08717	0.28694
	$x(BO_{3/2})$	0.02654	−0.05917	−0.04343	−0.10435	−0.08555
	$x(PO_{5/2})$	−0.63774	−0.25119	−0.41100	0.07224	−0.24811

Table 2-3 Five principal components obtained from the analysis of T_g.

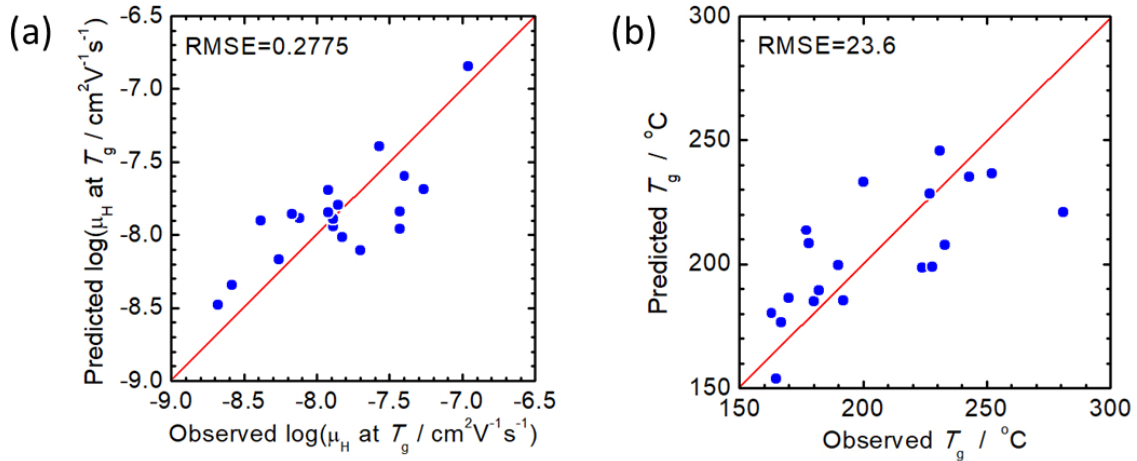| Principal components		PC_1	PC_2	PC_3	PC_4	PC_5
Proportion of variance		0.659	0.0183	0.061	0.026	0.021
Cumulative proportion		0.659	0.842	0.903	0.929	0.950
Factor loading	$x(HO_{1/2})$	0.69239	−0.32693	−0.07750	−0.19571	−0.15439
	$x(NaO_{1/2})$	−0.24549	0.28854	0.71623	−0.35865	−0.03489
	$x(WO_3)$	0.06837	0.15986	−0.11444	0.32222	0.77387
	$x(NbO_{5/2})$	0.16670	0.68417	−0.16598	0.28247	−0.30664
	$x(TaO_{5/2})$	0.02694	−0.5991	0.00355	−0.24336	0.04874
	$x(MgO)$	0.03954	−0.18457	0.01768	0.06160	−0.13778
	$x(BaO)$	0.02319	−0.04547	−0.02005	−0.12335	−0.09325
	$x(LaO_{3/2})$	−0.08309	0.19943	−0.33952	−0.50726	0.26128
	$x(AlO_{3/2})$	0.01281	0.06277	−0.04134	0.08739	−0.09090
	$x(YO_{3/2})$	0.01467	0.05828	−0.05950	0.09692	−0.09979
	$x(GdO_{3/2})$	−0.00319	−0.15212	0.31784	0.52266	−0.11954
	$x(GeO_2)$	−0.10164	−0.37370	0.21746	0.08717	0.28694
	$x(BO_{3/2})$	0.02654	−0.05917	−0.04343	−0.10435	−0.08555
	$x(PO_{5/2})$	−0.63774	−0.25119	−0.41100	0.07224	−0.24811

Figure 2-3 Comparison of experimentally observed and predicted values of (a) log (μ_H at T_g) and (b) T_g.

Figures 2-4 (a) and (b) illustrate the predicted values of log (μ_H at T_g) and T_g, respectively, for the 55,296 phosphate glass compositions. The predicted values for μ_H at T_g ranged between 8.1×10^{-10} to 7.7×10^{-7} cm^2 V^{-1} s^{-1}, while the predicted values for T_g ranged between 152 and 256 °C. Comparing these predicted values with the experimentally determined μ_H at T_g values [1], it is evident that the predicted range closely matches the range of the experimentally observed values, which fall between 2×10^{-9} to 2×10^{-7} cm^2 V^{-1} s^{-1}. These results indicate the reasonableness and applicability of the obtained models for discussing the effects of respective component oxides on μ_H at T_g.
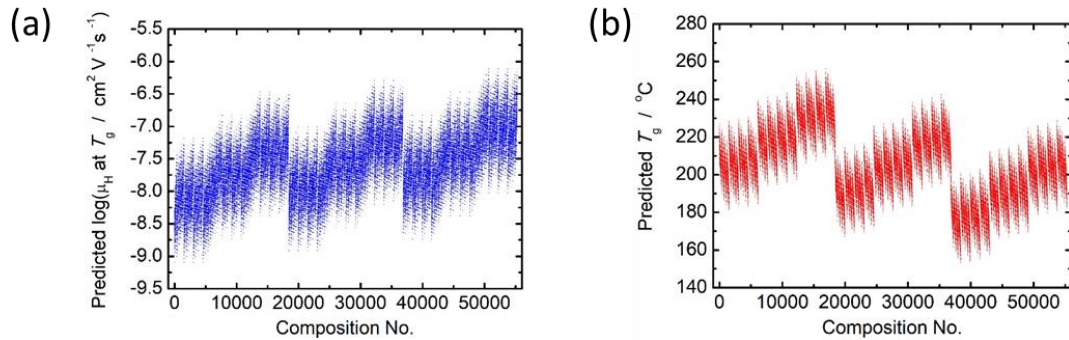
Figure 2-4 Predicted values of (a) log (μ_H at T_g) and (b) T_g for the 55,296 phosphate glass compositions.

Table 2-2 reveals that the absolute values of the factor loadings for $HO_{1/2}$ and $PO_{5/2}$ components are particularly larger than those of the other components. This indicates that the concentration of $HO_{1/2}$ and $PO_{5/2}$ primarily determines μ_H at T_g. Additionally, considering the positive coefficient of PC_1 in equation (2-5), it indicates that μ_H at T_g increases with increasing $HO_{1/2}$ concentration and decreases with increasing $PO_{5/2}$ concentration. This observation aligns well with the experimental finding that μ_H increases as the polymerization level of the phosphate glass network decreases. However, the linear regression model fails to reproduce the decrease in μ_H at higher O/P ratios (oxygen-to-phosphorus

23

atomic ratio) beyond 3.5-3.6 [13]. Consequently, the applicable composition range of the present model is limited to O/P ratios smaller than 3.5-3.6.

Comparing the models for μ_H at T_g and T_g, as summarized in Tables 2-2 and 2-3, it is surprisingly observed that the factor loadings of the principal components are the same for both log (μ_H at T_g) and T_g. This indicates a clear relationship between log (μ_H at T_g) and T_g, as the variance in both log (μ_H at T_g) and T_g is explained by the same principal components.

These recent findings align well with our previous estimations, which proposed that the movement of protons (proton diffusion or mobility), governs the behavior of the glass framework, specifically its glass transition temperature (T_g), in proton conducting phosphate glasses [6]. Figure 2-5 presents log (μ_H at T_g) as a function of T_g for the predicted values of 55,296 compositions (black dots) along with the 19 experimentally observed values (red dots). A clear linear trend is observed for the predicted values, indicating a decrease in log (μ_H at T_g) with increasing T_g. Although this relationship between log (μ_H at T_g) and T_g could be a crucial factor in understanding the determination of μ_H at T_g, further information is required to delve deeper into this aspect. Therefore, the origin of the relationship between log (μ_H at T_g) and T_g remains an open question and is not further discussed in this chapter.
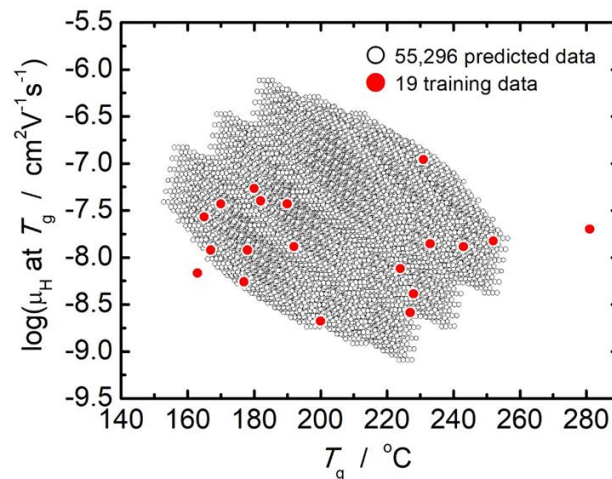
Figure 2-5 Plot of log (μ_H at T_g) as a function of T_g of 55,296 predicted values (open black dots) together with the experimentally observed 19 values (closed red dots).

2-3-2 Effects of respective component oxides on μH at Tg and Tg

In the previous section, I established a clear relationship between log (μ_H at T_g) and T_g. In this regard, I examined the effect of each component oxide and analyzed the distribution of predicted values in Figure 4. Figure 4(a) presents 55,296 predicted values for glasses with varying concentrations of $HO_{1/2}$, divided into three parts. Figure 4(b) displays 18,432 predicted values for glasses with 30 mol% of $HO_{1/2}$, categorized based on WO_3 concentration. Figure 4(c) shows 6,144 predicted values for glasses with 30 mol% of $HO_{1/2}$ and 0 mol% of WO_3, divided into four parts according to $LaO_{3/2}$ concentration. Figures

4(d) to 4(h) illustrate 1,536 predicted values for glasses with 30 mol% of $HO_{1/2}$, 0 mol% of WO_3, and 0 mol% of $LaO_{3/2}$, categorized based on the concentration of specific oxide components (MgO, BaO, $NbO_{5/2}$, $BO_{3/2}$, and GeO_2). The observations when adding the respective component oxides to the glass by substituting $PO_{5/2}$ are summarized as follows:

✓ Increasing $HO_{1/2}$ concentration leads to a decrease in T_g by 5°C per 1 mol% of $HO_{1/2}$ and an increase in log (μ_H at T_g) by 0.06 per 1 mol% of $HO_{1/2}$.

✓ Increasing WO_3 concentration results in an increase in both T_g and log (μ_H at T_g) by 6.5°C and 0.08 per 1 mol% of WO_3, respectively.

✓ With increasing $LaO_{3/2}$ concentration, T_g decreases by 2.2°C per 1 mol% of LaO3/2, while log (μ_H at T_g) increases by 0.1 per 1 mol% of $LaO_{3/2}$.

✓ Similar to $HO_{1/2}$ and $LaO_{3/2}$, the addition of MgO, BaO, and $BO_{3/2}$ causes T_g to decrease and log (μ_H at T_g) to increase. The variations are approximately -1.5°C and 0.05 per 1 mol% of MgO, -2.4°C and 0.05 per 1 mol% of BaO, and -2.2°C and 0.05 per 1 mol% of $BO_{3/2}$, respectively.

✓ $NbO_{5/2}$ concentration has little influence on the relationship between log (μ_H at T_g) and T_g, with T_g increasing by 0.7°C per 1 mol% of $NbO_{5/2}$ and log (μ_H at T_g) remaining constant regardless of $NbO_{5/2}$ concentration.

✓ In the case of GeO_2, both T_g and log (μ_H at T_g) increase, similar to WO_3. However, the increase in T_g is much smaller at 0.6°C per 1 mol% of GeO_2 compared to 6.5°C per 1 mol% of WO_3. On the other hand, the increase in log (μ_H at T_g) is slightly larger at 0.12 per 1 mol% of GeO_2 compared to 0.08 per 1 mol% of WO_3.

These observations and relationships are summarized in Table 2-4.

The observed effects of component oxides can be categorized into three groups based on their impact on μ_H at T_g and T_g. Group 1 includes $HO_{1/2}$, MgO, BaO, $LaO_{3/2}$, and $BO_{3/2}$, which increase μ_H at T_g but decrease T_g with increasing concentrations. Group 2 consists of WO_3 and GeO_2, which increase both μ_H at T_g and T_g as their concentrations increase. Group 3 comprises $NbO_{5/2}$, which increases T_g without affecting μ_H at T_g. These categorizations provide valuable insights for designing purpose-specific glasses.

The effect of each group oxide on T_g can be explained by glass structural chemistry. Group 1 oxides, excluding $BO_{3/2}$, act as glass modifiers, breaking the phosphate glass network and reducing T_g [14]. Among the group 1 oxide components, $BO_{3/2}$ is considered a glass-former and can exist in the glass as both trigonal planar BO_3 units and tetrahedral BO_4 units in the studied phosphate glasses [15-17]. However, when trigonal planar BO_3 units are introduced into the glass as an alternative to the PO_4 tetrahedra, it leads to a reduction in the number of bridging oxygens within the glass network. As a result, $BO_{3/2}$ acts as a glass modifier, similar to other group 1 oxides that possess glass-modifying properties, and its influence on T_g is comparable to that of other glass-modifying oxides. Groups 2 and 3 consist of oxides with high glass-forming ability. GeO_2 is a glass former, while WO_3 and $NbO_{5/2}$ are conditional glass formers [18]. When these oxides substitute for $PO_{5/2}$, GeO_6, WO_6 and NbO_6 octahedra reinforce the phosphate glass network, leading to an increase in T_g [19-21].
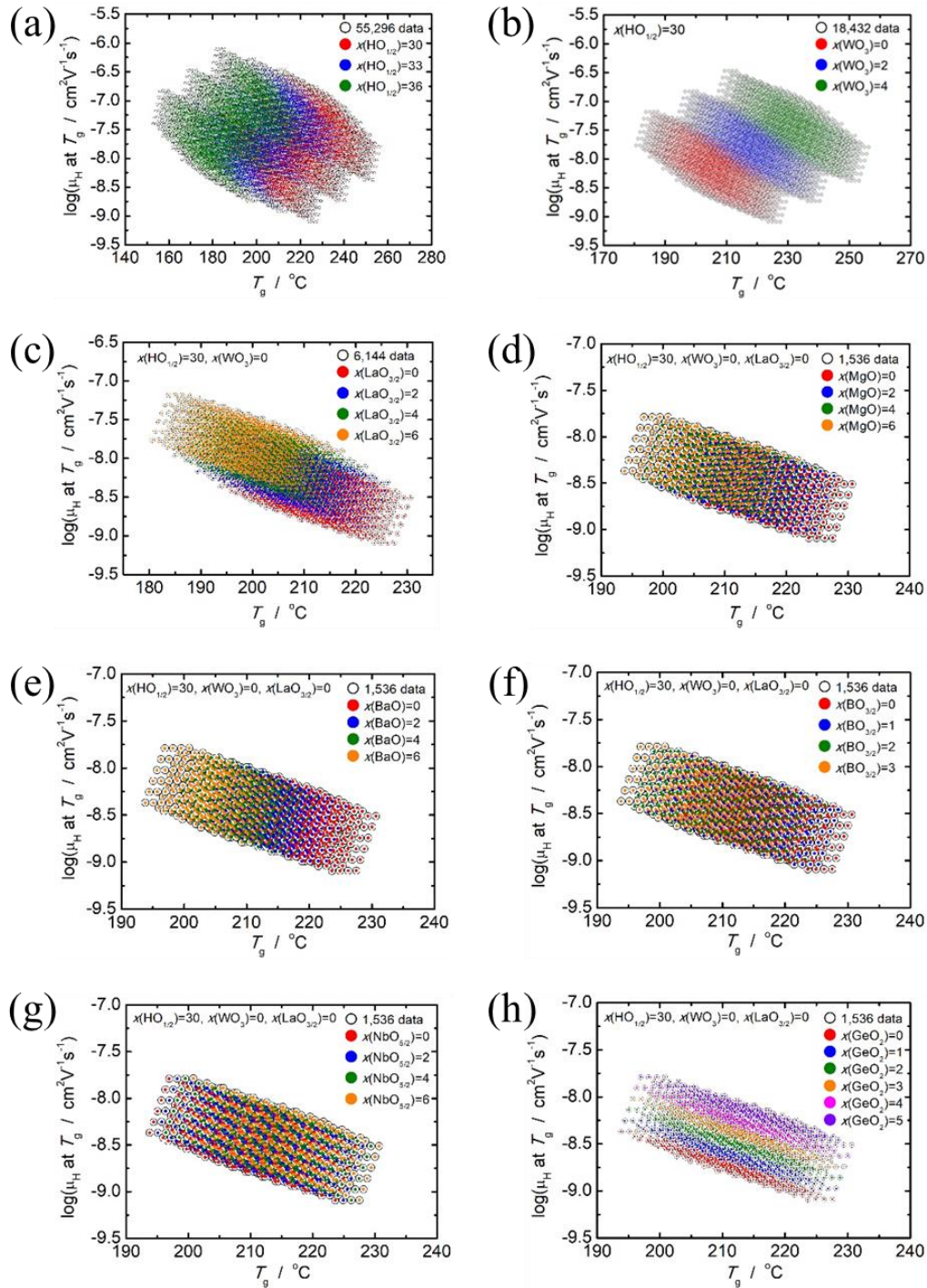
Figure 2-6 Distribution of the relationship between predicted values of log (μ_H at T_g) and T_g depending on the concentration of respective component oxides. (a) 55,296 predicted values distinguished by the $HO_{1/2}$ concentration (red dots = 30 mol% $HO_{1/2}$, blue dots = 33 mol% $HO_{1/2}$ and green dots = 36 mol% $HO_{1/2}$), (b) 18,432 predicted values for the glasses with 30 mol% of $HO_{1/2}$ distinguished by the WO_3 concentration (red dots = 0 mol% WO_3, blue dots = 2 mol% WO_3 and green dots = 4 mol% WO_3), (c) 6,144 predicted values for the glasses with 30 mol% of $HO_{1/2}$ and 0 mol% of WO_3 distinguished by the $LaO_{3/2}$ concentration (red dots = 0 mol% $LaO_{3/2}$, blue dots = 2 mol% $LaO_{3/2}$, green dots = 4 mol% $LaO_{3/2}$ and orange dots = 6 mol% $LaO_{3/2}$), (d), (e), (f), (g) and (h) 1,536 predicted values for the glasses with 30 mol% of $HO_{1/2}$, 0 mol% of WO_3 and 0 mol% of $LaO_{3/2}$ respectively distinguished by the concentration of MgO, BaO, $BO_{3/2}$, $NbO_{5/2}$ and GeO_2.

Table 2-4 Variation of log (μ_H at T_g) and T_g with the increasing component oxide by 1 mol%

			Group 1			Group 2		Group 3
Component oxide		MgO	BaO	LaO$_{3/2}$	BO$_{3/2}$	WO$_3$	GeO$_2$	NbO$_{5/2}$
Variation per 1 mol% of oxide	log (μ_H at T_g)	0.05	0.05	0.10	0.05	0.08	0.12	0.00
	T_g / °C	−1.5	−2.4	−2.2	−2.2	6.5	0.6	0.7

The origin of the effect on μ_H at T_g for group 1 can be understood, while for group 2 remains an open question and for group 3, it remains constant. The explanation for the effect of group 1 oxides is as follows. An illustrative example is the presence of BaO in the glass composition, the increased proton mobility, indicated by weaker O−H bonding, in Ba-containing glasses can be attributed to the highly ionic nature of Ba−O bonding [18]. In particular, the highly ionic Ba–O bonding in Ba–O–P≡ induces covalent P–O bonding in the phosphate network, which results in comparatively ionic O–H bonding in ≡P–O–H. The O–H bonding is weakened with increasing ionicity in O–H bonding; consequently, the proton carriers of the glass containing BaO with highly ionic Ba–O bonding exhibit higher mobility. The effect oxide components on the proton mobility can be applied to other modifiers of group 1. Glasses containing less electronegative modifiers exhibit higher mobility of proton carriers.

In a recent study [19], to gain insights into the role of GeO$_2$ on the thermal stability and proton mobility of proton-conducting phosphate glasses was investigated through experimental study. To conduct the study, proton-conducting phosphate glasses with an approximate composition of 22HO$_{1/2}$−3NaO$_{1/2}$−(12−x)LaO$_{3/2}$−xGeO$_2$−63PO$_{5/2}$ Ire prepared using the APS method. Upon replacing LaO$_{3/2}$ with GeO$_2$, an increase in both T_g and μ_H at T_g was observed [19]. The enhanced both T_g and μ_H at T_g can be attributed to the formation of heteroatomic P−O−Ge linkages. In this context, the Ge atoms exhibit six-fold coordination with the oxygen atoms and effectively bridge the (PO$_3^-$)$_n$ chains through these heteroatomic linkages. As a result, the phosphate frameworks become more rigid, leading to higher T_g values [19]. The formation of heteroatomic P−O−Ge linkages also influences the covalency of the P−O bonds. This increase in covalency subsequently impacts the ionicity of the O−H bond. To maintain a balanced electron transfer and prevent excessive reduction in electron density on the oxygen atom within the P−O−H bond, the ionicity of the O−H bond is increased. Consequently, the O−H bond weakens due to increased ionicity, resulting in enhanced μ_H at T_g [22]. In summary, the formation of heteroatomic P−O−Ge linkages contributes to the reinforcement of phosphate frameworks, higher T_g values, and the increased ionicity of O−H bonds. This, in turn, leads to improved proton mobility at T_g.

As predicted by present model, GeO$_2$ and WO$_3$ have emerged as favorable choices for enhancing both high proton conductivity and thermal stability in phosphate glasses designed for intermediate temperature. GeO$_2$ has already been experimentally validated in our previous work [19], demonstrating its ability to increase T_g and μ_H at T_g. On the other hand, the role of WO$_3$ remains to be experimentally confirmed.

2-4 Conclusions

In our study, I utilized a linear regression approach based on principal component analysis to develop models that describe the compositional dependence of log (μ_H at T_g) and T_g for proton-conducting phosphate glasses. These models allowed us to predict μ_H at T_g and T_g for a wide range of phosphate glass compositions, incorporating nine component oxides: $HO_{1/2}$, MgO, BaO, $LaO_{3/2}$, WO_3, $NbO_{5/2}$, $BO_{3/2}$, GeO_2, and $PO_{5/2}$. Although the models themselves lack physical significance, they provide valuable insights into the effects of individual component oxides on μ_H at T_g and T_g.

Our findings can be summarized as follows:

The concentration of $HO_{1/2}$ and $PO_{5/2}$ has a primary influence on μ_H at T_g, with μ_H at T_g increasing as the concentration of $HO_{1/2}$ increases and the concentration of $PO_{5/2}$ decreases. There is a linear relationship between log (μ_H at T_g) and T_g, supporting our previous estimation that the mobility of protons determines the motion of the glass framework in proton-conducting phosphate glasses. The component oxides can be categorized into three groups based on their effects on μ_H at T_g and T_g:

- Group 1 oxides, such as $HO_{1/2}$, MgO, BaO, $LaO_{3/2}$, and $BO_{3/2}$, behave as glass modifiers, increasing μ_H at T_g and decreasing T_g.

- Group 2 oxides, namely WO_3 and GeO_2, increase both μ_H at T_g and T_g.

- Group 3 oxides, represented by $NbO_{5/2}$, increase T_g without significantly affecting μ_H at T_g.

These insights are highly valuable for the design and development of purpose-designed glasses, particularly in the field of proton-conducting phosphate glasses. Furthermore, the addition of GeO_2 and WO_3 as group 2 oxides is crucial for achieving high proton conductivity in phosphate glasses at intermediate temperatures. The reported study investigated the role of GeO_2 in proton-conducting phosphate glasses, confirming its positive effect on T_g and μ_H at T_g through the formation of heteroatomic P−O−Ge linkages. The increased rigidity of the phosphate frameworks resulted in enhanced T_g and the enhanced ionicity of the O−H bonds resulted in enhanced μ_H at T_g. GeO_2, along with WO_3, emerged as favorable choices for enhancing proton conductivity and thermal stability.

References

1. T. Omata, T. Yamaguchi, S. Tsukuda, T. Ishiyama, J. Nishii, T. Yamashita, H. Kawazoe, Phys. Chem. Chem. Phys., 2019, **21**, 10744.

2. A. Makishima, J.D. Mackenzie, J. Non Cryst. Solids, 1973, **12**, 35-45.

3. B. Deng, J Non Cryst Solids, 2020, **529**, 119768.

4. S. Bishnoia, S. Singha, R. Ravindera, M. Bauchyb, N. N. Gosvamic, H. Kodamanad, N.M. A. Krishnan, J. Non Cryst. Solids, 2019, **524**, 119643.

5. T. Yamaguchi, S. Tsukuda, T. Ishiyama, J. Nishii, T. Yamashita, H. Kawazoe and T. Omata, J. Mater. Chem. A, 2018, **6**, 23628-23637.

6. T. Yamaguchi, T. Kataoka, S. Tsukuda, T. Ishiyama, J. Nishii, T. Yamashita, H. Kawazoe and T. Omata, Phys. Chem. Chem. Phys., 2017, **19**, 29669-29675.

7. T. Ishiyama, J. Nishii, T. Yamashita, H. Kawazoe and T. Omata, J. Mater. Chem. A, 2014, **2**, 3940-3947.

8. T. Yamaguchi, T. Ishiyama, K. Sakuragi, J. Nishii, T. Yamashita, H. Kawazoe and T. Omata, Solid State Ionics, 2015, **275**, 62-65.

9. T. Yamaguchi, Y. Saito, Y. Kuwahara, H. Yamashita, T. Ishiyama, J. Nishii, T. Yamashita, H. Kawazoe and T. Omata, J. Mater. Chem. A, 2017, **5**, 12385-12392.

10. K. Kawaguchi, T. Yamaguchi, T. Omata, T. Yamashita, H. Kawazoe and J. Nishii, Phys. Chem. Chem. Phys., 2015, **17**, 22855-22861.

11. T. Kinoshita, A. Miyazaki, K. Kawaguchi, D. Sakai, T. Yamaguchi, T. Omata, T. Ishiyama, M. Fujioka, H. Kaiju and J. Nishii, Appl. Surf. Sci., 2018, **428**, 718-722.

12. T. Ishiyama, S. Suzuki, J. Nishii, T. Yamashita, H. Kawazoe and T. Omata, Solid State Ionics, 2014, **262**, 856-859.

13. G. Harley, K. D. Kreuer, J. Maier, L. C. De Jonghe, J. Non Cryst. Solids, 2009, **355**, 932-937.

14. P. A. Bingham, R. J. Hand, O. M. Hannant, S.D. Forder, S. H. Kilcoyne, J. Non Cryst. Solids, 2009, **355**, 1526-1538.

15. N. Mascaraque, A. Durán, F. Muñoz, J. Non Cryst. Solids, 2011, **357**, 3212-3220.

16. S. Le Roux, S. Martin, R. Christensen, Y. Ren, V. Petkov, J. Phys.: Condens. Matter, 2011, **23**, 035403.

17. R. K. Brow, D. R. Tallant, J. Non Cryst. Solids, 1997, **222**, 396-406.

18. N. Boubata, A. Roula, I. Moussaoui, Bull. Mater. Sci., 2013, **36**, 457-460.

19. L. Y. Zhang, H. Li, L. L. Hu, J. Alloys Compd., 2017, **698**, 103-113.

20. G. Poirier, Y. Messaddeq, S. J. L. Ribeiro and M. Poulain, J. Solid State Chem., 2005, **178**, 1533-1538.

21. T. Honma, M. Okamoto, T. Togashi, N. Ito, K. Shinozaki, T. Komatsu, Solid State Ion., 2015, **269**, 19-23.

22. T. Omata, A. Sharma, T. Kinoshita, I. Suzuki, T. Ishiyama, S. Kohara, K. Ohara, M. Ono, T. Fang, Y. Ren, M. Fujioka, G. Zhaoh, J. Nishii, J. Mater. Chem. A, 2021, **9**, 20595.

Chapter 3 Experimental Investigation of Effect of WO$_3$ Addition on Proton Mobility and Thermal Stability in Proton-Conducting Phosphate Glasses

3-1 Introduction

In a recent investigation, our group explored the relationship between the composition of proton-conducting phosphate glasses and their proton mobility (μ_H) at the glass transition temperature (T_g) [1]. Additionally, I examined the correlation between T_g and composition using statistical analysis through a linear regression model [1]. The findings revealed that when glass-modifier oxides like alkali-earth oxides and rare-earth oxides replace PO$_{5/2}$, μ_H at T_g increases while T_g decreases. This suggests that higher concentrations of glass-modifier oxides improve proton conductivity but compromise thermal stability. Conversely, model predicted that replacing PO$_{5/2}$ with GeO$_2$ and WO$_3$ enhances both μ_H at T_g and T_g. This indicates that GeO$_2$ and WO$_3$ are preferable for achieving high proton conductivity and thermal stability in phosphate glasses at intermediate temperatures. In a recent study [2], to gain insights into the role of GeO$_2$ on the thermal stability and proton mobility of proton-conducting phosphate glasses was investigated through experimental study. To conduct the study, proton-conducting phosphate glasses with an approximate composition of 22HO$_{1/2}$−3NaO$_{1/2}$−(12−x)LaO$_{3/2}$−xGeO$_2$−63PO$_{5/2}$ were prepared using the APS method. Upon replacing LaO$_{3/2}$ with GeO$_2$, an increase in both T_g and μ_H at T_g was observed [2]. The enhanced both T_g and μ_H at T_g can be attributed to the formation of heteroatomic P−O−Ge linkages. In this context, the Ge atoms exhibit six-fold coordination with the oxygen atoms and effectively bridge the (PO$_3^-$)$_n$ chains through these heteroatomic linkages. As a result, the phosphate frameworks become more rigid, leading to higher T_g values [2]. The formation of heteroatomic P−O−Ge linkages also influences the covalency of the P−O bonds. This increase in covalency of P−O bonds subsequently impacts the ionicity of the O−H bond. To maintain a balanced electron transfer and prevent excessive reduction in electron density on the oxygen atom within the P−O−H bond, the ionicity of the O−H bond is increased. Consequently, the O−H bond weakens due to increased ionicity, resulting in enhanced μ_H at T_g [2]. In summary, the formation of heteroatomic P−O−Ge linkages contributes to the reinforcement of phosphate frameworks, higher T_g values, and the increased ionicity of O−H bonds. This, in turn, leads to improved proton mobility at T_g.

As predicted by present model, GeO$_2$ and WO$_3$ have emerged as favorable choices for enhancing both high proton conductivity and thermal stability in phosphate glasses designed for intermediate temperature. GeO$_2$ has already been experimentally validated in the previous work [2], demonstrating its ability to increase T_g and μ_H at T_g. On the other hand, the role of WO$_3$ remains to be experimentally confirmed. Therefore, in the this chapter, I focus on experimental investigations to elucidate the effect of WO$_3$ addition on thermal stability and proton mobility in proton-conducting phosphate glasses. The

aim is to verify the predicted role of WO₃, as determined by the linear regression model employing a statistical analysis approach.

Based on the relationship between μ_H at T_g, T_g and glass composition based on statistical analysis [1], WO₃ is a component that increases proton mobility and thermal stability of glasses. Figure 3-1 graph shows the trend between μ_H at T_g and T_g with increasing WO₃ content from red dots 0% to blue dots 2 mol% to green dots 4%, the μ_H at T_g and T_g both increases with increases WO₃ content, shown by black solid line. Now to validate these results, I have experimentally studied the effect of WO₃ on proton mobility and thermal stability in the proton-conducting phosphate glasses.
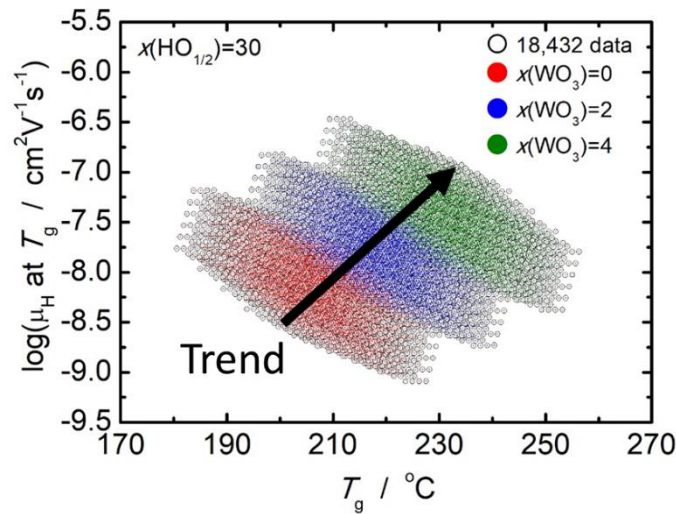
Figure 3-1 Distribution of the relationship between predicted values of log (μ_H at T_g) and T_g depending on the concentration of 18,432 predicted values for the glasses with 30 mol% of $HO_{1/2}$ distinguished by the WO₃ concentration (red dots = 0 mol% WO₃, blue dots = 2 mol% WO₃ and green dots = 4 mol% WO₃) [1].

For this purpose, I experimentally investigated the effect of WO₃ addition on thermal stability and proton mobility in $35HO_{1/2}-xWO_3-8NbO_{5/2}-5LaO_{3/2}-(52-x)PO_{5/2}$ (x = 2, 4, 6, and 8) glasses, referred to as xW-glass. The xW-glass samples were prepared using the APS technique. The experimental results confirmed the prediction of the linear regression model, showing that substituting $PO_{5/2}$ with WO₃ led to increased T_g and μ_H at T_g. To understand the underlying reasons, I examined the glass structure and the characteristics of O−H and P−O bonds. Similar to the case of GeO_2, the increased T_g was attributed to the presence of P−O−W linkages that tightly bridged the phosphate chains. However, unlike the GeO_2 case, the enhanced μ_H was not a result of weakened O−H bonds. Instead, it was due to a reduction in the migration barrier caused by an increased number of proton migration paths through non-bridging oxygens (NBOs) of WO_6 octahedra.

3-2 Experimental

3-2-1　Preparation of precursor glasses

I prepared precursor glasses of $35NaO_{1/2}-xWO_3-8NbO_{5/2}-5LaO_{3/2}-(52-x)PO_{5/2}$ (x = 2, 4, 6, and 8) using reagent-grade chemicals purchased from FUJIFILM Wako Chemicals, Japan, through a standard melt quenching method. Stoichiometric amounts of Na_2CO_3, WO_3, Nb_2O_5, La_2O_3, and H_3PO_4 (aq. 85%) were thoroughly mixed and melted at 1400 °C for 1 hour in an air atmosphere, utilizing a platinum crucible. The molten mixture was then poured into carbon molds and annealed at 450 °C for 20 minutes. Subsequently, the glasses were cooled slowly to room temperature at a rate of 20 °C per hour. Henceforth in this chapter, the glasses will be referred to as 2W, 4W, 6W, and 8W for ease of discussion.

3-2-2　Proton injection by APS

To facilitate proton injection, the cylindrical-shaped precursor glass obtained after annealing was cut into 0.8 mm thick disks with an 18 mm diameter as shown in Figure 3-2 (a). A 100 nm thick palladium (Pd) thin film was deposited on one surface of the disk using magnetron sputtering (JFC-1600, JEOL, Japan). The disk, with the Pd-film side facing upwards, was placed in a sample holder where the other side was in contact with a molten tin cathode in an H_2 atmosphere. I performed APS on all four glasses by applying a DC voltage of 10 V in the temperature range of 310−340 °C for 8−9 hours using the apparatus as shown in Figure 3-2 (b). Detailed information about the APS apparatus and working conditions can be found in chapter 1 [3-4]. I checked the glass nature of the specimens after APS by conducting X-ray diffraction (XRD) using Cu Kα radiation (SmartLab, Rigaku, Japan).
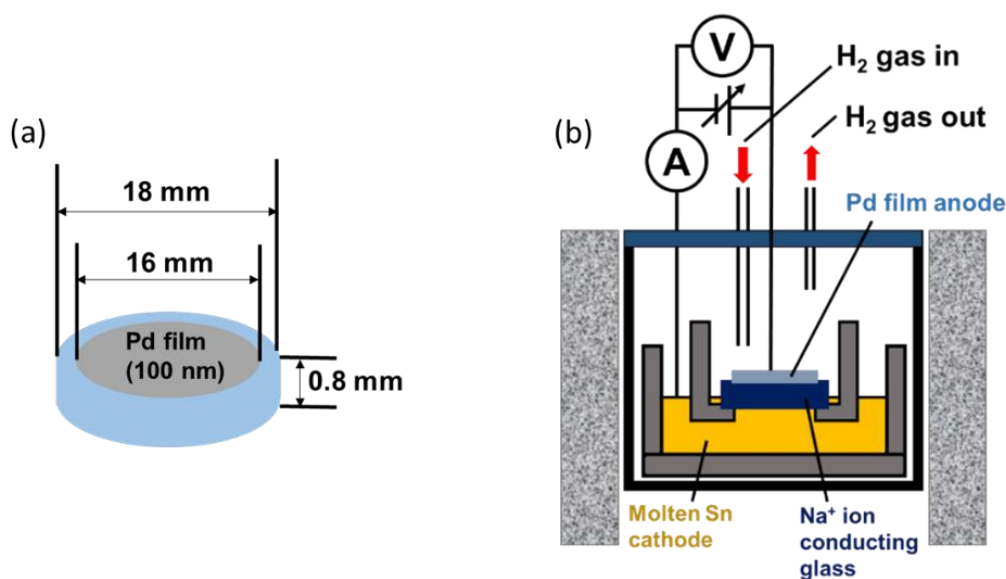
Figure 3-2 Schematic illustrations of (a) the sample configuration and (b) the APS apparatus.

3-2-3 Electrical properties

To evaluate the electrical properties, disk-shaped glasses were used. Pd thin-film electrodes with a thickness of 200 nm were deposited on both surfaces of the disk using magnetron sputtering. I employed an AC impedance method and an impedance analyzer (ModuLab, Solartron Analytical, UK) to measure the electrical conductivity in a dry 5% H_2/95% N_2 atmosphere. As the Pd electrodes served as non-blocking electrodes for both proton and electron carriers, the conductivity of the glasses was determined using the DC limit since the electrode resistance was significantly smaller than the electrolyte resistance. The mean transport number of protons in the glasses was determined by measuring the electromotive force (EMF) of a hydrogen concentration cell:

$$\text{gas (I), Pd} \mid x\text{W-glass (electrolyte)} \mid \text{Pd, gas (II)} \qquad\qquad 3\text{-}1$$
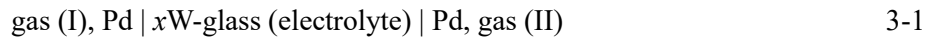
In gas (I), the hydrogen partial pressure was regulated at 1 atm through the continuous flow of H_2 gas, while in gas (II), the hydrogen partial pressure was controlled by diluting H_2 with N_2.

3-2-4 Characterization

For characterization purposes, I determined the glass transition temperature (T_g) using thermomechanical analysis (TMA) with a TD5000SA instrument (Bruker AXS, US). The test samples were subjected to an applied load of 68 mN mm^{-2}, and the temperature was increased at a rate of 20 °C min^{-1}. The sodium concentrations (C_{Na}) in the glass before and after APS were determined using an energy dispersive X-ray spectrometry (EDX) system (JED 2300, JEOL, Japan) integrated into a field emission scanning electron microscopy (FE-SEM) instrument (SU6600, Hitachi, Japan). Fourier-transform infrared spectroscopy (FT-IR; FT/IR-6100, JASCO, Japan) was employed to obtain infrared absorption spectra in the O–H stretching vibration region (v_{OH}) for evaluating O–H bonding characteristics and the concentration of OH groups corresponding to proton concentration. The concentration of OH groups, denoted as C_{OH} and measured in cm^{-3}, was determined from the maximum absorption intensity v_{OH} ($\alpha(v_{OH})$), by employing Equation 3-2 [5]:

$$C_{OH} = 1.03 \times 10^{19} \times \alpha(v_{\text{OH}}) \qquad\qquad 3\text{-}2$$

Raman spectra were obtained using a laser Raman spectrometer (NRS-3100, JASCO, Japan) with an excitation wavelength of 532 nm. The ^{31}P magic angle spinning nuclear magnetic resonance (MAS-NMR) spectra were obtained using a Bruker Avance 600 spectrometer operating at 14.1 T, corresponding to a Larmor frequency of 242.92 MHz. The measurements were conducted with a 4 mm magic-angle spinning probe at a spinning frequency of 30 kHz. The spectra were acquired using a pulse length of 4 ms (901 flip angle) and a recycle delay of 10 s. For reference, 85% H_3PO_4 was used during the spectra acquisition.

The P 2p core level X-ray photoelectron spectra (XPS) were examined using a PHI5600 spectrometer (ULVAC-PHI Inc., Japan) equipped with a hemispherical electron analyzer. Excitation was achieved

using monochromatic Al-Kα radiation ($h\nu$=1486.6 eV) as the source. To ensure surface integrity, all glass samples were prepared under a dry N_2 atmosphere and scraped to expose a fresh surface immediately prior to analysis. The samples were then placed on a gastight sample holder and loaded into the preparation chamber of the XPS apparatus, ensuring no exposure to air. During spectra recording, the residual pressure in the analyzing chamber was maintained at approximately 5×10^{-7} Pa. The binding energy of the system was calibrated at 284.8 eV using the C 1s core level for reference to account for residual carbon contamination [6,7].

3-3 Results and discussion

3-3-1 Proton injection by APS

Figure 3-3 (a) illustrates the depth profiles of Na and OH concentrations (C_{Na} and C_{OH}) in the 2W-glass before and after APS (dashed lines). Following APS, more than 90% of Na ions were discharged from the glass, while a substantial amount of OH was introduced into the glass. The absolute changes, ΔC_{Na} and ΔC_{OH}, were both determined to be 8.8×10^{21} cm^{-3}, indicating the successful electrochemical substitution of Na$^+$ ions with protons. The concentration profiles of Na and OH, denoted as C_{Na} and C_{OH} respectively, were analyzed in the 4W, 6W, and 8W-glasses both before and after APS, as shown in Figure 3-3 (b), (c), and (d) respectively. After-APS, it was observed that over 95% of Na ions were discharged from the glass, while a considerable amount of OH was introduced into the glass. The absolute changes, ΔC_{Na} and ΔC_{OH}, in these glasses exhibited slight variations, indicating that the 4W, 6W, and 8W-glasses after APS did not possess the same OH concentration as the Na ion concentration in the glass before APS. Nonetheless, the depth profiles of C_{Na} and C_{OH} indicated the successful electrochemical substitution of Na$^+$ ions with protons. XRD analysis confirmed that all after APS specimens remained in a glassy state as shown in Figure 3-4. Thus, successful synthesis of $35HO_{1/2}-xWO_3-8NbO_{5/2}-5LaO_{3/2}-(52-x)PO_{5/2}$ glasses (x=2, 4, 6, and 8) was achieved through APS.

After APS, the 2W- and 4W-glasses exhibited a nearly colorless appearance, whereas the 6W- and 8W-glasses appeared deeply blue as shown in Figure 3-5. This coloration can be attributed to the presence of W^{5+}, as transition metals tend to prefer lower valence states in glasses with low basicity [8]. The low basicity of our glasses, primarily resulting from the very low concentration of NaO$_{1/2}$. Additionally, the reducing hydrogen atmosphere during APS may have facilitated the formation of W^{5+}. The presence of W^{5+} in the 6W- and 8W-glasses suggests a mixed protonic and electronic conduction, similar to the cases of $35HO_{1/2}-20WO_3-55PO_{5/2}$ and $35HO_{1/2}-8WO_3-8NbO_{5/2}-5LaO_{3/2}-44PO_{5/2}$ [3, 4, 9-11].
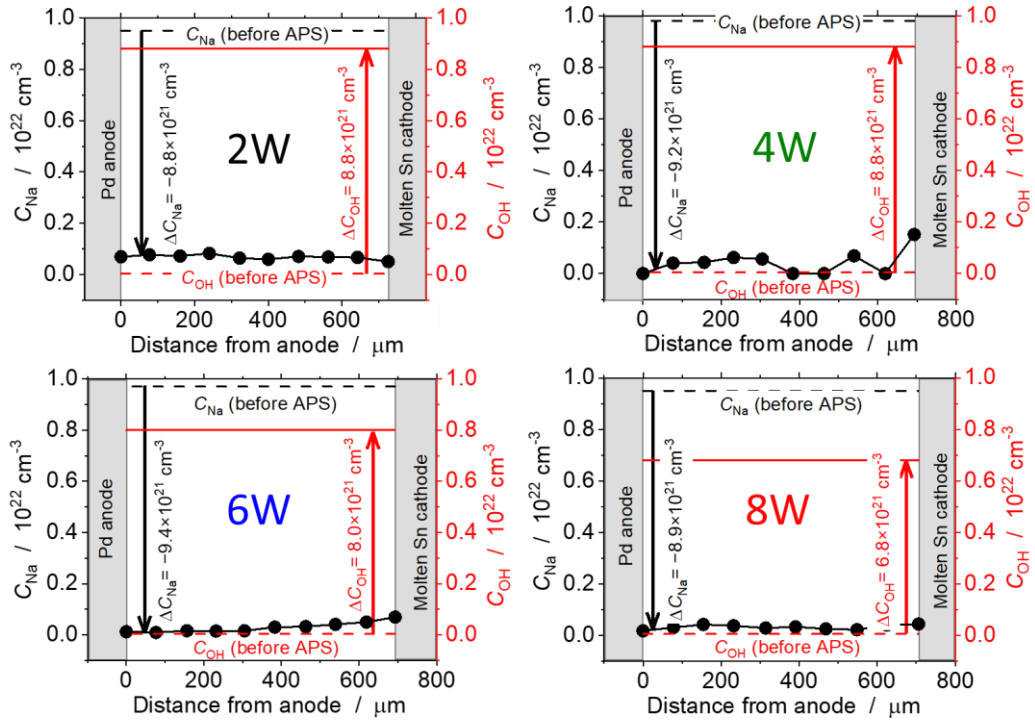
Figure 3-3 Depth profiles for glass (a) 2W, (b) 4W, (c) 6W and (d) 8W of C_{Na} (black dots) and C_{OH} (red solid line) for xW-glass after alkali-proton substitution (APS). The black and red dashed lines indicate C_{Na} and C_{OH}, respectively, for the xW-glass before APS.
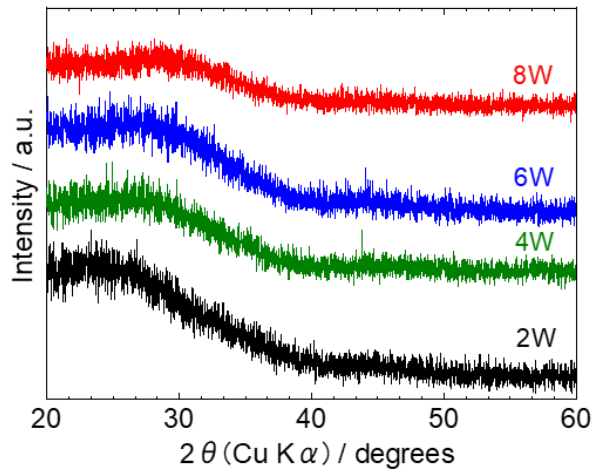

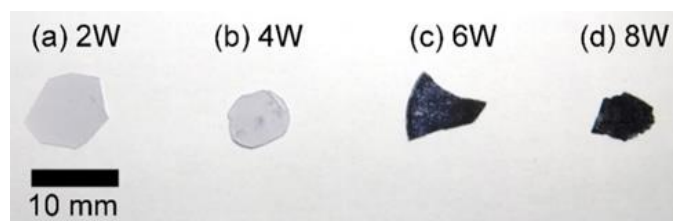**Figure 3-4** XRD patterns of the xW glasses after APS.

Figure 3-5 Photographic images of the glasses after alkali-proton substitution (APS) for the (a) 2W-, (b) 4W-, (c) 6W-, and (d) 8W-glasses.

3-3-2 Thermal stability

Figure 3-6 illustrates the relationship between T_g and the content of WO_3 in the glasses. It is evident that T_g increases as the WO_3 content increases, indicating that the replacement of $PO_{5/2}$ with WO_3 enhanced the thermal stability of the glasses. This observation aligns with the predictions of the linear regression model. The phenomenon of increased T_g has been reported in various phosphate glasses and is attributed to the formation of heteroatomic P−O−W bonds, which form strong cross-links between the phosphate glass networks [12-14]. Consequently, the improved T_g observed in our glasses with higher WO_3 content can be attributed to the formation of P−O−W linkages. Further insights into the glass structure will be discussed based on Raman and ^{31}P MAS-NMR spectra. The data presented in Figure 3-6 demonstrate that T_g exhibits an almost linear increase with increasing WO_3 content. The experimentally obtained slope, +9.1 °C per mol% of WO_3 replacing $PO_{5/2}$, closely matches the predicted slope of +6.5 °C per mol% of WO_3 from the linear regression model [1].
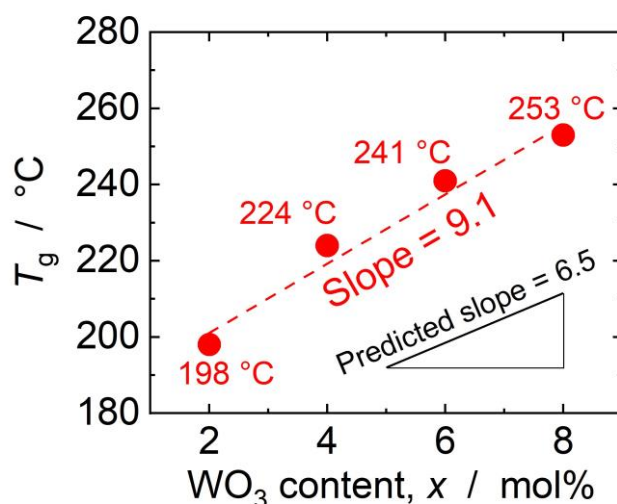
Figure 3-6 Variation of the glass transition temperature (T_g) of the glasses after alkali-proton substitution (APS) as a function of the WO_3 content (x). The triangle in the figure indicates the slope predicted by the linear regression model.

3-3-3 Proton conductivity

Figures 3-7 and 3-8 present the electromotive force (EMF) measurements of hydrogen concentration cells using glasses after APS as electrolytes, conducted at 207 °C and 243 °C, respectively. Table 3-1 summarizes the proton transport numbers (t_H) obtained from these measurements. The results indicate that the 2W- and 4W-glasses exhibit a t_H value of unity, signifying that they are pure proton-conducting electrolytes. In contrast, the t_H of the 6W- and 8W-glasses is less than 1, suggesting the presence of non-proton contributions to the conductivity. The partial conductivity attributed to these non-proton contributions were almost comparable to the Na^+ ion conductivity in the glasses before APS (Figure 3-

9). Given that the C_{Na} in the glasses after APS is less than 10% of the C_{Na} in the glasses before APS, it is unlikely to attribute the partial conductivity to Na^+ ions. Notably, the formation of W^{5+} in the 6W- and 8W-glasses, as indicated by their color (Figure 3-5), suggests a contribution from small-polaron hopping of electrons on W^{5+} in the glasses, which is a known phenomenon in phosphate glasses containing WO_3 [3, 4, 9-11]. This is attributed to electronic conductivity, which increases with higher WO_3 content due to an increased electron carrier density. However, the t_H values of the 6W- and 8W-glasses remain above 0.9, indicating very small electronic contribution to the conductivity and the t_H of these glasses was constant within the measured temperature range. Consequently, the protonic conductivity of all the glasses can be investigated.
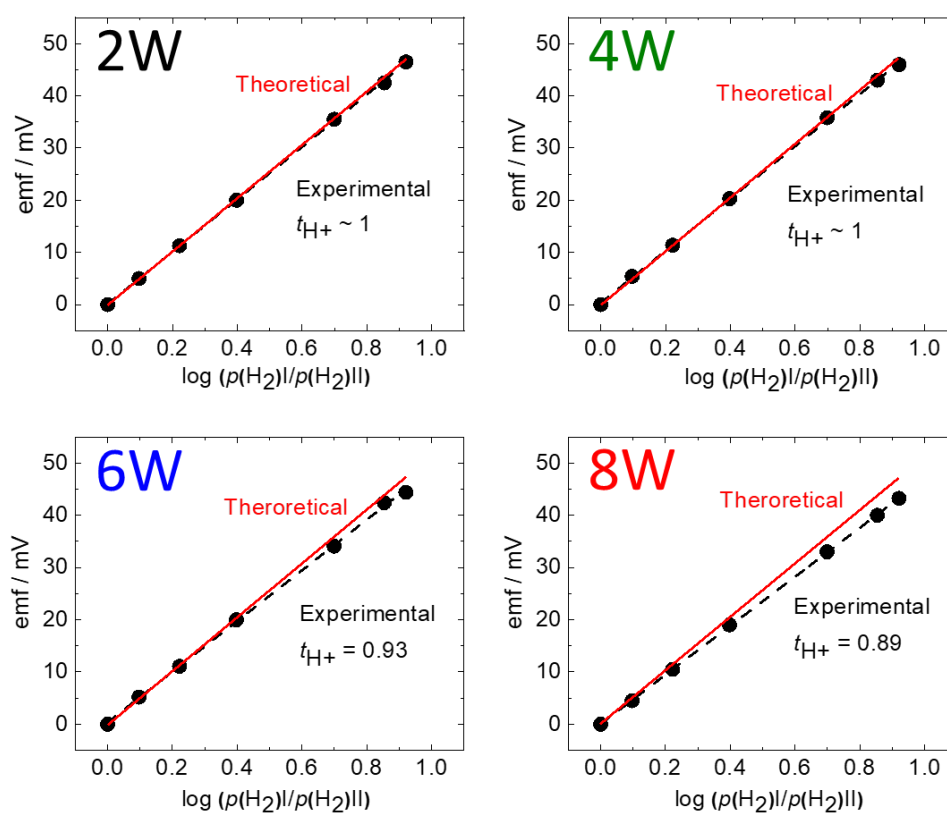
Figure 3-7 Electromotive forces (EMFs) for the hydrogen concentration cell as a function of logarithmic hydrogen partial pressure, $p(H_2)$, ratio at 207 °C for xW glass after alkali-proton substitution (APS). The theoretical emfs calculated using the Nernst equation, E= $(RT/2F)$ ln(p(H$_2$)$_{high}$/p(H$_2$)$_{low}$) are shown as red lines.

Table 3-1 Proton transport number (t_H) at 207 and 243 °C of the xW-glasses after alkali-proton substitution (APS) determined by measuring the electromotive force (EMF) of the hydrogen concentration cells.

Glass	Proton transport number, t_H	
	207 °C	243 °C
2W	1	1
4W	1	1
6W	0.93	0.93
8W	0.89	0.89
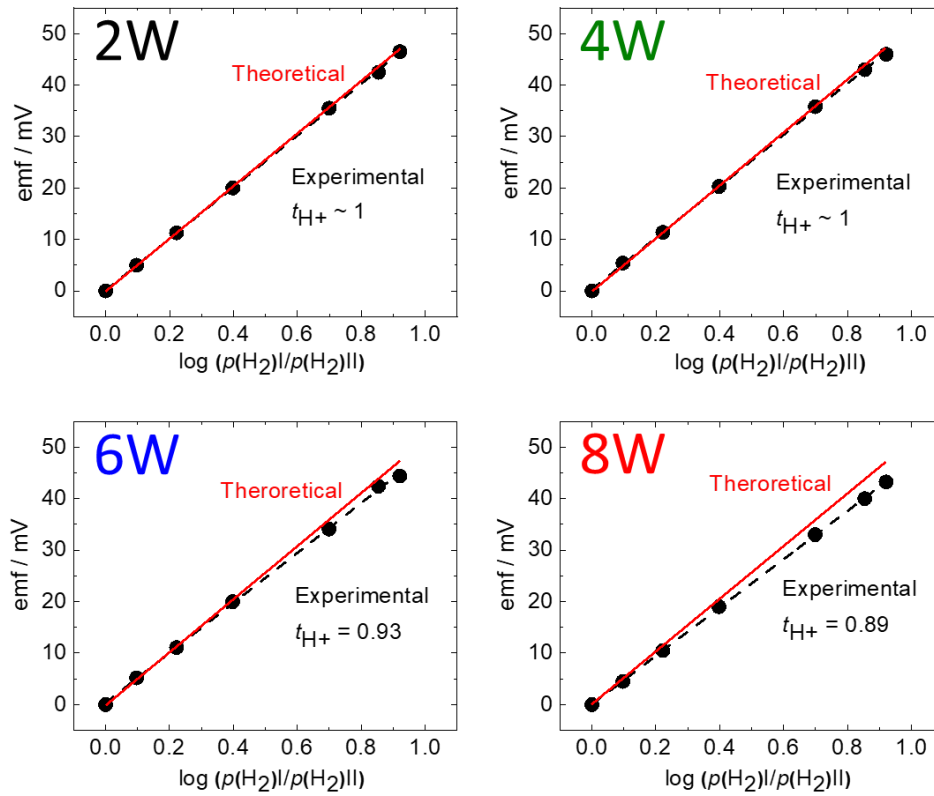
Figure 3-8 Electromotive forces (EMFs) for the hydrogen concentration cell as a function of logarithmic hydrogen partial pressure, $p(H_2)$, ratio at 243 °C for xW glass after alkali-proton substitution (APS). The theoretical emfs calculated using the Nernst equation, E= $(RT/2F)$ ln(p(H$_2$)$_{high}$/p(H$_2$)$_{low}$) are shown as red lines.

Figure 3-10 presents the Arrhenius plot of the proton conductivity for the glasses. The proton conductivity corresponds to the total conductivity for the 2W- and 4W-glasses, while for the 6W- and 8W-glasses, it was derived from total conductivity and t_H values. The proton conductivity ranges from 10^{-6} to 10^{-4} S cm^{-1} over temperatures between 150 °C and 300 °C. The conductivities of the respective glasses remain within the same order of magnitude throughout the temperature range. Although no significant variation in conductivity based on WO$_3$ content is observed, the activation energy (E_a) for proton hopping conduction, obtained from the ln(σT) vs. $1/T$ plot, gradually decreases from 0.79 to 0.70 eV with increasing WO$_3$ content from 2 to 8 mol% (Figure 3-11 (a)). Figure 3-11 (b) displays μ_H at T_g, calculated from the proton conductivity at T_g and the proton carrier density (n_H) assuming all protons forming OH groups are mobile ($n_H=C_{OH}$). The μ_H at T_g increases with higher WO$_3$ content. These results indicate a reduction in the energy barrier for proton conduction and increased mobility of proton carriers as the WO$_3$ content increases. The log (μ_H at T_g [cm^2 V^{-1} s^{-1}]) increases by 0.09 per mol% of WO$_3$, aligning closely with the predicted value of 0.08 from the previously proposed log (μ_H at T_g)-composition model [1].
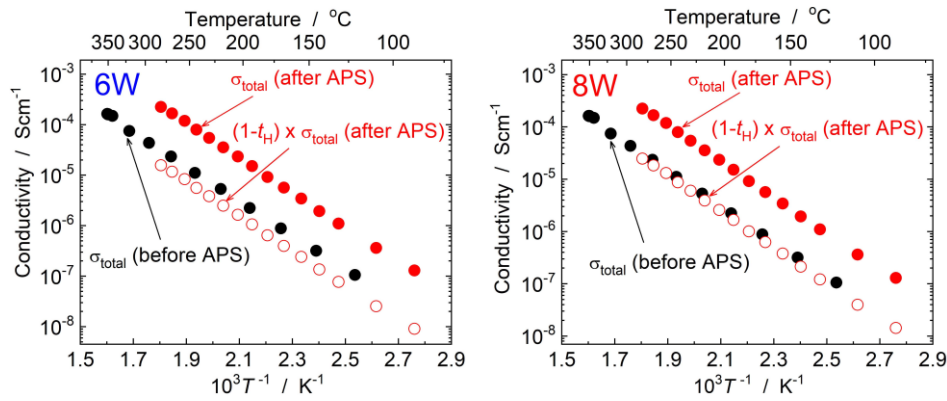
Figure 3-9 Arrhenius plot of the total conductivity (σ_{total}) and partial conductivity due to non-proton contributions (($1-t_H)\times\sigma_{total}$) of the 6W- and 8W- glasses after APS comparing with total conductivity, i.e., approximately Na$^+$ ion conductivity, of them before APS.
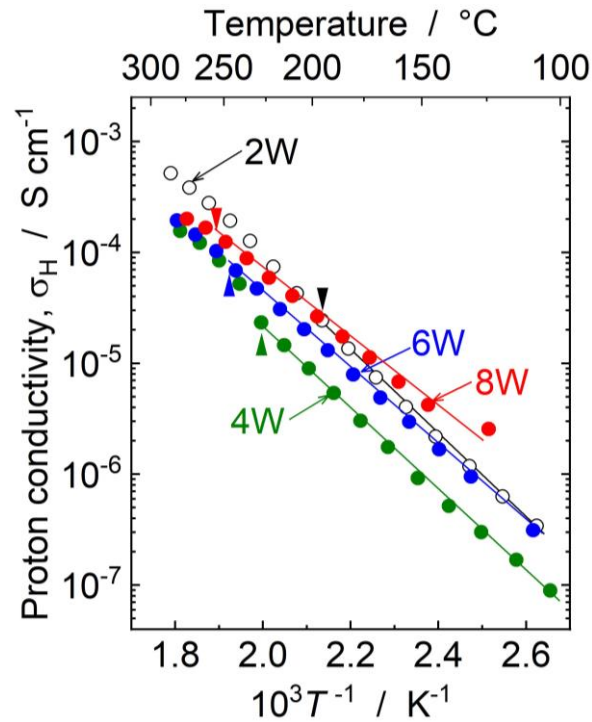
Figure 3-10 Arrhenius plot of the proton conductivity of the glasses after alkali-proton substitution (APS). The triangles correspond to the proton conductivities at the glass transition temperature (T_g) of each glass.

In summary, the experimental findings demonstrate that the addition of WO$_3$ to phosphate glasses enhances their thermal stability and proton mobility, resulting in improved proton conductivity. Both T_g and μ_H at T_g increase with higher WO$_3$ content, as predicted by the linear regression model. These results suggest that WO$_3$ is a suitable oxide component for enhancing the properties of proton-conducting phosphate glasses. However, a WO$_3$ content ≥ 6 mol% leads to partial electronic conduction.
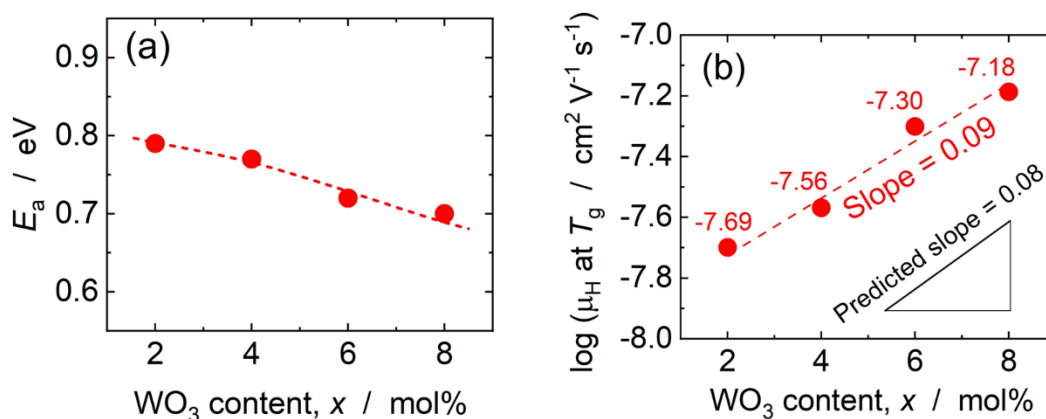
Figure 3-11 Variation of (a) activation energy (E_a) of the proton conduction, and (b) proton mobility (μ_H) at the glass transition temperature (T_g) as a function of the WO$_3$ content (x). The triangle in (b) indicates the slope of μ_H at T_g predicted by the linear regression model.

3-4 Origin of enhanced thermal stability and proton mobility

3-4-1 Thermal stability

The improved thermal stability of phosphate glasses when substituting PO$_{5/2}$ with WO$_3$ is commonly associated with the creation of P−O−W bonds, which effectively interconnect the network of the phosphate glass [12-14]. Therefore, it is crucial to examine the formation of P−O−W bonds and the local structure surrounding the P atom. The analysis employed the Q^n notation and its extended Q$^n_{mM}$ notation, where n represents the number of bridging oxygens (BOs) connected to P atoms, and m represents the number of BOs connected to M atoms (M denotes Nb or W atom).

The Raman spectra of the glasses after APS, as shown in Figure 3-12, reveal important features and is summarized in Table 3-2 [15-20]. The dominant bands observed at 900−1000 cm^{-1} correspond to the stretching modes of Nb−O$^-$ and W−O$^-$ bonds (v_{MO}^-), indicating the presence of NbO$_6$ and WO$_6$ octahedra. The bands at ~700 cm^{-1} and ~1150 cm^{-1} are associated with the symmetric stretching vibrations of the P−O−P bond for the Q^2 unit (v_{sym}(P−O−P)Q^2) and the symmetric stretching vibrations of the O−P−O bond for the Q^2 unit (v_{sym}(PO$_2$)Q^2), respectively, primary spectral features representing the phosphate framework. This suggests that the primary phosphate ion forming the glass framework is the chain type (PO^{3-})$_l$. The (v_{sym}(P−O−P)Q^2) and (v_{sym}(PO$_2$)Q^2) bands undergo shifts to higher and lower wavenumber regions, respectively, with increasing WO$_3$ content, indicating a reduction in the length of the phosphate chain and the depolymerization of (PO^{3-})$_l$ chains [21-23]. The absence of the band assigned to pyrophosphate (P$_2$O$_7^{4-}$) ions indicates that the depolymerization did not progress enough to form pyrophosphate ions. Furthermore, there is no evidence of the formation of homoatomic W−O−W linkages at ~820-840 cm^{-1} [24] in 2W-, 4W-, and 6W-glasses, indicating the preference for heteroatomic P−O−W linkages, similar to previous reports. However, in 8W-glass, there is a possibility of the formation of W−O−Nb bonds as indicated by the asterisk in Figure 3-12.
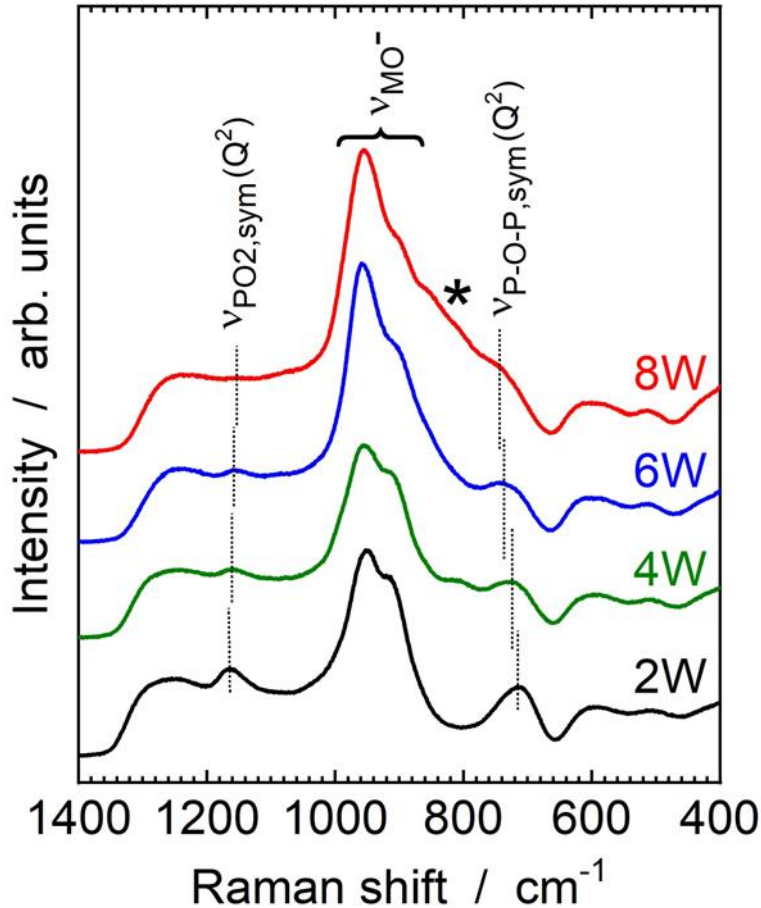
Figure 3-12 Raman spectra of the *x*W-glasses after alkali-proton substitution (APS).

The ^{31}P MAS-NMR spectra of the glasses after APS, presented in Figure 3-13, exhibit a broadened single peak for all glasses. In the 2W-glass, a distinct peak is observed around -22 ppm, accompanied by a minor shoulder around -10 ppm. The relative intensities of the peaks at approximately -22 ppm and -10 ppm decreased and increased, respectively, with increasing WO_3 content as indicated by the thin dashed lines in figure 3-13. The -22 ppm peak in the spectrum is attributed to the Q^2 unit, whereas the -10 ppm peak is assigned to the Q^1_{1M} unit [13, 24-26]. The changes in the ^{31}P MAS-NMR spectra, as depicted in Figure 3-13, can be interpreted based on these assignments. It indicates a decrease in the number of Q^2 units, suggesting the depolymerization of $(PO_3^{3-})_l$ phosphate chains with increasing WO_3 content. Additionally, the increased intensity of the peak assigned to the Q^1_{1M} units indicates the formation of heteroatomic P−O−W linkages with higher WO_3 content.

Based on the analysis of the Raman and ^{31}P MAS-NMR spectra, the substitution of $PO_{5/2}$ with WO_3 induces structural changes, including the depolymerization of $(PO_3^{3-})_l$ chains and the formation of cross-linkages between one-dimensional $(PO_3^{3-})_l$ chains through P−O−W bonds facilitated by WO_6 octahedra. This transformation results in the transition from a one-dimensional phosphate network to a three-dimensional tungstophosphate network as the WO_3 content increases. WO_3 acts as an intermediate oxide in terms of glass-forming ability, and its single W−O bond strength of 318 kJ mol^{-1} is comparable to

other typical glass-forming oxides such as P_2O_5 (464 kJ mol^{-1}), SiO_2 (443 kJ mol^{-1}), and GeO_2 (343 kJ mol^{-1}) [27]. Consequently, the replacement of $PO_{5/2}$ with WO_3 strengthens the glass network, leading to an increase in T_g due to the formation of a three-dimensional tungstophosphate network.

Table 3-2 Assignment of the Raman bands observed for xW-glass after alkali-proton substitution (APS).

Assignment[a]	Position / cm^{-1}					Ref.
	2W	4W	6W	8W		
δ_{O-M-O}	265	265	265	265	Bending mode of O–M–O of MO_6 octahedra	15-18
δ_{O-M-O^-}	380	380	380	380	Bending mode of O–M–O$^-$ of MO_6 octahedra	15-18
$\delta_{O-M-O} + \delta_{O-P-O}$	508	509	512	514	Combination mode of the O–M–O bending mode with the O–P–O bending mode	15-18
ν_{M-O}	598	596	595	594	Stretching mode of the M–O bond of MO_6 octahedra	15-18
$\nu_{P-O-P,\ sym}(Q^2)$	714	724	738	746	Symmetric stretching mode of the P–O–P bond for the Q^2 unit	19-20
ν_{W-O-W}	-	-	-	820	Stretching vibrations of W–O–W linkages	24
ν_{M-O^-}	917, 950	912, 954	907, 956	902, 956	Stretching mode of the M–O$^-$ bond of MO_6 octahedra	15-18
$\nu_{O-P-O,\ sym}(Q^2)$	1163	1159	1157	1153	Symmetric stretching mode of NBOs for the Q^2 unit	19-20
$\nu_{O-P-O,\ assym}(Q^2)$	1246	1244	1242	1240	Asymmetric stretching mode of NBOs for the Q^2 unit	19-20

[a] M denotes Nb or W
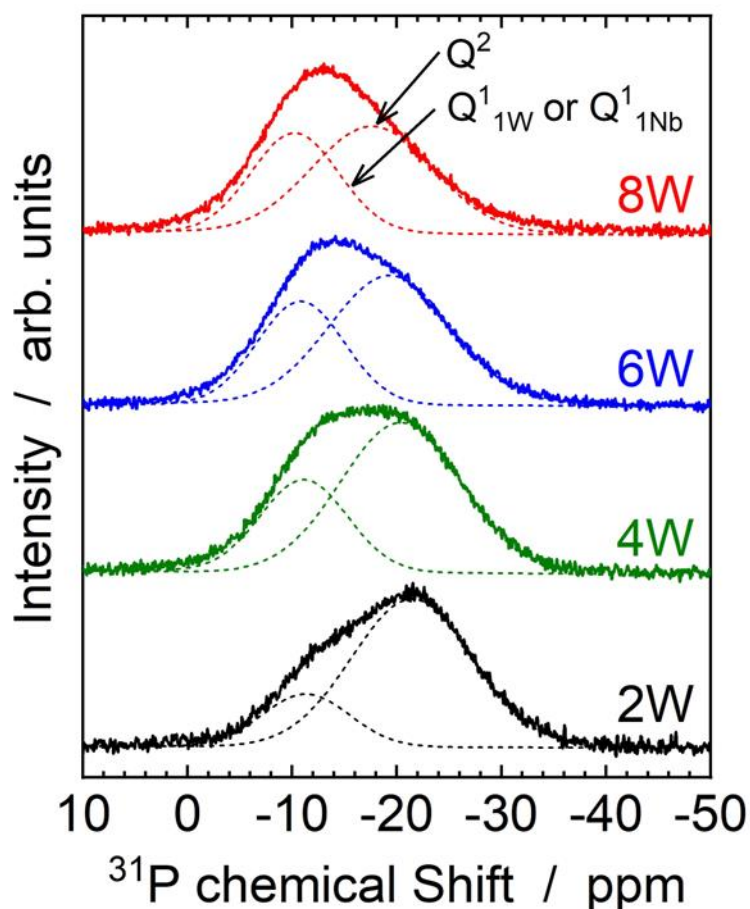
Figure 3-13 ^{31}P magic angle spinning nuclear magnetic resonance (MAS-NMR) spectra of the xW-glasses after alkali-proton substitution (APS).

3-4-2 Proton mobility

Based on the hopping mechanism, the activation energy (E_a) can be expressed as the sum of two contributions: the energy barrier (E_d) for proton dissociation from the O−H bonding and the energy barrier (E_m) for proton migration, as represented by Equation (3-3) [28].

$$E_a = E_d + E_m \qquad\qquad (3\text{-}3)$$

To determine the dominant contribution responsible for the observed reduction in E_a upon replacing $PO_{5/2}$ with WO_3 (as depicted in Figure 3-11 (a)), I first investigated O−H stretching vibration that reflect O−H bond strength affecting E_d.

Figure 3-14 displays the infrared (IR) spectra in the OH stretching vibration region (v_{OH}) region (ranging from 2500−3600 cm^{-1}) of the xW-glasses after APS. The spectra of all glasses exhibit an intense and broadened absorption peak at approximately 2900 cm^{-1}, accompanied by a shoulder at around 3300 cm^{-1}. The dashed lines in Figure 3-14 represent the deconvolution results of the spectra, indicating two absorption bands at approximately 2900 and 3300 cm^{-1}. The intensity of the band at around 2900 cm^{-1} remains relatively constant regardless of the WO_3 content, while the band at around 3300 cm^{-1} slightly increases in intensity with increasing WO_3 content. Typically, the band at around 2900 cm^{-1} is associated with the v_{OH} of the OH groups at Q^2 units, corresponding to the internal PO_4 units in $(PO_3^{-})_l$ chains. On the other hand, the band at around 3300 cm^{-1} originates from the OH groups at Q^1 units, corresponding to the terminal PO_4 unit in $(PO_3^{-})_l$ chains [29]. Additionally, the area fractions of Q^1 (Q^1_{1M}) and Q^2 units obtained from ^{31}P MAS-NMR spectroscopy generally correspond to the area fractions of the v_{OH} bands at around 3300 and 2900 cm^{-1}, respectively [30,31]. However, in the current xW-glasses, the variations in the area fractions of IR and ^{31}P MAS-NMR spectra do not align with each other, as illustrated in figure 3-15. The increase in intensity of the 3300 cm^{-1} IR band is relatively small and approximately half of the increase in intensity of Q^1_{1M} in the ^{31}P MAS-NMR spectra.

The nature of O−H bonding in phosphate glasses that exhibit proton conduction, whether it is ionic or covalent, relies on the characteristics of P−O bonding [2]. The extent of electron transfer from the phosphorus atom to the oxygen atom determines the ionic or covalent nature of the P−O−H bond. In cases where the P−O bonding is highly ionic, the phosphorus atom donates electrons to the oxygen atom, inhibiting electron donation from the hydrogen atom to the oxygen atom. The O−H bonding becomes covalent resulting in avoiding excessive electron density on the oxygen atom. On the other hand, if the P−O bonding is highly covalent, the O−H bonding becomes ionic to maintain the appropriate electron density of the oxygen atom [32]. Consequently, the v_{OH} band appears at a higher frequency when the P−O bonding is ionic, indicating stronger O−H bonding. Conversely, when the P−O bonding is highly covalent, the O−H bonding is weakened, resulting in the v_{OH} band appearing at a lower frequency.
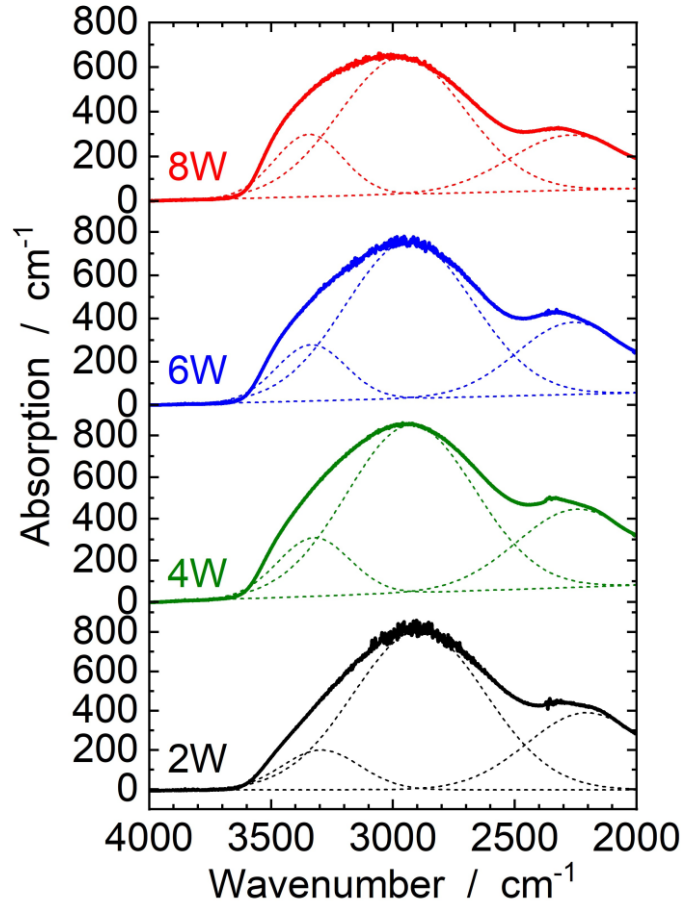
Figure 3-14 Infrared spectra in the ν_{OH} region of the xW-glasses after alkali-proton substitution (APS). The deconvoluted spectra into two ν_{OH} bands at ~3300 and 2900 cm^{-1} is indicated by dashed lines.
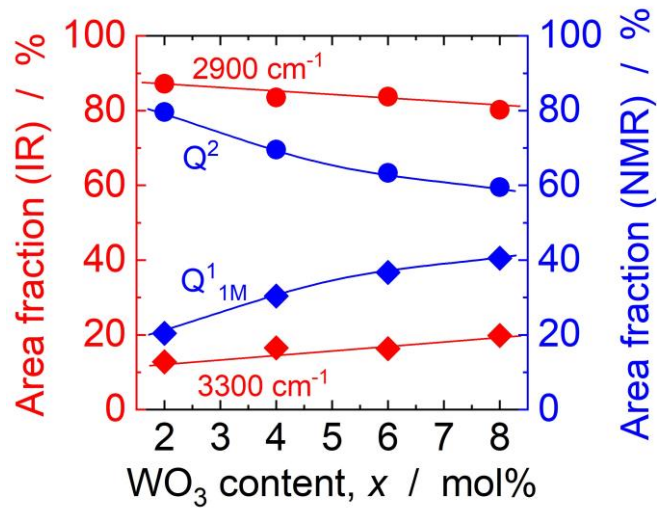

Figure 3-15 Variation of the area fraction of ν_{OH} bands at ~3300 and 2900 cm^{-1} (red dots and squares), and ^{31}P magic angle spinning nuclear magnetic resonance (MAS-NMR) peaks for Q^1_{1M} and Q^2 type PO_4 units (blue dots and squares) of the xW-glasses as a function of the WO_3 content (x).

The P 2p core-level X-ray photoelectron spectroscopy (XPS), which enables the assessment of the ionicity or covalency of P−O bonds, is a valuable tool for investigating the v_{OH} band. Even slight variations in the nature of P−O bonding, leading to shifts in the frequency of v_{OH} by tens of cm^{-1}, can be detected as peak shifts of 0.3 to 0.5 eV did not change in all xW-glasses, regardless of the fractions of Q^1_{1M} and Q^2 units. In other words, the average ionicity or covalency of the P−O bonding in Q^1_{1M} and Q^2 units is the same. Based on the relationship between the nature of P−O and O−H bonding, the frequency of the v_{OH} band for the OH groups at Q^1_{1M} and Q^2 units should be same. The observed phenomenon, where the fraction of the v_{OH} band at around 3300 cm^{-1} only slightly increases despite an increase in the fraction of Q^1_{1M} units with higher WO$_3$ content, can be explained by considering that the v_{OH} bands for the OH groups at Q^1_{1M} units appear at around 2900 cm^{-1}, similar to those of the OH groups at Q_2 units. The reason for the slight increase in the fraction of v_{OH} at around 3300 cm^{-1} will be discussed later. With the nearly unchanged O−H bonding nature in all xW-glasses, the contribution of E_d in the proton hopping process does not change significantly, regardless of the WO$_3$ content. Consequently, it can be safely concluded that the reduction in E_a with increasing WO$_3$ content primarily arises from the decrease in E_m rather than E_d of the OH group.

The long-range migration of protons in the xW-glasses follows two elemental migration paths: intra-phosphate chain migration and inter-phosphate chain migration. In intra-phosphate chain migration, protons hop between non-bridging oxygens (NBOs) in adjacent PO$_4$ units. This migration process occurs along the hydrogen bonding network, as illustrated in Figure 3-17 (a), and is characterized by a relatively low energy barrier. On the other hand, inter-phosphate chain migration involves the movement of protons between NBOs in separate phosphate chains connected by glass network modifiers such as La^{3+} ions in the current glasses. The hydrogen bonding network plays a minimal role in facilitating inter-phosphate chain migration. Additionally, during inter-phosphate chain migration, protons encounter a significant energy barrier when passing near positively charged La^{3+} ions, as indicated by the blue dashed line in Figure 3-17 (d). Consequently, the energy barrier associated with inter-phosphate chain migration predominantly contributes to the overall activation energy (E_a).

By increasing the WO$_3$ content, cross-linking between the phosphate chains is facilitated through the incorporation of WO$_6$ octahedra. This leads to the formation of bonding structures involving heteroatomic P−O−W linkages, specifically ≡P−O−W−O−P≡ bonds. Proton conduction has been observed in materials such as H$_x$WO$_3$ [34] and WO$_3$·2H$_2$O [35], where non-Grotthus-type and hopping mechanisms are involved. In the current glasses, the corner-sharing WO$_6$ octahedra, as illustrated in Figure 3-17 (c), serves as migration pathways for protons. Importantly, inter-phosphate chain proton migration occurs without the protons coming into close proximity to the positively charged W^{6+} ions. This is due to the geometric arrangement of the corner-sharing WO$_6$ octahedra with the PO$_4$ tetrahedra. Moreover, the formation of hydrogen bonding between the O−H group at the PO$_4$ tetrahedron and the non-bridging oxygen at the WO$_6$ octahedron is highly likely. These characteristics suggest that the

energy barrier for inter-phosphate chain proton migration via WO_6 octahedra is smaller compared to migration via LaO_8 polyhedra, as depicted by the green line in Figure 3-17 (d).
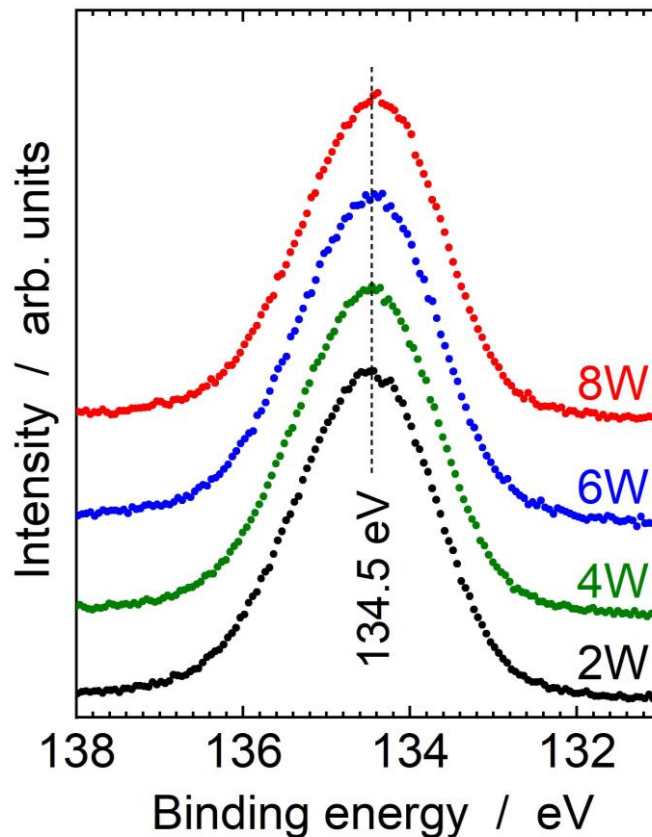

Figure 3-16 P 2p core-level X-ray photoelectron spectroscopy (XPS) spectra of the xW-glasses after alkali-proton substitution (APS).

When WO_6 octahedra serve as proton migration pathways, the presence of v_{OH} bands corresponding to the OH groups at the WO_6 octahedra should be observed in the infrared (IR) spectra. Previous research on various WO_3-based proton conductors has reported the presence of v_{OH} bands around 3300 cm^{-1}, often accompanied by a long tail extending to lower frequency regions [36-38]. In the current xW-glasses, a slight increase in absorption around 3300 cm^{-1} was indeed observed as depicted in Figures 3-14 and 3-15, with this increase attributed to the emergence of v_{OH} for W−O−H bonding. Consequently, I can conclude that the reduction in activation energy (E_a) and the enhancement of μ_H at T_g with increasing WO_3 content can be attributed to the decreased E_m resulting from the enhanced cross-linkages between $(PO^{3-})_l$ phosphate ion chains facilitated by the presence of WO_6 octahedra (specifically, the formation of P−O−W linkages).

The mixing of glass former oxides is known to induce enhanced mobility and conductivity in alkali-ion conduction glasses, a phenomenon commonly referred to as the MGF effect [9,39,40]. This effect arises from the increased availability of migration paths resulting from the mixture of glass former

oxides. In the present study, the observed enhancement in proton mobility upon replacing $PO_{5/2}$ with WO_3 can be attributed to the formation of P−O−W linkages, which in turn increases the number of migration paths available for proton conduction.
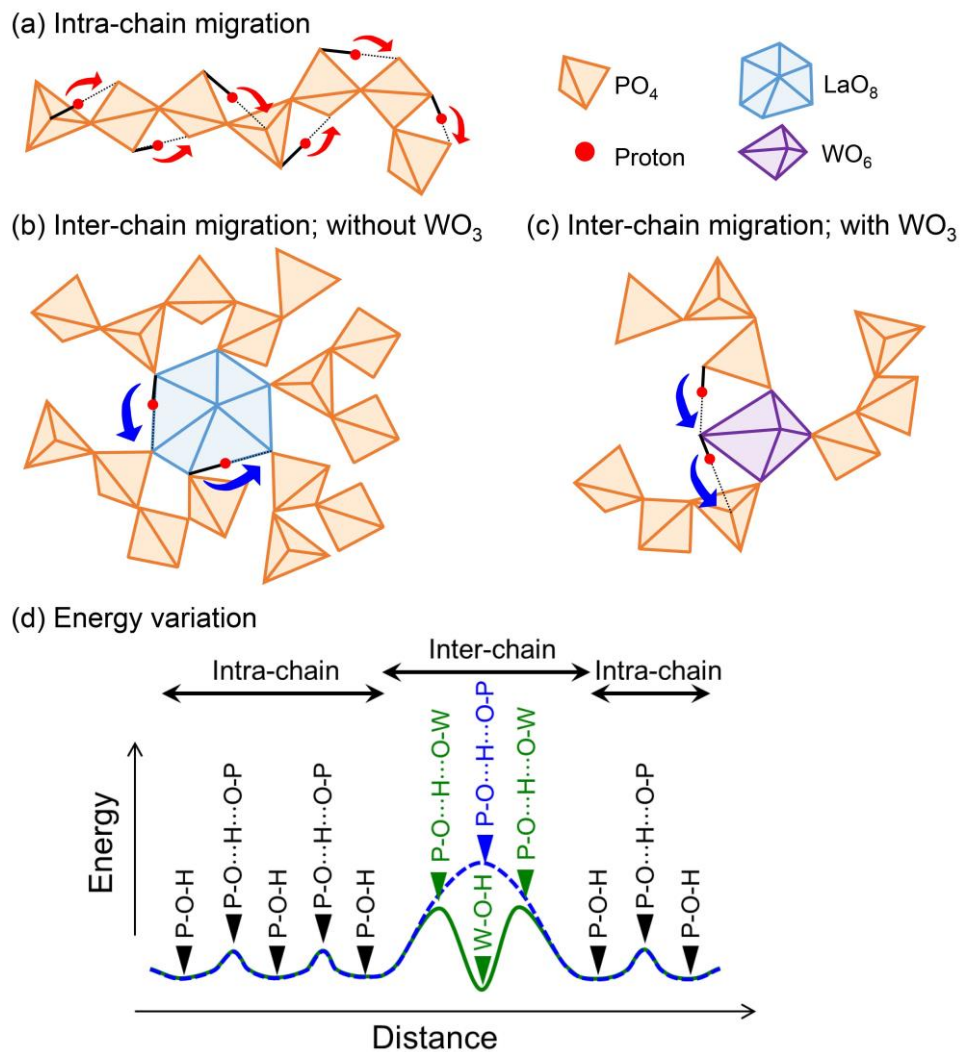
Figure 3-17 Schematic illustrations of (a) intra-phosphate chain and inter-phosphate chain proton migration (c) with and (d) without WO_3. (d) Variation in the relative potential energy of a proton carrier during migration. The blue dashed line and solid green line indicate proton migration involving the inter-phosphate chain migration via LaO_8 polyhedron and WO_6 octahedron, respectively.

3-5 Conclusion

The effect of WO_3 on the T_g and μ_H at T_g was experimentally investigated in $35HO_{1/2}-xWO_3-8NbO_{5/2}-5LaO_{3/2}-(52-x)PO_{5/2}$ glasses. The replacement of $PO_{5/2}$ with WO_3 led to the enhancement of both T_g and μ_H at T_g, as predicted by the linear regression model. The observed enhancement rates were in line with the predicted values, with an increase of +9.1 °C per mol% of WO_3 for T_g and 0.09 per mol% of WO_3 for log (μ_H at T_g [cm^2 V^{-1} s^{-1}]). The increase in T_g was attributed to

the formation of the P−O−W linkage, which resulted in increased cross-linking within the glass network, as previously reported for $NaO_{1/2}$−WO_3−$PO_{5/2}$ glasses. On the other hand, the increase in μ_H at T_g was attributed to the reduction in the energy barrier for inter-phosphate chain proton migration, facilitated by formation of P−O−W linkages, which in turn increases the number of migration paths available for proton conduction.

While previous studies in proton-conducting phosphate glasses have primarily focused on enhancing μ_H by modifying the strength of O−H bonds (controlling E_d) [2,33,41], this study revealed that in xW-glasses, the enhancement of μ_H arises from the reduction in E_m due to the formation of the P−O−W linkage. Although 6 mol% or higher concentrations of WO_3 may introduce partial electronic conduction, limiting their suitability as electrolytes.

References

1. T. Omata, I. Suzuki, A. Sharma, T. Ishiyama, J. Nishii, T. Yamashita and H. Kawazoe, RSC Adv., 2021, **11**, 3012–3019.

2. T. Omata, A. Sharma, T. Kinoshita, I. Suzuki, T. Ishiyama, S. Kohara, K. Ohara, M. Ono, T. Fang, Y. Ren, M. Fujioka, G. Zhao and J. Nishii, J. Mater. Chem. A, 2021, **9**, 20595–20606.

3. T. Ishiyama, S. Suzuki, J. Nishii, T. Yamashita, H. Kawazoe and T. Omata, J. Electrochem. Soc., 2013, **160**, E143–E147.

4. T. Ishiyama, S. Suzuki, J. Nishii, T. Yamashita, H. Kawazoe and T. Omata, Solid State Ion., 2014, **262**, 856–859.

5. Y. Abe and D. E. Clark, J. Mater. Sci. Lett., 1990, **9**, 244–245.

6. Y. Goto, K. Taniguchi, T. Omata, S. Otsuka-Yao-Matsuo, N. Ohashi, S. Ueda, H. Yoshikawa, Y. Yamashita, H. Oohashi and K. Kobayashi, Chem. Mater., 2008, **20**, 4156–4160.

7. D. Fang, F. He, J. Xie and L. Xue, Journal Wuhan University of Technology, Materials Science Edition, 2020, **35**, 711–718.

8. J. A. Duffy, J. Non Cryst. Solids, 1996, **196**, 45–50.

9. S. Renka, L. Pavić, G. Tricot, P. Mošner, L. Koudelka, A. Moguš-Milanković and A. Šantić, Phys. Chem. Chem. Phys., 2021, **23**, 9761–9772.

10. I. Oliva, A. Masuno, H. Inoue, M. Sakamoto and K. Morita, Solid State Ion., 2014, **255**, 56–59.

11. A. Šantić, J. Nikolić, S. Renka, L. Pavić, P. Mošner, L. Koudelka, G. Tricot and A. Moguš-Milanković, Solid State Ion., 2022, **375**, 115849.

12. G. Poirier, Y. Messaddeq, S. J. L. Ribeiro and M. Poulain, J. Solid State Chem., 2005, **178**, 1533–1538.

13. C. C. De Araujo, W. Strojek, L. Zhang, H. Eckert, G. Poirier, S. J. L. Ribeiro and Y. Messaddeq, J. Mater. Chem., 2006, **16**, 3277–3284.

14. P. Mosner, O. Kupetska, L. Koudelka, Phys. Chem. Glas.: Eur J Glass Sci. Technol. B, 2018, **59**, 213-220.

15. M. G. Donato, M. Gagliardi, L. Sirleto, G. Messina, A. A. Lipovskii, D. K. Tagantsev and G. C. Righini, Appl. Phys. Lett., 2010, **97**, 231111.

16. A. El Jazouli, J. C. Viala, C. Parent, G. Le Flem and P. Hagenmuller, J. Solid State Chem., 1988, **73**, 433–439.

17. K. Fukumi and S. Sakka, J. Mater. Sci., 1988, **23**, 2819–2823.

18. J. M. Jheng and I. E. Wachs, Chem. Mater., 1991, **3**, 100–107.

19. R. K. Brow, J. Non Cryst. Solids, 2000, **263–264**, 1–28.

20. R. K. Brow, D. R. Tallant, J. J. Hudgens, S. W. Martin and A. D. Irwin, J. Non Cryst. Solids, 1994, **177**, 221–228.

21. M. A. Karakassides, A. Saranti and I. Koutselas, J. Non Cryst. Solids, 2004, **347**, 69–79.

22. T. Yamaguchi, T. Kataoka, S. Tsukuda, T. Ishiyama, J. Nishii, T. Yamashita, H. Kawazoe and T. Omata, Phys. Chem. Chem. Phys., 2017, **19**, 29669–29675.

23. M. Tatsumisago, Y. Kowada and T. Minami, Phys. Chem. Glasses, 1988, **29**, 63–66.

24. P. Kalenda, L. Koudelka, P. Mošner, L. Montagne, B. Revel, J. Non Cryst. Solids, 2020, **541**, 120145.

25. R. J. Kirkpatrick and R. K. Brow, Solid State Nucl. Magn. Reson., 1995, **5**, 9–21.

26. A. Flambard, L. Montagne, L. Delevoye, G. Palavit, J. P. Amoureux and J. J. Videau, J. Non Cryst. Solids, 2004, **345–346**, 75–79.

27. T. Ishiyama, T. Yamaguchi, J. Nishii, T. Yamashita, H. Kawazoe, N. Kuwata, J. Kawamura and T. Omata, Phys. Chem. Chem. Phys., 2015, **17**, 13640–13646.

28. T. Komatsu and V. Dimitrov, Int. J. Appl. Glass Sci., 2020, **11**, 253–271.

29. T. Ishiyama, T. Yamaguchi, J. Nishii, T. Yamashita, H. Kawazoe and T. Omata, J. Electrochem. Soc., 2022, **169**, 034517.

30. A. Naruse, Y. Abe and H. Inoue, J. Ceram. Assoc. Jpn., 1968, **76**, 36.

31. T. Yamaguchi, T. Ishiyama, K. Sakuragi, J. Nishii, T. Yamashita, H. Kawazoe, N. Kuwata, J. Kawamura and T. Omata, Solid State Ion., 2016, **288**, 281–285.

32. T. Yamaguchi, T. Ishiyama, K. Sakuragi, J. Nishii, T. Yamashita, H. Kawazoe and T. Omata, Solid State Ion., 2015, **275**, 62–65.

33. T. L. Barr, Modern Esca: The Principles and Practice of X-Ray Photoelectron Spectroscopy, 1994.

34. T. Yamaguchi, Y. Saito, Y. Kuwahara, H. Yamashita, T. Ishiyama, J. Nishii, T. Yamashita, H. Kawazoe and T. Omata, J. Mater. Chem. A, 2017, **5**, 12385–12392.

35. J. P. Randin and R. Vienne, J. Electrochem. Soc., 1982, **129**, 2349.

36. H. Lin, F. Zhou, C. P. Liu and V. Ozoliņš, J. Mater. Chem. A, 2014, **2**, 12280–12288.

37. H. Morita, Jpn. J. Appl. Phys., 1985, **24**, 744.

38. M. Hashimoto, G. Koyano and N. Mizuno, J. Phys. Chem. B, 2004, **108**, 12368–12374.

39. G. Koyano, T. Saito, M. Hashimoto and M. Misono, Stud. Surf. Sci. Catal., 2000, **130**, 3077–3082.

40. A. Magistris, G. Chiodelli and M. Villa, J. Power Sources, 1985, **14**, 87–91.

41. K. Sklepić, R. D. Banhatti, G. Tricot, P. Mošner, L. Koudelka and A. Moguš-Milanković, J. Phys. Chem. C, 2017, **121**, 17641–17657.

42. T. Omata, A. Sharma, I. Suzuki, T. Ishiyama, S. Kohara, K. Ohara, M. Ono, Y. Ren, K. Zagarzusem, M. Fujioka, G. Zhao and J. Nishii, ChemPhysChem, 2022, **23**, 1–5.

Appendix

S-3-1   Results and Discussions of the precursor glasses

S-3-1-1   Thermal Stability

Figure S3-1 illustrates the relationship between T_g and the content of WO$_3$ in the precursor's glasses, i.e., glasses before APS. It is evident that T_g increases as the WO$_3$ content increases, indicating that the replacement of PO$_{5/2}$ with WO$_3$ enhanced the thermal stability of the glasses. The phenomenon of increased T_g has been reported in various phosphate glasses containing WO$_3$ and is attributed to the formation of heteroatomic P−O−W bonds, which form strong cross-links between the phosphate glass networks [12-14]. Consequently, the improved T_g observed in our glasses with higher WO$_3$ content can be attributed to the formation of P−O−W linkages. Further insights into the glass structure will be discussed based on Raman and ^{31}P MAS-NMR spectra. The data presented in Figure S3-1 demonstrate that T_g exhibits an almost linear increase with increasing WO$_3$ content.
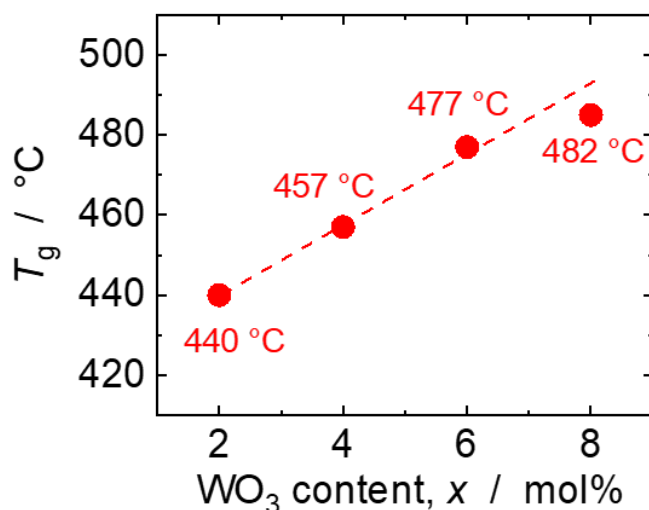
Figure S3-1 Variation of the glass transition temperature (T_g) of the glasses before alkali-proton substitution (APS) as a function of the WO$_3$ content (x).

S-3-1-2   Electrical conductivity

Figure S3-2 presents the Arrhenius plot of the total electrical conductivity for the glasses before APS. The electrical conductivity is assumed to be the mixed sodium ions and electronic conductivity for the 2W-, 4W-, 6W- and 8W-glasses. The electrical conductivity ranges from 10^{-7} to 10^{-3} S cm^{-1} over temperatures between 120 °C and 400 °C. The conductivities of the respective glasses remain within the same order of magnitude throughout the temperature range. Although no significant variation in conductivity based on WO$_3$ content is observed.
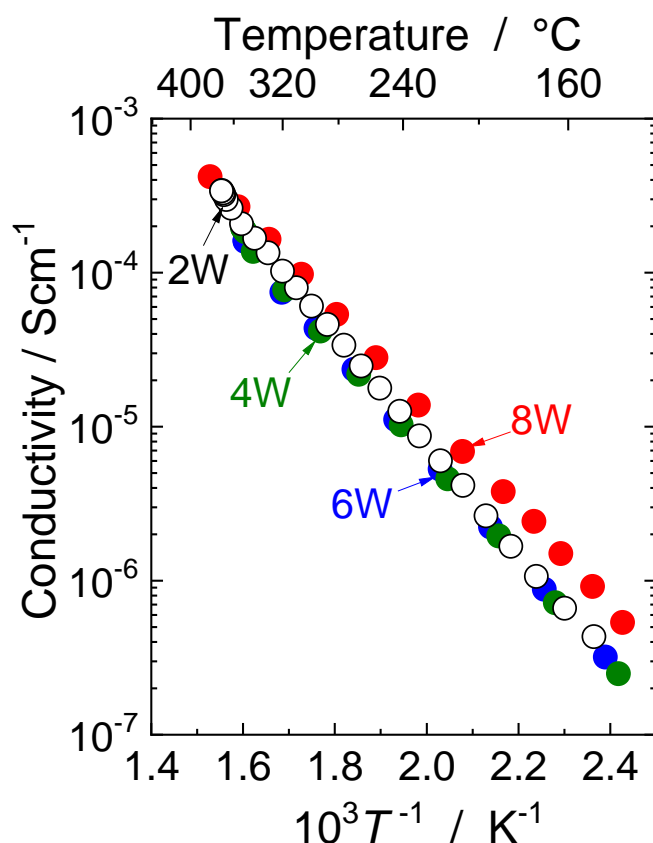
Figure S3-2 Arrhenius plot of the conductivity of the glasses before alkali-proton substitution (APS).

S-3-1-3 Origin of enhanced thermal stability in the glasses before APS

The improved thermal stability of phosphate glasses when substituting $PO_{5/2}$ with WO_3 is commonly associated with the creation of P−O−W bonds, which effectively interconnect the network of the phosphate glass [12-14]. Therefore, it is crucial to examine the formation of P−O−W bonds and the local structure surrounding the P atom. The analysis employed the Q^n notation and its extended Q^n_{mM} notation, where n represents the number of bridging oxygens (BOs) connected to P atoms, and m represents the number of BOs connected to M atoms (M denotes Nb or W atom).

The Raman spectra of the glasses before APS, as shown in Figure S3-3, reveal important features and is summarized in Table S3-1 [15-20]. The dominant bands observed at 900−1000 cm^{-1} correspond to the stretching modes of Nb−O^- and W−O^- bonds (v_{MO}^-), indicating the presence of NbO_6 and WO_6 octahedra. The bands at ~700 cm^{-1} and ~1150 cm^{-1} are associated with the symmetric stretching vibrations of the P−O−P bond for the Q^2 unit (v_{sym}(P−O−P)Q^2) and the symmetric stretching vibrations of the O−P−O bond for the Q^2 unit (v_{sym}(PO_2)Q^2), respectively, primary spectral features representing the phosphate framework. This suggests that the primary phosphate ion forming the glass framework is the chain type $(PO_3^{3-})_l$. The (v_{sym}(P−O−P)Q^2) and (v_{sym}(PO_2)Q^2) bands undergo shifts to higher and lower wavenumber regions, respectively, with increasing WO_3 content, indicating a reduction in the length of the phosphate chain and the depolymerization of $(PO_3^{3-})_l$ chains [21-23]. The absence of the band assigned to pyrophosphate ($P_2O_7^{4-}$) ions indicates that the depolymerization did not progress enough to

form pyrophosphate ions. Furthermore, there is no evidence of the formation of homoatomic W−O−W linkages at ~820-840 cm^{-1} [24] in 2W-, 4W-, and 6W-glasses, indicating the preference for heteroatomic P−O−W linkages, similar to previous reports. However, in 8W-glass, there is a possibility of the formation of W−O−Nb bonds as indicated by the asterisk in Figure S3-3.

Figure S3-3 Raman spectra of the xW-glasses before alkali-proton substitution (APS).

The ^{31}P MAS-NMR spectra of the glasses before APS, presented in Figure S3-4, exhibit a broadened single peak for all glasses. In the 2W-glass, a distinct peak is observed around -20 ppm, accompanied by a minor shoulder around -12 ppm. The relative intensities of the peaks at approximately -20 ppm and -12 ppm decreased and increased, respectively, with increasing WO_3 content as indicated by the thin dashed lines in figure S3-4. The -20 ppm peak in the spectrum is attributed to the Q^2 unit, whereas the -12 ppm peak is assigned to the Q^1_{1M} unit [13, 24-26]. The changes in the ^{31}P MAS-NMR spectra, as depicted in Figure S3-4, can be interpreted based on these assignments. It indicates a decrease in the number of Q^2 units, suggesting the depolymerization of $(PO_3^-)_l$ phosphate chains with increasing WO_3 content. Additionally, the increased intensity of the peak assigned to the Q^1_{1M} units indicates the formation of heteroatomic P−O−W linkages with higher WO_3 content.

Table S3-1 Assignment of the Raman bands observed for xW-glass before alkali-proton substitution (APS).

Assignment[a]	Position / cm^{-1}					Ref.
	2W	4W	6W	8W		
δ_{O-M-O}	265	265	265	265	Bending mode of O–M–O of MO$_6$ octahedra	15-18
δ_{O-M-O^-}	380	380	380	380	Bending mode of O–M–O$^-$ of MO$_6$ octahedra	15-18
$\delta_{O-M-O} + \delta_{O-P-O}$	508	509	512	514	Combination mode of the O–M–O bending mode with the O–P–O bending mode	15-18
ν_{M-O}	605	605	605	605	Stretching mode of the M–O bond of MO$_6$ octahedra	15-18
$\nu_{P-O-P,\ sym}(Q^2)$	700	710	712	715	Symmetric stretching mode of the P–O–P bond for the Q^2 unit	19-20
ν_{W-O-W}	-	-	-	830	Stretching vibrations of W–O–W linkages	24
ν_{M-O^-}	914, 938	912, 940	907, 942	902, 943	Stretching mode of the M–O$^-$ bond of MO$_6$ octahedra	15-18
$\nu_{O-P-O,\ sym}(Q^2)$	1161	1156	1146	1137	Symmetric stretching mode of NBOs for the Q^2 unit	19-20
$\nu_{O-P-O,\ assym}(Q^2)$	1240	1234	1223	1217	Asymmetric stretching mode of NBOs for the Q^2 unit	19-20

Based on the analysis of the Raman and ^{31}P MAS-NMR spectra, the substitution of PO$_{5/2}$ with WO$_3$ induces structural changes, including the depolymerization of (PO^{3-})$_l$ chains and the formation of cross-linkages between one-dimensional (PO^{3-})$_l$ chains through P−O−W bonds facilitated by WO$_6$ octahedra. This transformation results in the transition from a one-dimensional phosphate network to a three-dimensional tungstophosphate network as the WO$_3$ content increases. WO$_3$ acts as an intermediate oxide in terms of glass-forming ability, and its single W−O bond strength of 318 kJ mol^{-1} is comparable to other typical glass-forming oxides such as P$_2$O$_5$ (464 kJ mol^{-1}), SiO$_2$ (443 kJ mol^{-1}), and GeO$_2$ (343 kJ mol^{-1}) [27]. Consequently, the replacement of PO$_{5/2}$ with WO$_3$ strengthens the glass network, leading to an increase in T_g due to the formation of a three-dimensional tungstophosphate network.

S-3-1-4 Nature of O−H and P−O bond in the glasses before APS

Figure S3-5 presents the infrared (IR) spectra in the OH stretching vibration region (ν_{OH}) of the xW-glasses before APS. By replacing WO$_3$ with PO$_{5/2}$, changes in the peak positions are observed for the residual protons remained in the glasses after melting process. Specifically, the peak shifts from 2834 cm^{-1} in the 2W glass to 2923 cm^{-1} in the 4W glass and exhibits a slight increase from the 4W to the 8W glass. These observations suggest that the substitution of 2 to 4 mol% PO$_{5/2}$ with WO$_3$ results in the strengthening of the O−H bond, while the substitution from 4 mol% to 8 mol% leads to only a slight strengthening of the O−H bond with increasing WO$_3$ content. Typically, the band at around 2900 cm^{-1} is associated with the ν_{OH} of the OH groups at Q^2 units, corresponding to the internal PO$_4$ units in (PO^{3-})$_l$ chains [29].
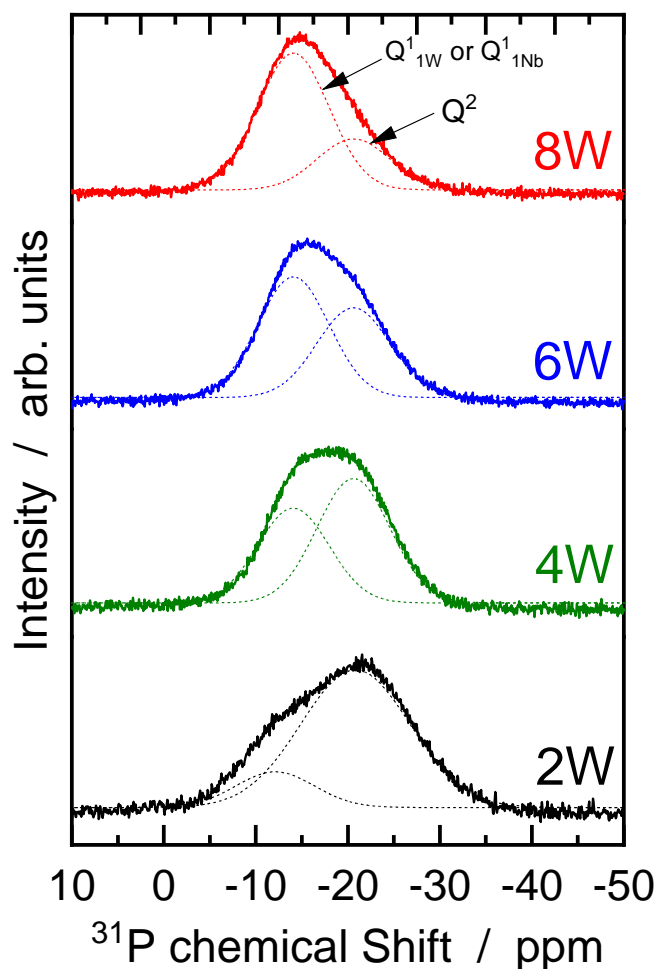
Figure S3-4 ^{31}P magic angle spinning nuclear magnetic resonance (MAS-NMR) spectra of the xW-glasses before alkali-proton substitution (APS).

The P 2p core-level X-ray photoelectron spectroscopy (XPS), which enables the assessment of the ionicity or covalency of P−O bonds. Figure S3-6 illustrates the changes in binding energy and full width at half maximum (FWHM) of the P 2p core-level peak, which consistently shift to lower binding energies with increasing substitution of $PO_{5/2}$ with WO_3. Specifically, the peak shifts from 134.1 eV in the 2W glass to 133.97 eV in the 4W glass, with a slight increase of 0.07 eV observed from the 4W to the 8W glass. These observations indicate that the substitution of 2 mol% to 4 mol% of $PO_{5/2}$ with WO_3 results in an increase in the covalency of the P−O bond, while the substitution from 4 mol% to 8 mol% leads to a slight increase in covalency. In summary, these findings suggest a progressive shift towards a more covalent nature of the P−O bond with increasing WO_3 content.
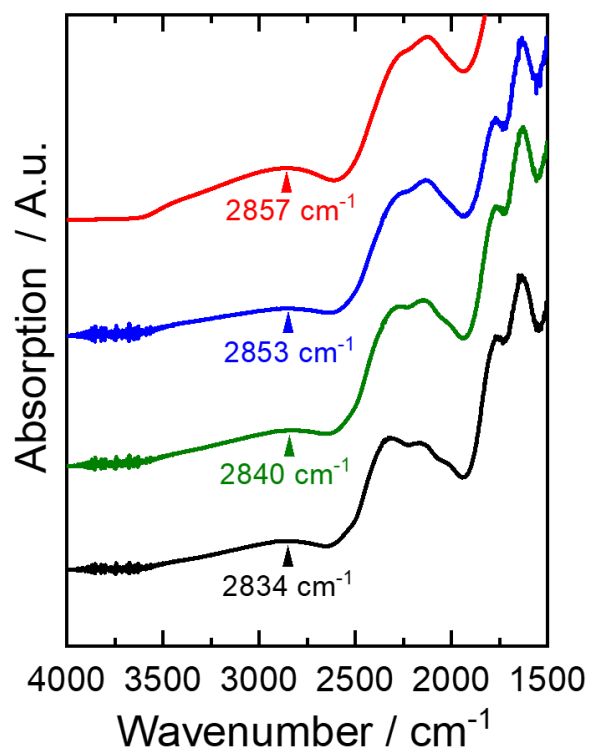
Figure S3-5 Infrared spectra in the ν_{OH} region of the xW-glasses before alkali-proton substitution (APS).
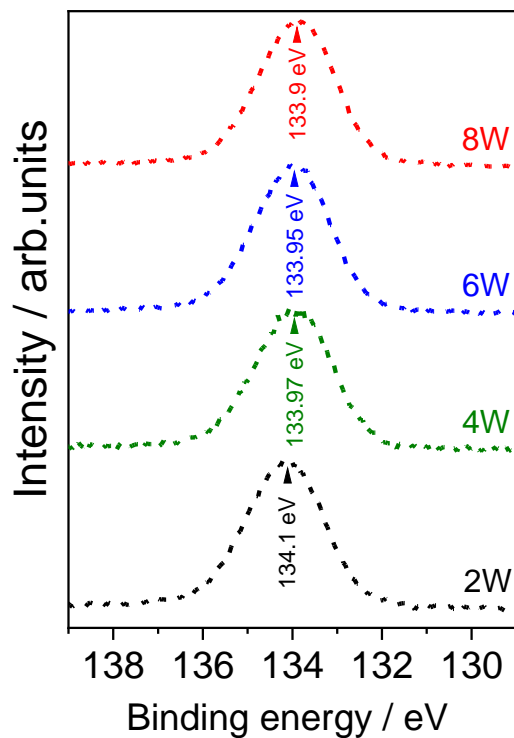
Figure S3-6 P 2p core-level X-ray photoelectron spectroscopy (XPS) spectra of the xW-glasses before alkali-proton substitution (APS).

Chapter 4 Experimental Investigation of Effect of V_2O_5 Addition on Proton Mobility and Thermal Stability in Proton-Conducting Phosphate Glasses

4-1 Introduction

The previous investigation emphasized the role of WO_3 in enhancing the thermal stability of glass compositions by promoting strong cross-linking between phosphate chains. WO_3 is widely recognized as a conditional glass former. In the case of WO_3, the increase in proton mobility (μ_H) at T_g was attributed to the reduction in the energy barrier for inter-phosphate chain proton migration, facilitated by formation of P−O−W linkages, which in turn increases the number of migration paths available for proton conduction. The increased number of migration pathways are attributed to the presence of non-bridging oxygen (NBO) sites associated with WO_6 octahedra units. Similarly, $VO_{5/2}$ is also recognized as a conditional glass former, known for its ability to establish strong cross-linking between phosphate chains, resulting in an enhanced glass transition temperature (T_g) [1-3]. Similarly, it has been reported that vanadium phosphate glasses contain at least one NBO site associated with vanadium ion units [3-6]. However, the effect of $VO_{5/2}$ on proton mobility remains unexplored. To address this gap, experimental investigation was conducted in this study to explore the potential of $VO_{5/2}$ as a conditional glass former and to evaluate its effect on thermal stability and proton mobility. Previous research has indicated that compositions with more than 20 mol% of $VO_{5/2}$ exhibit dominating electronic conductivity [7-8]. Conversely, compositions with less than 15 mol% of $VO_{5/2}$ have a T_g below 350 °C, making them unsuitable for APS because the T_g is expected to reduce 150-200 °C during APS with high possibility of APS temperature being higher than the crystallization temperature of the glasses after APS, resulting in crystallization of the glasses after APS [9-10]. Therefore, a composition containing 20 mol% $VO_{5/2}$ was selected to strike a balance between these factors.

In this chapter, I experimentally investigated the effect of $VO_{5/2}$ addition on thermal stability and proton mobility in $29HO_{1/2}-1NaO_{1/2}-6VO_{5/2}-14VO_2-50PO_{5/2}$ glass. The glass sample was prepared using the APS technique. Although, the addition of $VO_{5/2}$ into the glass usually results in electronic conduction, luckily the glass after APS was pure proton conductor. The experimental results confirmed the high T_g, despite the positive influence on T_g, the addition of $VO_{5/2}$ in the glass composition led to low proton mobility. To understand the underlying reasons, I examined the glass structure and the characteristics of O−H bonds. Similar to the case of WO_3, the increased T_g was attributed to the presence of P−O−V linkages that tightly bridged the phosphate chains. However, unlike the WO_3 case, the high μ_H was not observed. Instead, the strong trapping of protons resulted in low proton mobility.

4-2 Experimental
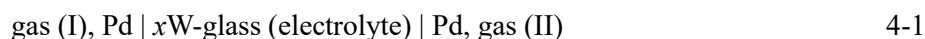
4-2-1 Preparation of precursor glasses

The precursor glasses were prepared using reagent-grade chemicals purchased from FUJIFILM Wako Chemicals, Japan, through a standard melt quenching method. Stoichiometric amounts of Na_2CO_3, V_2O_5 and H_3PO_4 (aq. 85%) were thoroughly mixed and melted at 1200 °C for 20 minutes in an air atmosphere, utilizing a platinum crucible. The molten mixture was then poured into carbon molds and annealed at 450 °C for 20 minutes. Subsequently, the glasses were cooled slowly to room temperature at a rate of 20 °C per hour.

4-2-2 Proton injection by APS

To facilitate proton injection, the cylindrical-shaped precursor glass obtained after annealing was cut into 0.8 mm thick disks with an 18 mm diameter as shown in Figure 4-1 (a). A 100 nm thick palladium (Pd) thin film was deposited on one surface of the disk using magnetron sputtering (JFC-1600, JEOL, Japan). The disk, with the Pd-film side facing upwards, was placed in a sample holder where the other side was in contact with a molten tin cathode in an H_2 atmosphere. APS by applying a DC voltage of 10 V in the temperature range of 320−380 °C for 8−9 hours using the apparatus as shown in Figure 4-1 (b). Detailed information about the APS apparatus and working conditions can be found in chapter 1 [11-12]. The glass nature of the specimen after APS was checked by conducting X-ray diffraction (XRD) using Cu Kα radiation (SmartLab, Rigaku, Japan).

4-2-3 Electrical properties

To evaluate the electrical properties, disk-shaped glasses were used. Gold (Au) thin-film electrodes with a thickness of 200 nm were deposited on both surfaces of the disk using magnetron sputtering. I employed an AC impedance method and an impedance analyzer (ModuLab, Solartron Analytical, UK) to measure the electrical conductivity in a dry 5% H_2/95% N_2 atmosphere. The mean transport number of protons in the glasses was determined by measuring the electromotive force (EMF) of a hydrogen concentration cell:

$$\text{gas (I), Pd} \mid x\text{W-glass (electrolyte)} \mid \text{Pd, gas (II)} \qquad \text{4-1}$$

In gas (I), the hydrogen partial pressure was regulated at 1 atm through the continuous flow of H_2 gas, while in gas (II), the hydrogen partial pressure was controlled by diluting H_2 with N_2.

4-2-4 Characterization

For characterization purposes, I determined the glass transition temperature (T_g) using thermomechanical analysis (TMA) with a TD5000SA instrument (Bruker AXS, US). The test samples were subjected to an applied load of 68 mN mm^{-2}, and the temperature was increased at a rate of 20 °C min^{-1}. The sodium concentrations (C_{Na}) in the glass before and after APS were determined using an energy dispersive X-ray spectrometry (EDX) system (JED 2300, JEOL, Japan) integrated into a field emission scanning electron microscopy (FE-SEM) instrument (SU6600, Hitachi, Japan). Fourier-transform infrared spectroscopy (FT-IR; FT/IR-6100, JASCO, Japan) was employed to obtain infrared absorption spectra in the O−H stretching vibration region (v_{OH}) for evaluating O–H bonding characteristics and the concentration of OH groups corresponding to proton concentration. The concentration of OH groups, denoted as C_{OH} and measured in cm^{-3}, was determined from the maximum absorption intensity v_{OH} ($\alpha(v_{OH})$), by employing equation 4-2 [13]:

$$C_{OH} = 1.03 \times 10^{19} \times \alpha(v_{OH}) \qquad\qquad 4\text{-}2$$

Raman spectra were obtained using a laser Raman spectrometer (NRS-3100, JASCO, Japan) with an excitation wavelength of 532 nm. The V 2p core-level X-ray photoelectron spectra (XPS) were examined using a PHI5600 spectrometer (ULVAC-PHI Inc., Japan) equipped with a hemispherical electron analyzer. Excitation was achieved using monochromatic Al-Kα radiation (hv=1486.6 eV) as the source. To ensure surface integrity, all glass samples were prepared under a dry N_2 atmosphere and scraped to expose a fresh surface immediately prior to analysis. The samples were then placed on a gastight sample holder and loaded into the preparation chamber of the XPS apparatus, ensuring no exposure to air. During spectra recording, the residual pressure in the analyzing chamber was maintained at approximately 5×10^{-7} Pa. The binding energy of the system was calibrated at 284.8 eV using the C 1s core level for reference to account for potential carbon contamination [14,15].

4-3 Results and discussion

4-3-1 Proton injection by APS

The 9 precursor glasses were prepared based on the glass forming region reported by Ungureanu et al. in 2000, as shown in Figure 4-1 [16]. Of these, 8 glasses were successfully synthesized within the glass forming region and confirmed to have an amorphous structure through XRD pattern analysis (Glass 1 and 6 in the Figure 4-2), while glass 9 was found to be crystallized, as evidenced by sharp peaks observed in the XRD pattern (Glass 9 in Figure 4-3). All the precursor glasses exhibited varying shades of green coloration, which is typical for vanadium phosphate glasses due to the presence of mixed valence states of V^{5+} and V^{4+} [6,17,18]. APS was conducted on the above 8 glasses with different APS conditions such as temperature and voltage. The optimized APS conditions were only achieved for glass

6, as the thin range between its glass transition temperature (T_g) and crystallization temperature (T_c) caused crystallization in the other glasses, such as glasses 1 and 7 (Figure 4-4).
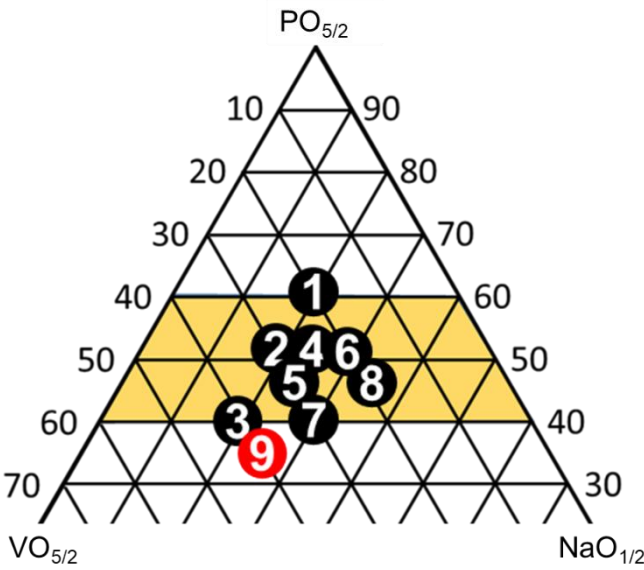
Figure 4-1 The 9 precursor glass compositions prepared in reported glass forming region [16].
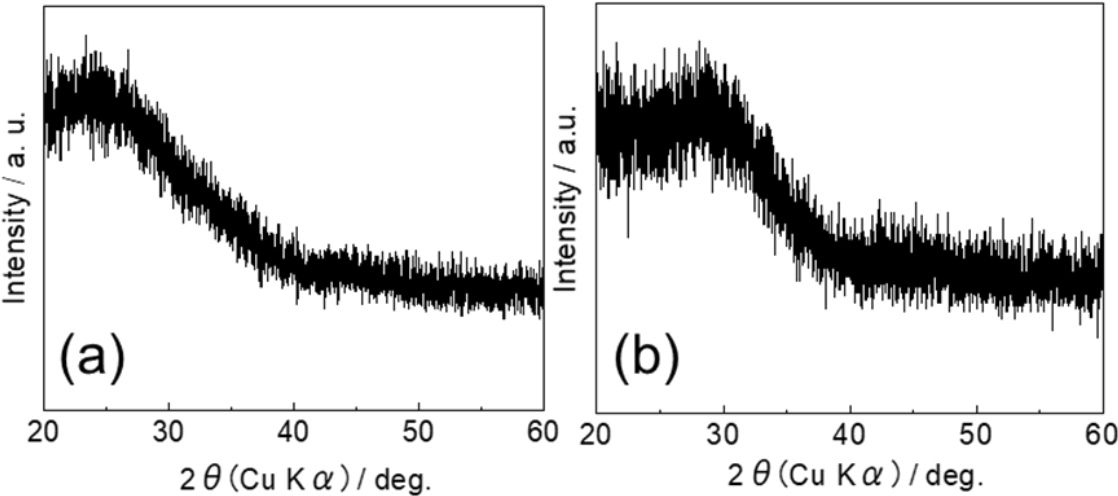

Figure 4-2 XRD pattern of the glasses before alkali-proton substitution (APS) (a) glass 1 and (b) glass 6.

The glass composition $30NaO_{1/2}-20VO_{5/2}-50PO_{5/2}$ was synthesized, and APS was conducted under varying temperature and voltage conditions to determine the optimal parameters. However, APS performed APS carried out at 380 °C with 5 V applied DC voltage led to glass crystallization (Figure 4-5a) as the temperature, 380 °C was higher than the crystallization temperature of the glass after APS, while at 320 °C with 10 V applied DC voltage resulted in complete glass breakage (Figure 4-5b) due to high viscosity at lower temperature to conduct APS. Eventually, the desired glass state was achieved by conducting APS at 340 °C with a 10 V applied DC voltage (Figure 4-5c).
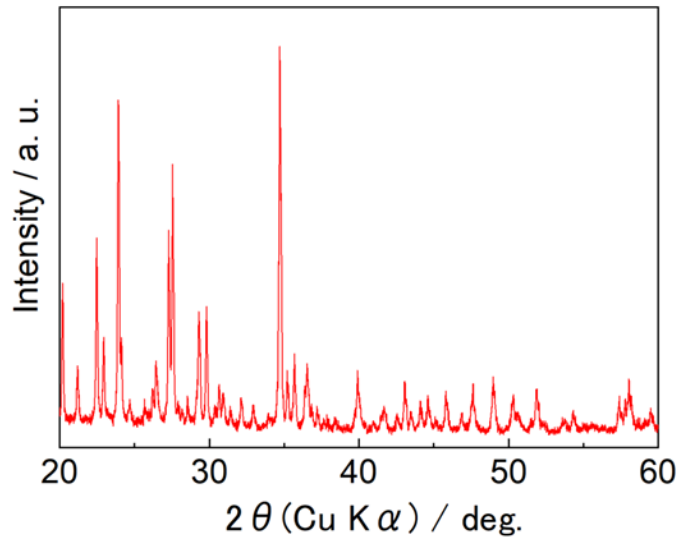
Figure 4-3 XRD pattern of the glass 9 before alkali-proton substitution (APS).
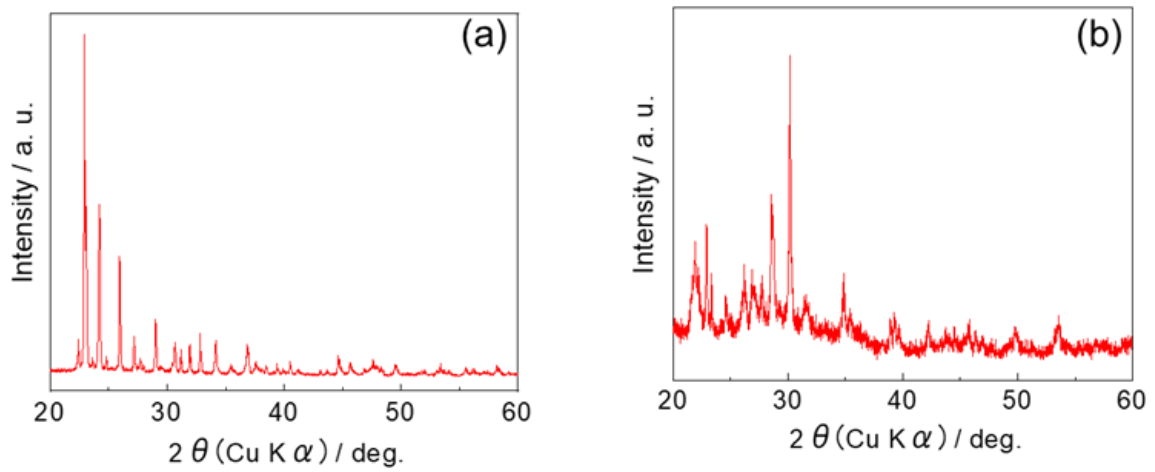
Figure 4-4 XRD pattern of the (a) glass 1 and (b) glass 7 after alkali-proton substitution (APS).
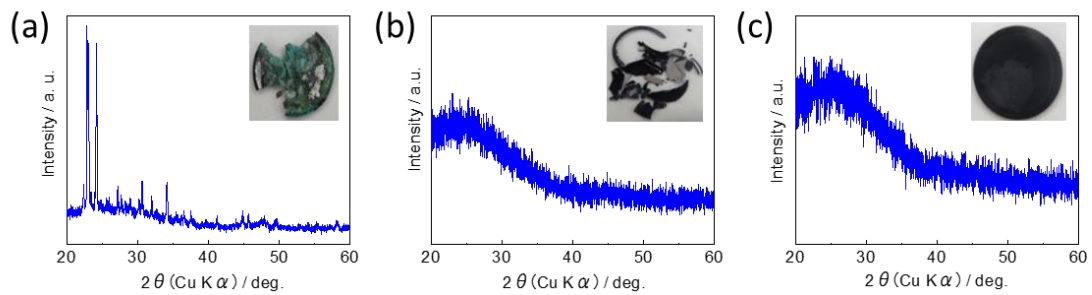
Figure 4-5 XRD pattern and photographic images of the glass with APS conducted: (a) 380 °C at 5 V, (b) 320 °C at 5 V, and (c) 340 °C at 10 V.

Figure 4-6 displays the depth profiles of Na and OH concentrations (C_{Na} and C_{OH}) in the glass before and after APS (indicated by dashed lines). After APS, over 95% of Na ions were discharged from the glass, while a substantial amount of OH was introduced into the glass. The absolute changes, ΔC_{Na} and ΔC_{OH}, were measured to be -7.7×10^{21} cm^{-3} and 8.3×10^{21} cm^{-3}, respectively, confirming the successful electrochemical substitution of Na$^+$ ions with protons. Thus, successful synthesis of $29HO_{1/2}-1NaO_{1/2}-20VO_{5/2}-50PO_{5/2}$ glass was achieved through APS. The glasses exhibited shades of green both before and after APS (Figure 4-7), indicating the presence of both V^{5+} and V^{4+} ions, consistent with previous reports [6,17,18]. The low basicity of glass after APS is attributed to the low concentration of NaO$_{1/2}$ or the presence of HO$_{1/2}$, transition metals such vanadium ions tend to adopt lower valence states of V^{4+} as suggested by color [19-20].
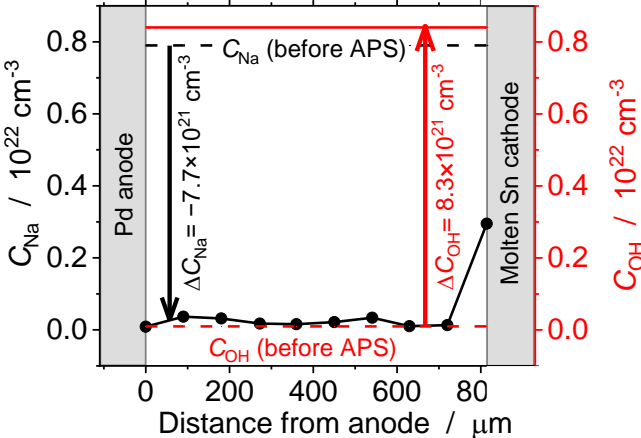
Figure 4-6 Depth profiles of C_{Na} (black dots) and C_{OH} (red solid line) for glass after alkali-proton substitution (APS). The black and red dashed lines indicate C_{Na} and C_{OH}, respectively, for the glass before APS.
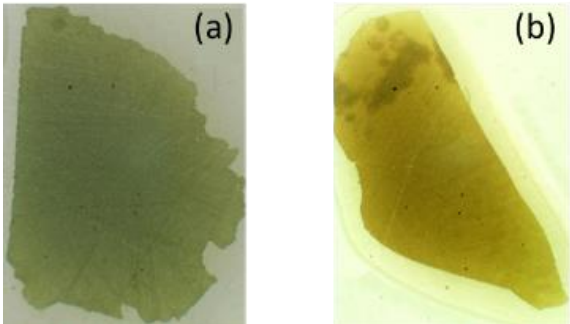
Figure 4-7 Photographic images of the glasses (a) before and (b) after alkali-proton substitution (APS).

4-3-2 Thermal stability

Figure 4-8 presents the thermal expansion curves for the glass before and after APS. The T_g of the glass decreased from 422°C before APS to 245°C after APS, primarily due to the increase in [OH] content [21]. In comparison with the glass containing 20 mol% of conditional glass former the obtained

T_g is quite reasonable. On comparing with reported glasses obtained with APS method containing various proton concentration and oxide components, the T_g is found to be higher in the current glass after APS [22-23], the addition of vanadium ions to the glass structure significantly enhanced T_g, thereby improving the glass's thermal stability. This phenomenon of increased T_g has been reported in various phosphate glasses and is attributed to the formation of heteroatomic P−O−V bonds via VO_6 octahedra units, which create strong cross-links within the phosphate glass networks [1-2]. Further insights into the structural analysis based on Raman spectra will be discussed in subsequent sections, shedding light on the specific bonding configurations and structure of the glass.

4-3-3 AC impedance spectroscopy

Impedance measurements were performed during heating cycle for the glass before APS, and the resulting data is presented in Figure 4-9, showing the Nyquist plot depicting the complex impedance diagram of the glass as temperatures increase from (a) to (b) in Figure 4-9. At low temperature of 155 °C, two semicircles were observed at relatively higher frequency ($1MHz > f > 1KHz$) and lower frequencies ($1KHz > f > 1Hz$) regions, with similar sizes. As the temperature increased from 155 to 320 °C, the size of the lower frequency semicircle decreased compared to the higher frequency semicircle. At high temperatures of around 300°C, the lower frequency semicircle almost disappeared. On the other hand, Impedance measurements were performed during heating cycle for the glass after APS, and the resulting data is presented in Figure 4-10, showing the Nyquist plot depicting the complex impedance diagram of the glass as temperatures increase from (a) to (b) in Figure 4-10. In the higher frequency region (1 MHz to 1 kHz), the data points form a single semicircle positioned below the real axis. Furthermore, the impedance plot displayed a distinct capacitive spike, characteristic of a blocking electrode [24-26].
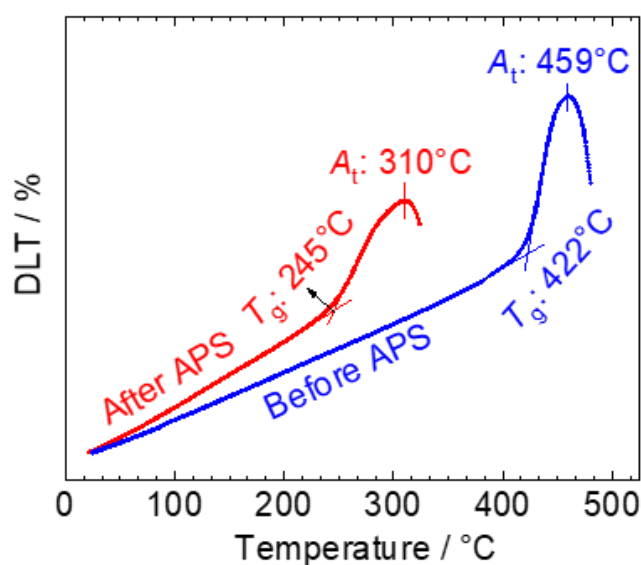
Figure 4-8 Glass transition temperature (T_g) of the glasses before and after alkali-proton substitution (APS).
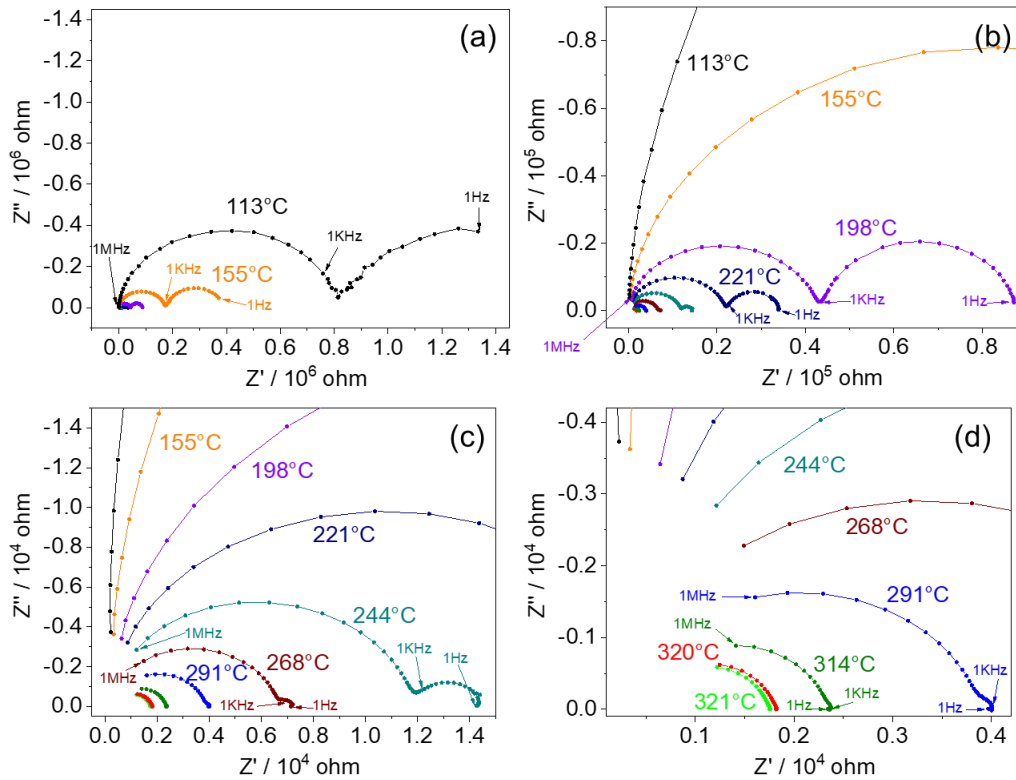
Figure 4-9 Comparison of Nyquist plot with increasing temperature from (a) to (d) for the glass before alkali-proton substitution (APS).

These semicircles observed at high frequencies can be attributed to the parallel combination of bulk resistance (R_b) and bulk capacitance (C_b) of the glass [27]. The capacitance values were determined at the maximum frequency using the relationship $2\pi f_{max}RC = 1$. Typically, the experimentally obtained semicircle exhibited a capacitance value that closely approximated an order of 10 pF, indicating conduction through the bulk of the material [27]. As anticipated, at elevated temperatures, the bulk resistance decreased, leading to a decrease in the semicircle diameters associated with it. Consequently, the capacitive blocking spike remained observable throughout the measured frequency range. However, it is important to note that vanadium phosphate glasses are known to exhibit mixed ionic and electronic conductivity [28-30]. Therefore, a comparison between the glasses before and after APS was performed using equivalent circuit fitting.

To analyze the characteristics of the Nyquist impedance plot, it is common practice to employ an equivalent circuit due to its simplicity, efficiency, and ability to provide a comprehensive understanding of the system. In this study, the focus was on determining the bulk resistance of the glasses, which can be derived from the equivalent circuit. The proposed equivalent circuit (Figure 4-11a) for systems exhibiting mixed ionic and electronic conductivity is relatively straightforward. It consists of a parallel combination of ionic resistance (R_i) and electronic resistance (R_e) in parallel with their respective chemical capacitances, representing the bulk portion of the system [31-32]. These elements are further connected in series with their corresponding interface impedances. The Nyquist plot displays depressed

semicircular arcs with their centers positioned below the Z' axis. To achieve better fitting results, common phase elements (CPEs) were used instead of capacitances. Additionally, a geometrical capacitance (C_{geom}) was included in the circuit to account for changes in capacitance solely due to the system's geometry. This capacitance typically has a small value in the order of 10 pF.
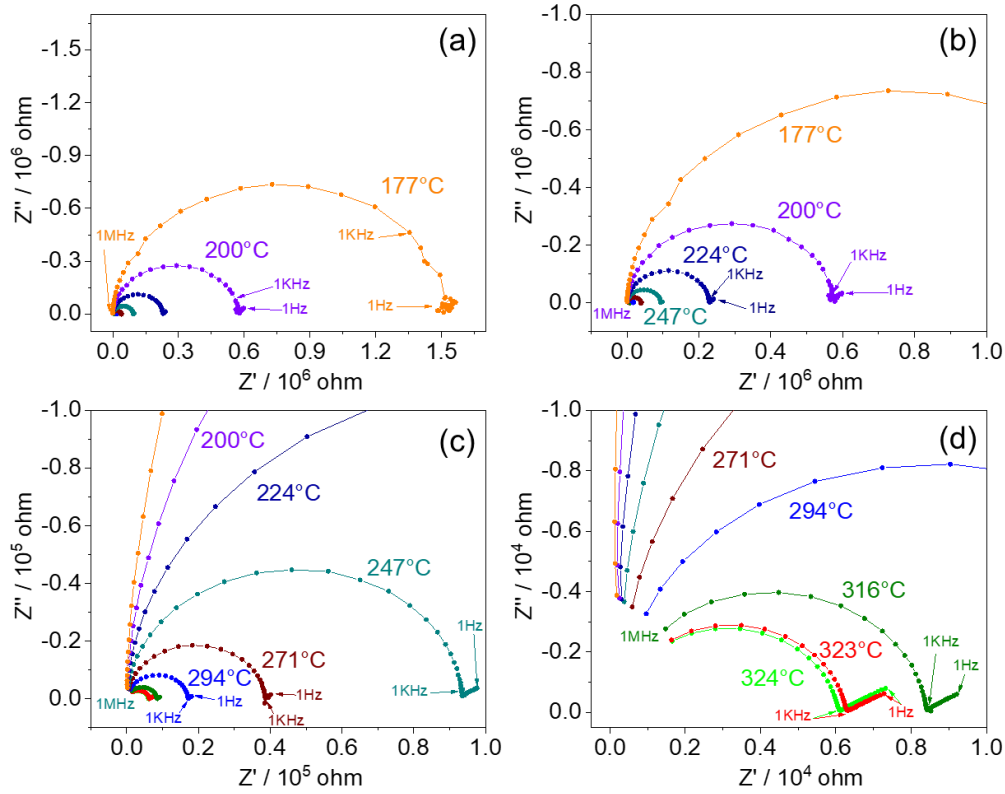

Figure 4-10 Comparison of Nyquist plot with increasing temperature from (a) to (d) for the glass after alkali-proton substitution (APS).

By utilizing gold electrodes, a simplified circuit (Figure 4-11b) was employed over a variable frequency range spanning from 1 MHz to 1 Hz [31-32]. At relatively higher frequencies, all the capacitances effectively short circuit, resulting in an impedance that is a parallel combination of the electronic and ionic circuits. On the other hand, at lower frequencies, all the capacitances effectively open circuit, leading to an impedance that is solely electronic due to the blockage of ion transfer and zero resistance to electron transfer provided by the gold electrode. Based on the proposed equivalent circuit, the first intercept (R_1) at the real axis represents a parallel combination of electronic and ionic resistances, as described by Equation 4-3. Similarly, the second intercept (R_2) represents the electronic resistance, as described by Equation 4-4.

$$\frac{1}{R_1} = \frac{1}{R_e} + \frac{1}{R_i} \qquad\qquad 4\text{-}3$$

$$R_2 = R_e \qquad\qquad 4\text{-}4$$
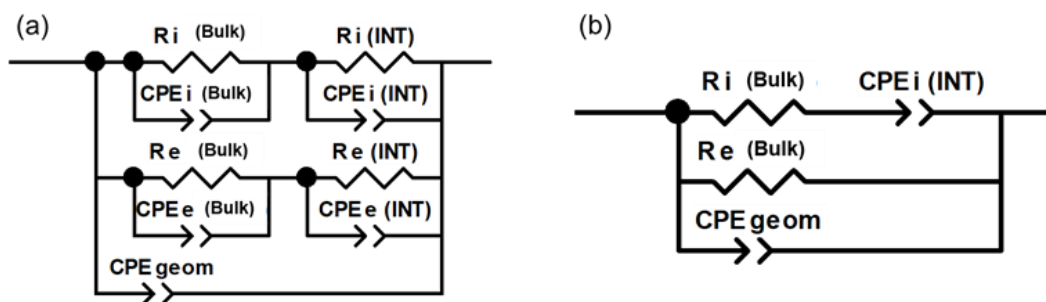
Figure 4-11 (a) Equivalent circuit for mixed ionic and electronic conductor, (b) Simplified version of (a)
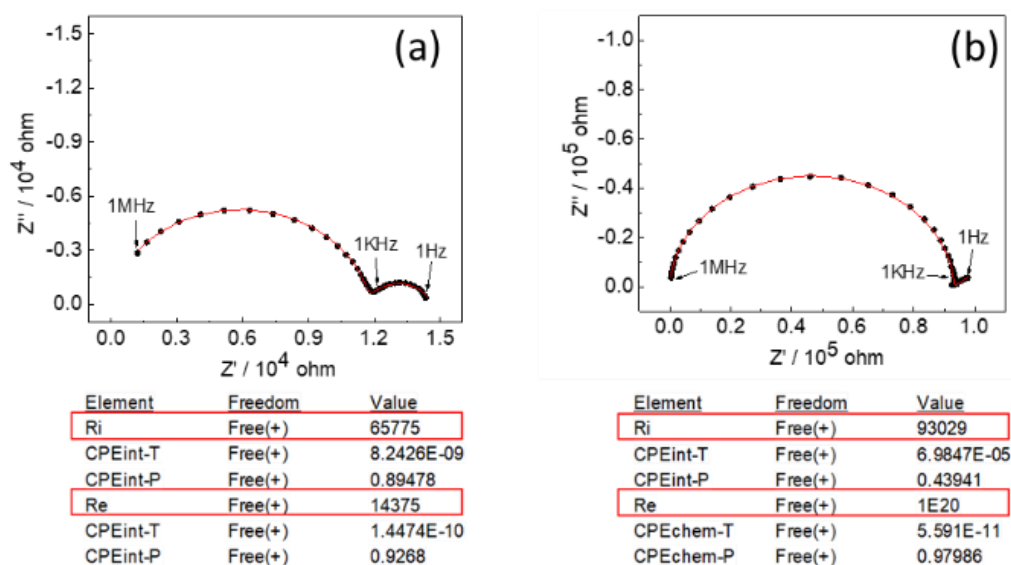
Figure 4-12 (a) and (b) depict the fitting results (red solid line) overlaid on the original data points (black dots) obtained at 250 °C for the glasses before and after APS, respectively. The fitting results exhibited excellent agreement with the experimental data. Consistent with expectations, the presence of a finite electronic resistance was observed in the glass before APS, indicating mixed sodium ion and electronic conductivity. In contrast, after APS treatment, the electronic resistance approached infinity, indicating exclusive protonic conductivity.

Element	Freedom	Value
Ri	Free(+)	65775
CPEint-T	Free(+)	8.2426E-09
CPEint-P	Free(+)	0.89478
Re	Free(+)	14375
CPEint-T	Free(+)	1.4474E-10
CPEint-P	Free(+)	0.9268

Element	Freedom	Value
Ri	Free(+)	93029
CPEint-T	Free(+)	6.9847E-05
CPEint-P	Free(+)	0.43941
Re	Free(+)	1E20
CPEchem-T	Free(+)	5.591E-11
CPEchem-P	Free(+)	0.97986

Figure 4-12 The equivalent circuit fitting results (red solid line) overlaid on the original data points (black dots) obtained at 250°C for the glasses (a) before and (b) after alkali-proton substitution (APS).

In Figure 4-13, electromotive force (EMF) measurements of hydrogen concentration cells utilizing glass after APS as electrolytes were conducted at 250 °C. The results indicated a t_H value of unity for the glass after APS, signifying that the glass serves as a pure proton-conducting electrolyte. The 100% proton transport number inferred from both the Nyquist and EMF data supports a discussion on the protonic conductivity exhibited by the glass after APS.
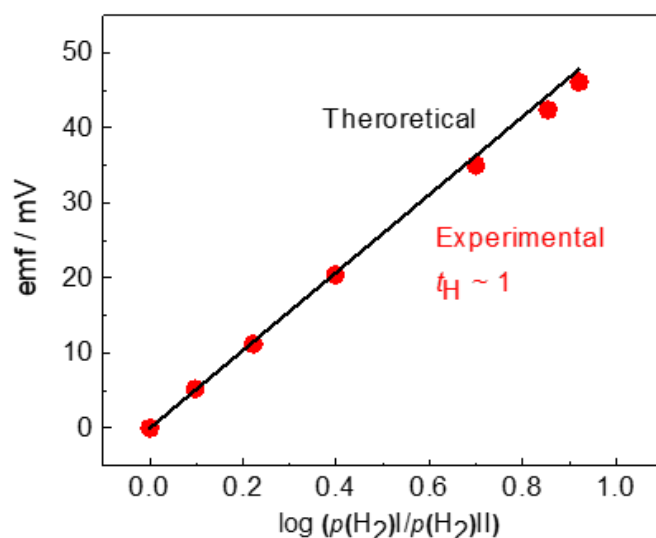
Figure 4-13 Electromotive forces (EMFs) for the hydrogen concentration cell as a function of logarithmic hydrogen partial pressure, $p(H_2)$, ratio at 250 °C for glass after alkali-proton substitution (APS). The theoretical emfs calculated using the Nernst equation, E= $(RT/2F)$ $\ln(p(H_2)_{high}/p(H_2)_{low})$ are shown as black lines.

4-3-4 Electrical conductivity

Figure 4-14 displays the Arrhenius plot of the electrical conductivity for glass before APS. Based on fitting data of glass before APS, an Arrhenius plot was plotted for mixed ionic and electronic conductivity with total conductivity represented by red dots, electronic conductivity by blue open triangles, and sodium ions conductivity by green open triangles. The total conductivity for the glass before APS ranged from 10^{-7} to 10^{-4} S cm^{-1} within a temperature range of 150−300 °C. It was observed that the glass before APS showed mixed conductivity up to 200 °C, after which electronic conductivity dominated and sodium ions conductivity reduced significantly.

Figure 4-15 illustrates the Arrhenius plot of the proton conductivity for the glass after APS, with the glass transition temperature (T_g) indicated by a small black triangle. The temperature range examined in the plot spans from 120 to 320 °C, and the proton conductivity ranges from 10^{-8} to 5×10^{-5} S cm^{-1}. The activation energy (E_a) for proton conduction obtained from the $\ln(\sigma T)$ vs. $1/T$ plot. The calculated E_a till T_g value of 0.81 eV suggests that the proton conductivity in this glass follows a proton hopping mechanism similar to that observed in other phosphate glasses [23]. The experimentally calculated μ_H at T_g was 1.8×10^{-9} cm^2 V^{-1} s^{-1}, which was calculated using the proton conductivity at T_g and the proton carrier density (n_H), assuming that all protons forming OH groups are mobile ($n_H = C_{OH}$). Upon comparison with reported values for glass obtained with APS method [23], the experimentally obtained μ_H at T_g is found to be at lower end of the converged value of μ_H at T_g, 2×10^{-9} to 2×10^{-7} cm^2 V^{-1} s^{-1} [23], suggesting that the inclusion of VO$_{5/2}$ has a negative effect on proton mobility in the glass.
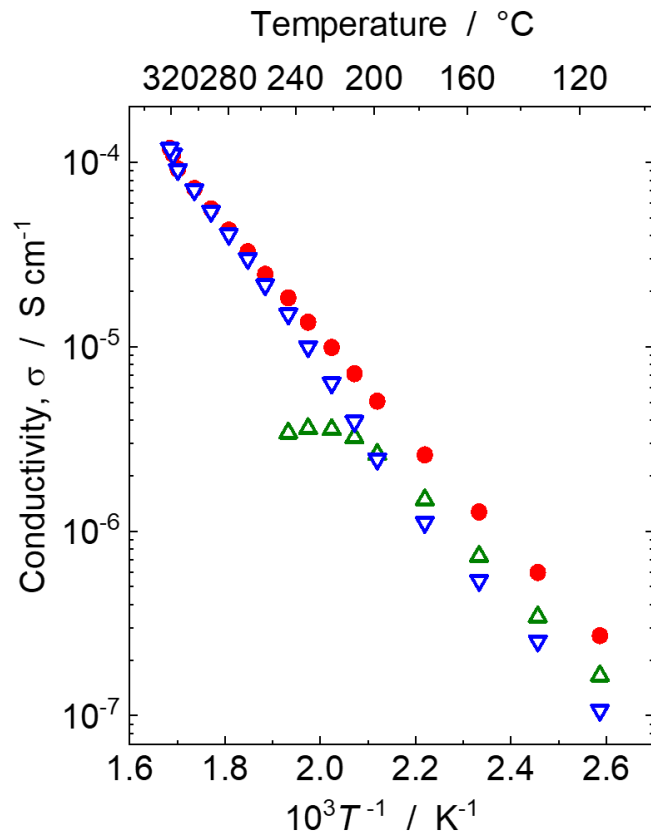
Figure 4-14 Arrhenius plot of the electrical conductivity of the glass before alkali-proton substitution (APS).
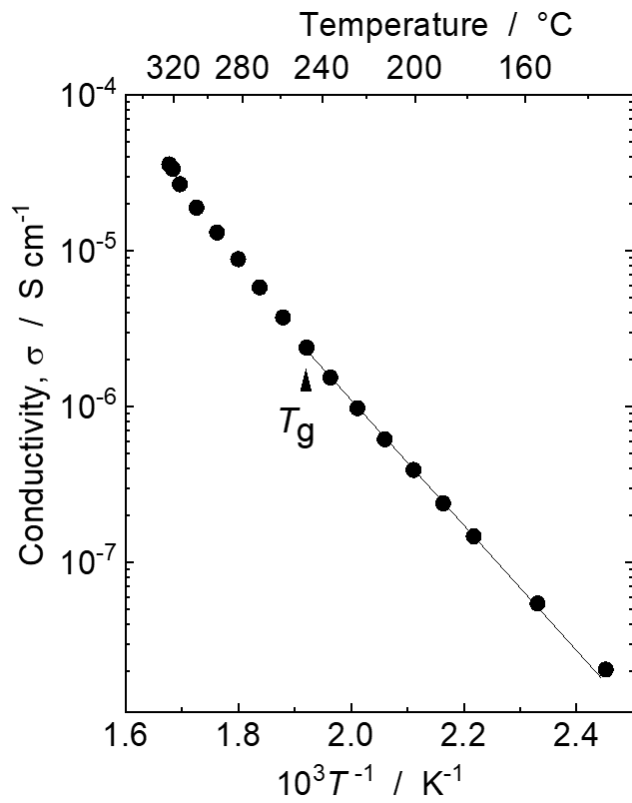

Figure 4-15 Arrhenius plot of the proton conductivity of the glass after alkali-proton substitution (APS). The triangle corresponds to the proton conductivities at the glass transition temperature (T_g) of the glass.

In summary, the experimental results indicate that the incorporation of $VO_{5/2}$ into phosphate glasses improved the thermal stability but leads to relatively low proton mobility than other reported phosphate glasses prepared using APS method, which in turn affects proton conductivity. These findings suggest that $VO_{5/2}$ may not be a favorable oxide component for enhancing the properties of proton-conducting phosphate glasses. Subsequently, the discussion will delve into the influence of vanadium ion concentration, glass structure, and the nature of O−H bonding on T_g and proton mobility.

4-4 Vanadium mixed valence and glass structure

The enhanced thermal stability observed in phosphate glasses upon the addition of $VO_{5/2}$ can be attributed to the formation of P−O−V bonds, which effectively interconnect the phosphate glass network [1-2]. Therefore, it is crucial to investigate the formation of these bonds. Figure 4-16 presents the core level spectra of V $2p_{3/2}$ for both the glasses before and after APS, where the broad peak positions align with previously reported data for vanadium phosphate glasses [33-35]. However, a detailed analysis of the V $2p_{3/2}$ spectra reveals an asymmetry on the lower binding energy side, indicating the presence of vanadium ions in multiple oxidation states. This observation is also consistent with the color changes observed in the glasses before and after APS. Consequently, the spectra was fitted using two Gaussian-Lorentzian peaks, with the lower binding energy peak corresponding to V^{4+} and the higher binding energy peak corresponding to V^{5+}. Table 4-1 presents the results of the two-peak fitting, including the peak positions and the relative abundance of each oxidation state. The V^{4+}/V^{total} ratio varies from 50% for the glass before APS to almost 70% for the glass after APS. After APS, a reduction in the abundance of V^{5+} to V^{4+}, resulting in a shift from vanadium acting primarily as a glass former with V^{5+} to an intermediate oxide state with V^{4+}, based on the finding of the previously reported reports on vanadium phosphate glasses, which highlight the role of V^{5+} as a glass former and V^{4+} as an intermediate oxide [3,36]. Based on these results, the composition obtained after APS is determined to be $29HO_{1/2}−1NaO_{1/2}−14VO_2−6VO_{5/2}−50PO_{5/2}$.

Table 4-1 V 2p core-level XPS spectra fitting results for before and after APS.

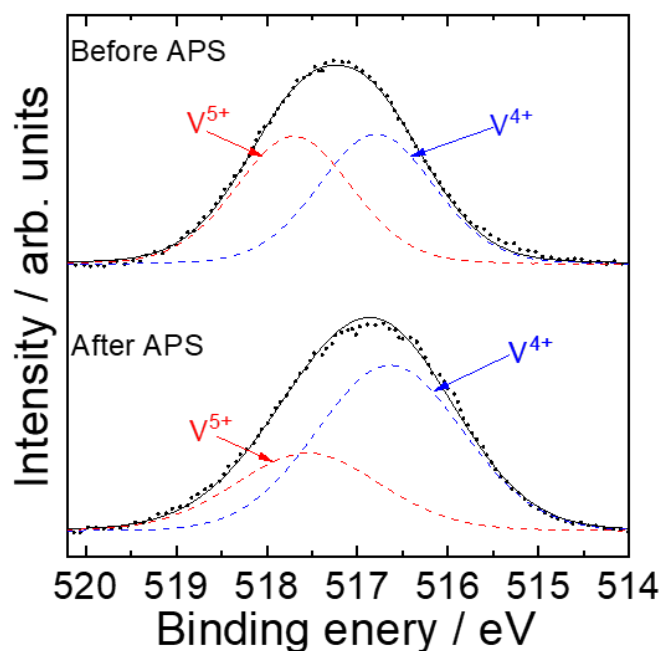| Band	Before APS			After APS		
	Pos	FWHM	%Area	Pos	FWHM	%Area
V^{4+}	516.79	1.51	50.4	516.64	1.90	69.7
V^{5+}	517.70	1.51	49.6	517.55	1.90	30.3

Figure 4-16 V 2p core-level X-ray photoelectron spectroscopy (XPS) spectra of the glasses before and after alkali-proton substitution (APS).

The Raman spectra of the glass before and after APS treatment is presented in Figure 4-17 and the assignments of the bands are summarized in Table 4-2. In the glass before APS, the prominent bands observed in the spectral range of $900-1000$ cm^{-1} correspond to the stretching modes of V=O and V−O^{-} bonds [37-39], indicating the presence of NBOs on VO$_x$ units. The bands located at approximately 700 cm^{-1} and 1180 cm^{-1} can be attributed to the symmetric stretching vibrations of the P−O−P bond for the Q^2 unit (v_{sym}(P−O−P)Q^2) and the symmetric stretching vibrations of the O−P−O bond for the Q^2 unit (v_{sym}(PO$_2$)Q^2), respectively [40-42]. These spectral features primarily represent the phosphate framework of the glass. This indicates that the main phosphate ion contributing to the glass network is the chain-type ion (PO$_3{}^{3-}$)$_l$. An important band is observed at 626 cm^{-1}, which is attributed to P−O−V heteroatomic linkages and a band at 757 cm^{-1} was attributed to V−O−V stretching vibrations [37,39]. The glass after APS, the most distinctive change observed in the phosphate framework is the noticeable shift of the $v_{P-O-P, sym}$(Q^2) band at ~700 cm^{-1} towards a higher frequency. This significant shift of the $v_{P-O-P, sym}$(Q^2) band is primarily attributed to a decrease in chain length, resulting in the fragmentation of phosphate chains composed of inner Q^2 units and two terminal Q^1 units, represented as (PO$_3{}^{-}$)$_l$(P$_2$O$_7{}^{4-}$). By analyzing this shift, we can infer the reduction in chain length and the associated fragmentation of the phosphate structure in the glass after APS. Another notable change observed in the phosphate framework is the fluctuation in the intensity of the $v_{PO2, sym}$(Q^2) band at ~1162 cm^{-1}, which exhibited a significant decrease as the substitution of Na$^+$ with protons happened. This decrease in intensity can be attributed to the fact that protons possess a significantly lower polarizability compared to Na$^+$ ions. It is important to consider that the intensity of the Raman band is directly influenced by

changes in polarizability. The prominent bands observed in the spectral range of 900−1000 cm^{-1} correspond to the stretching modes of V=O and V−O$^-$ bonds [37-39], indicating the presence of NBOs on VO$_x$ units. The bands in the 900-1000 cm^{-1} range exhibited a noticeable shift towards higher frequencies, indicating a change in the coordination number of vanadium ions in the glass after APS. An important band is observed at 626 cm^{-1}, which is attributed to P−O−V heteroatomic linkages [37,39]. The relative intensities of P−O−V and V−O−V vibrations bands at 620 cm^{-1} and 750 cm^{-1}, respectively, both decreased after APS, and the relative intensity of V−O band at 900 cm^{-1} increased significantly. These observations suggest further fragmentation of the phosphate chains in the glass after APS and formation of more NBOs related to the vanadium ions polyhedral units. Based on the information obtained from V 2p core level spectra and Raman Spectra, the postulated glass structure were found to be different before and after the APS as illustrated in the Figure 4-18.
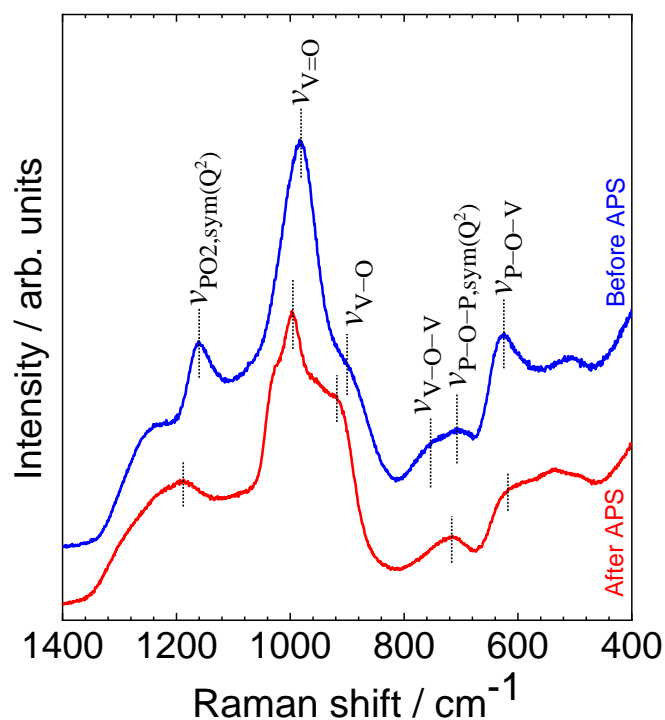
Figure 4-17 Raman spectra of the glasses before and after alkali-proton substitution (APS).

Table 4-2 Assignment of the Raman bands observed for glass before and after alkali-proton substitution (APS).

Assignment	Position / cm^{-1} Before APS	After APS		Ref.
ν_{P-O-V}	626	607	Symmetric stretching vibrations of V–O–P linkages	37,39
$\nu_{P-O-P,\,sym}$(Q^2)	706	718	Symmetric stretching mode of the P–O–P bond for the Q^2 unit	40-42
ν_{V-O^-}	895	918	Stretching mode of the V-O$^-$ bond of VO$_x$ polyhedra	37-39
$\nu_{V=O}$	982	996	Stretching mode of the V=O bond of VO$_x$ polyhedra	37-39
$\nu_{O-P-O,\,sym}$(Q^2)	1159	1189	Symmetric stretching mode of NBOs for the Q^2 unit	40-42
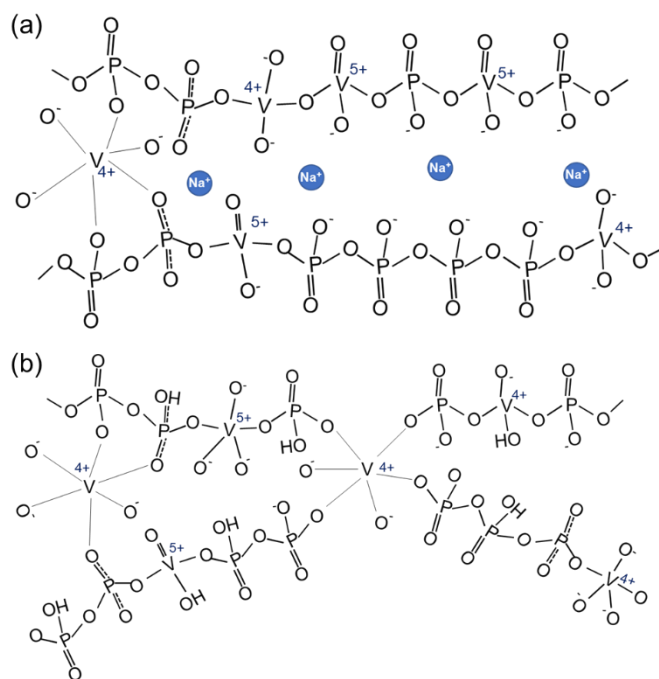
Figure 4-18 Glass structure illustration of the glasses (a) before and (b) after alkali-proton substitution (APS).

4-4-1　Suppressed electronic conductivity in the glass after APS

The observation of only protonic conductivity in the glass after APS, as evidenced by impedance spectroscopy and EMF analysis, was surprising considering the well-known electronic conductivity exhibited by vanadium oxide-containing phosphate glasses before APS. This suggests that the suppressed electronic conductivity in the glass after APS is likely a result of changes in both the valence states of vanadium ions and the glass structure caused by the substitution of sodium ions with protons. V 2p core level spectra showed a decrease in polaron acceptor sites (V^{5+}) from 50% before APS to almost 30% in the glass after APS, resulting in reduced polaron hopping between the acceptor and donor sites. Also, Raman spectra analysis reveals that the introduction of $HO_{1/2}$ disrupts the P−O−V and V−O−V linkages, leading to the formation of non-bridging groups associated with VO_x polyhedra. These non-bridging groups impede electron transfer between the mixed valence of vanadium ions, thereby reducing electron mobility. Consequently, an increase in the $HO_{1/2}$ content leads to a significant decrease in polaronic conductivity due to an increased proton-polaron interaction as proton concentration significantly increased in the glass after APS. This is similar to ion-polaron effect that has been reported in similar kinds of phosphate glasses containing vanadium oxide [39].

As the number of H^+ surpasses the number of trapping polarons, the protonic conductivity dominates in the glass after APS. These structural changes induced by proton substitution may have also resulted in the formation of new sites for protonic conduction, which contribute to the overall protonic conductivity of the glass. These newly formed sites offer pathways for protons to migrate and contribute to the observed protonic conductivity.

In summary, the absence of electronic conductivity after APS in the glass can be attributed to a combination of changes in vanadium ion valence and glass structure induced by the proton substitution. The disrupted P−O−V and V−O−V linkages, formation of non-bridging groups, and increased separation between unpaired polarons all contribute to the suppression of electronic conductivity. However, further investigation is needed for better understanding of the suppression of the electronic conductivity after APS. Additionally, the increased proton concentration and presence of new sites for protonic conduction enhances the overall protonic conductivity in the glass.

4-4-2 Origin of enhanced thermal stability and low proton mobility

Thermal stability

Based on the V $2p_{3/2}$ core level XPS spectra data, it was determined that approximately 70% of the vanadium ions exist in the V^{4+} oxidation state, while the remaining 30% are in the V^{5+} oxidation state. It has been previously reported that V^{4+} acts as an intermediate oxide, contributing to the formation of VO_6 octahedra units through P−O−V heteroatomic linkages [1-3]. On contrary, V^{5+} primarily forms VO_4 or VO_5 units and serves as a glass former within the phosphate chains [36]. The analysis of the Raman spectra provides evidence for the existence of P−O−V heteroatomic linkages and the presence of VO_6 units within the glass structure. These findings support the notion that cross-linkages occur between the one-dimensional $(PO^{3-})_l$ chains through P−O−V bonds, facilitated by the incorporation of VO_6 octahedra. A three-dimensional network glass structure is formed after APS. This three-dimensional network contributes to the observed high glass transition temperature (T_g) and improved thermal stability of the glass.

Proton mobility

The Raman spectra analysis has confirmed the presence of non-bridging oxygen (NBO) sites associated with the vanadium ions units within the glass structure. These NBOs play a crucial role in understanding the migration of protons within the glass. The long-range migration of protons in the phosphate glasses follows two elemental migration paths: intra-phosphate chain migration and inter-phosphate chain migration. It should be noted that approximately 6 mol% of V^{5+} ions are present within these phosphate chains, and each of VO_4 and VO_5 units typically contains 1 or 2 NBOs. Specifically, in the case of intra-phosphate proton hopping, protons are required to migrate through the NBOs of the VO_4 or VO_5 units that are incorporated within the phosphate chains. Additionally, the VO_6 units, which are attributed to the V^{4+} oxidation state and constitute around 14 mol% of the glass composition, contribute at least 2 NBOs each. Therefore, in the process of inter-phosphate proton hopping, protons are also migrating through the NBOs of the VO_6 units. Considering the overall composition of the glass after APS, which includes 29 mol% of protons assuming they all are mobile and contribute to proton

conductivity, the presence of NBOs associated with the vanadium ions units is of utmost importance for determining proton mobility within the glass structure. For better understanding, an analysis of the OH stretching vibration region in the Infrared (IR) spectra was conducted to investigate the nature of OH bonding.

In Figure 4-19, the FT-IR spectra obtained in the OH stretching vibration region reveal a broad and intense peak located at a high wavenumber region 3280 cm^{-1} in the after-APS glass. Previous studies by Naruse et al. have investigated the O−H bonding in various alkaline earth phosphate glasses using IR spectroscopy [43]. Their findings indicate that the v_{OH} vibrations corresponding to the O−H bonding at Q^2 units, which correspond to the inner PO_4 units in $(PO_3^{-})_l$ chains, exhibit weak O−H bonding and strong hydrogen bonding at approximately 2800 cm^{-1}. Conversely, the O−H bonding at Q^1 units, corresponding to the terminal PO_4 unit in $(PO_3^{-})_l$ chains, demonstrates strong O−H bonding and weak hydrogen bonding at approximately 3300 cm^{-1}. Additionally, the O−H bonding in V−O−H units, associated with the NBOs of vanadium ions units has been reported to appear at 3200 cm^{-1} in previous reports [44]. Therefore, it is crucial to deconvolute the spectra into at least three peaks to enable a quantitative analysis of the nature of O−H bonding in the glass. However, it is important to note that the deconvolution of the spectra into three peaks is subjective and arbitrary. Alternatively, a direct discussion based on the observed peak positions can still provide valuable insights into the O−H bonding characteristics in the glass. The presence of a peak at 3281 cm^{-1} in the FT-IR spectra suggests the occurrence of strong O−H bonding and weak hydrogen bonding in the glass structure. The strong OH bonding leads to an increased dissociation energy barrier, hindering the movement of protons and ultimately resulting in low proton mobility.

The analysis of Raman spectra in the glass after APS did not reveal any bands associated with isolated Q^1 units, indicating their absence in the glass structure. The peak corresponding to v_{OH} associated with the OH bond in Q^2 units was reported to be observed around 2800 cm^{-1}, as explained earlier. Therefore, the dominant contribution to the broad peak observed at 3380 cm^{-1} can be attributed to v_{OH} associated with the OH bond in V−O−H units. Considering that vanadium units are incorporated within the phosphate chains, the presence of NBOs related to V^{4+} or V^{5+} units in the glass structure can be inferred. These NBOs create strong proton trapping sites, leading to a low proton mobility in the present glass.

In the reported case glass containing WO_3 having composition $20WO_3$-$35NaO_{1/2}$-$45PO_{5/2}$ (20W) glass [11], the introduction of protons in the 20W glass resulted in sufficient mobility throughout the temperatures range up to 350 °C. The partial conductivity of the proton reached 5×10^{-5} Scm^{-1} at 250 °C, indicating a promising level of proton conduction [11]. However, it is noteworthy that the electronic contribution to conductivity was significant, accounting for almost 70% of the total conductivity. The glass was reported to be mixed protonic and electronic conductivity, unlike the present case of $VO_{5/2}$. Comparing the IR spectra of the reported 20W glass with the present glass, distinct differences in the proton migration pathways are observed. In the 20W glass, the v_{OH} absorption of the present glass was found to be extremely broadened, indicating that the dominant pathway for proton migration mainly

consists of non-bridging oxygens (NBOs) associated with both PO_4 and WO_x polyhedra. This result highlighted the significant role of WO_3 in promoting proton mobility as also observed in previous chapter study of effect of addition WO_3. In the current glass composition containing vanadium oxide, a contrasting observation was made. Protons in this composition were found to preferentially associate with oxygens of VO_x polyhedras rather than PO_4. This distinction suggests that vanadium oxide plays a crucial role in the proton trapping mechanism. The presence of VO_x polyhedra seems to create favorable sites for strong proton trapping, potentially influencing the overall proton conductivity and migration behavior.
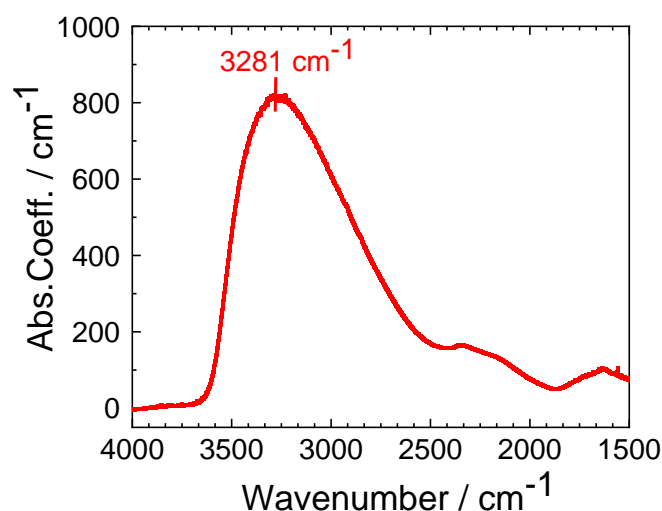
Figure 4-19 Infrared spectra in the ν_{OH} region of the glass after alkali-proton substitution (APS).

4-5 Conclusion

The effect of incorporating $VO_{5/2}$ into the $29HO_{1/2}-1NaO_{1/2}-14VO_2-6VO_{5/2}-50PO_{5/2}$ glass composition was investigated, focusing on the glass transition temperature (T_g) and proton mobility (μ_H). The addition of $VO_{5/2}$ resulted in high T_g, indicating better thermal stability. This enhancement can be attributed to the formation of tight cross-linkages between the phosphate ion chains through the formation of P−O−V heteroatomic linkages involving 6-fold coordinated vanadium (V) atoms. However, despite the positive influence on T_g, the addition of $VO_{5/2}$ in the glass composition led to low proton mobility. This can be attributed to the strong trapping of protons resulting in high proton dissociation energy.

The VO_2 species acts as a conditional glass former, contributing to the cross-linking of phosphate chains and the formation of a three-dimensional network in the glass structure. It is important to note that the effect on μ_H at T_g observed in $VO_{5/2}$ differs from the behaviour observed in WO_3. In WO_3, proton migration is enhanced was attributed to the reduction in the energy barrier for inter-phosphate chain proton migration, facilitated by formation of P−O−W linkages. In contrast, in the case of $VO_{5/2}$, the

presence of NBOs related to V^{4+} or V^{5+} units in the phosphate network leads to the creation of strong proton trapping sites. This strong trapping effect results in a low proton mobility. The difference in behaviour between WO_3 and $VO_{5/2}$ can be attributed to the specific characteristics of the NBOs, and the glass-forming units associated with each oxide.

References

1. A. Majjane, A. Chahine, M. Et-tabirou, B. Echchahed, T. O. Do, P. Mc Breen, Mater. Chem. Phys., 2014, **143**, 779-787.

2. S. Rada, M. Culea, M. Rada, E. Culea, J. Mater. Sci., 2008, **43**, 6122-6125.

3. A. Bianconi, A. Giovannelli, I. Davoli, S. Stizza, L. Palladino, O. Gzowski, L. Murawski, Solid State Commun., 1982, **42**, 547-551.

4. N. Vedeanu, O. Cozar, I. Ardelean, S. Filip, J. Optoelectron. Adv. M., 2006, **8-3**, 1135-1139.

5. A. H. Hammad, A. M. Abdelghany, J. Non Cryst. Solids, 2016, **433**, 14-19.

6. P. Hejda, J. Holubová, Z. Černošek and E. Černošková, J. Non Cryst. Solids, 2017, **462**, 65-71.

7. J. E. Garbarczyk, M. Wasiucionek, P. Machowski, W. Jakubowski, Solid State Ion, 1999, **199**, 9-14.

8. C. Cramer, K. Funke, B. Roling, T. Saatkamp, D. Wilmer, M. D. Ingram, A. Pradel, M. Ribes, G. Taillades, Solid State Ion., 1996, **86-88**, 481-486.

9. J. J. D. Marin, PhD thesis, São Carlos: UFSCar, 2016, 93 p.

10. A. Feltz, B. Unger, J. Non Cryst Solids, 1985, **72**, 335-343.

11. T. Ishiyama, S. Suzuki, J. Nishii, T. Yamashita, H. Kawazoe, T. Omata, J. Electrochem. Soc., 2013, **160**, E143-E147.

12. T. Ishiyama, S. Suzuki, J. Nishii, T. Yamashita, H. Kawazoe, T. Omata, Solid State Ion., 2014, **262**, 856-859.

13. Y. Abe, D. E. Clark, J. Mater. Sci. Lett., 1990, **9**, 244-245.

14. Y. Goto, K. Taniguchi, T. Omata, S. Otsuka-Yao-Matsuo, N. Ohashi, S. Ueda, H. Yoshikawa, Y. Yamashita, H. Oohashi and K. Kobayashi, Chem. Mater., 2008, **20**, 4156-4160.

15. D. Fang, F. He, J. Xie and L. Xue, Journal Wuhan University of Technology, Materials Science Edition, 2020, **35**, 711-718.

16. M. C. Ungureanu, M. Levy, J. L. Souquet, Ceram. – Silik, 2000, **44 (3)**, 81-85.

17. X. Lu, L. Deng, S. A. Saslow, H. Liu, C. J. Benmore, B. P. Parruzot, J. T. Reiser, S. H. Kim, J. V. Ryan, J. D. Vienna, J. Du, J. Phys. Chem. B, 2021, **125**, 12365-12377.

18. I. M. Batyaev, S. V Linnikov, A. L. Lipatova, Tech. Phys. Lett., 2003, **29**, 327-328.

19. C. Mercier, G. Palavit, L. Montagne and C. Follet-Houttemane, C. R. Chimie, 2002, **5**, 693-703.

20. D. Ehrt, M. Leister, A. Matthai, C. Rüssel, F. Breitbarth, Proceedings of Fundamentals in Glass Science and Technology, Vaxjo, Sweden, 1997, 204–211.

21. T. Yamaguchi, S. Tsukuda, T. Ishiyama, J. Nishii, T. Yamashita, H. Kawazoe, T. Omata, J. Mater. Chem. A, 2018, **6**, 23628-23637.

22. T. Yamaguchi, T. Ishiyama, K. Sakuragi, J. Nishii, T. Yamashita, H. Kawazoe and T. Omata, Solid State Ion., 2015, **275**, 62-65.

23. T. Omata, T. Yamaguchi, S. Tsukuda, T. Ishiyama, J. Nishii, T. Yamashita, H. Kawazoe, Phys. Chem. Chem. Phys., 2019, **21**, 10744-10749.

24. J. T. S. Irvine, D. C. Sinclair, A. R. West, Adv. Mater., 1990, **2**, 132-138.

25. J. R. Macdonald, J. Chem. Phys., 1974, **61**, 3977-3996.

26. D. S. Patil, K. Shimakawa, V. Zima, T. Wagner, J. Appl. Phys., 2014, **115**, 143707.

27. M. Wang, H. Bin Luo, S. X. Liu, Y. Zou, Z. F. Tian, L. Li, J. L. Liu, X. M. Ren, Dalton Transactions, 2016, **45**, 19466-19472.

28. M. Wasiucionek, J. E. Garbarczyk, P. Kurek, W. Jakubowski, Solid State Ion., 1994, **70/71**, 346-349.

29. J. E. Garbarczyk, P. Machowski, M. Wasiucionek, W. Jakubowski, Solid State Ion, 2003, **157**, 269-273.

30. J.E. Garbarczyk, P. Machowski, M. Wasiucionek, L. Tykarski, R. Bacewicz, A. Aleksiejuk, Solid State Ion., 2000, **136-137**, 1077-1083.

31. J. E. Garbarczyk, M. Wasiucionek, P. Machowski, W. Jakubowski, Solid State Ion, 1999, **199**, 9-14.

32. W. Lai, S. M. Haile, J. Am. Ceram. Soc., 2005, **88**, 2979-2997.

33. M. Du, K. Huang, Y. Guo, Z. Xie, H. Jiang, C. Li, Y. Chen, J. Power Sources, 2019, **424**, 91-99.

34. A. Mekki, G. D. Khattak, D. Holland, M. Chinkhota, L. E. Wenger, J. Non Cryst. Solids, 2003, **318**, 193-201.

35. A. Majjane, A. Chahine, M. Et-Tabirou, B. Echchahed, T. O. Do, P. M. Breen, Mater. Chem. Phys., 2014, **143**, 779-787.

36. G. Broglia, C. Mugoni, J. Du, C. Siligardi, M. Montorsi, J. Non Cryst. Solids, 2014, **403**, 53-61.

37. A. Chrissanthopoulos, C. Pouchan, G. N. Papatheodorou, Zeitschrift für Naturforschung A, 2014, **56**, 773-776.

38. N. Vedeanu, O. Cozar, I. Ardelean, S. Filip, J. Optoelectron. Adv. M., 2006, **8-3**, 1135-1139.

39. M. Saad, W. Stambouli, N. Sdiri, H. Elhouichet, Mater. Res. Bull., 2017, **89**, 224-231.

40. R. K. Brow, J. Non Cryst. Solids, 2000, **263-264**, 1-28.

41. R. K. Brow, D. R. Tallant, J. J. Hudgens, S. W. Martin and A. D. Irwin, J. Non Cryst. Solids, 1994, **177**, 221-228.

42. A. Chrissanthopoulos, C. Pouchan, G. N. Papatheodorou, Zeitschrift für Naturforschung A, 2014, **56**, 773-776.

43. A. Naruse, Y. Abe and H. Inoue, J. Ceram. Assoc. Jpn., 1968, **76**, 36.

44. R. T. Rasheed, H. S. Mansoor, T. A. Abdullah, T. Juzsakova, N. Al‑Jammal, A. D. Salman, R. R. Al‑Shaikhly, P. C. Le, E. Domokos, T. A. Abdulla, J. Therm. Anal., 2021, **145**, 297-307.

Chapter 5 Experimental Investigation of Effect of Ga₂O₃ Addition on Proton Mobility and Thermal Stability in Proton-Conducting Phosphate Glasses

5-1 Introduction

The incorporation of WO_3 and $VO_{5/2}$ into glass compositions has been found to strengthen the cross-linking between phosphate chains, thereby enhancing thermal stability. When WO_3 content is increased, it facilitates cross-linking between the phosphate chains by incorporating WO_6 octahedra. This results in the formation of bonding structures that involve heteroatomic P−O−W linkages, specifically ≡P−O−W−O−P≡ bonds. These linkages contribute to an increase in the glass transition temperature (T_g) with increasing WO_3 content, indicating improved thermal stability. The increased proton mobility (μ_H) at T_g can be attributed to a reduction in the energy barrier for inter-phosphate chain proton migration. The formation of P−O−W linkages facilitates proton migration by creating additional migration paths for proton conduction. This increase in migration pathways is associated with the presence of non-bridging oxygen (NBO) sites associated with WO_6 octahedral units. The NBO sites associated with WO_6 octahedral units provided favorable environments for proton transport within the glass structure, resulting in enhanced proton mobility and conductivity. On the other hand, the incorporation of V_2O_5 into the glass composition improves thermal stability, as indicated by the high T_g. This enhancement in thermal stability can be attributed to the formation of strong cross-linkages between the phosphate ion chains through the introduction of P−O−V heteroatomic linkages. These linkages involve 6-fold coordinated vanadium (V) atoms, which tightly bridge the phosphate chains and contribute to a more rigid and robust glass structure. However, the addition of V_2O_5 negatively affects proton mobility within the glass. Protons tend to be trapped at the oxygen sites of the VO_x polyhedra, resulting in increased proton dissociation energy. Consequently, the proton mobility within the glass is low, leading to low proton conductivity. Specifically, I investigated the influence of WO_3 and V_2O_5 as conditional glass formers. While both oxides have shown similarities in enhancing thermal stability, their effects on proton mobility were found to be distinct. In this chapter, my research aimed to explore the potential of Ga_2O_3 as a conditional glass former and investigate its effect on both thermal stability and proton mobility. Ga_2O_3 has been widely recognized for its ability to create strong cross-linkages between phosphate chains, which in turn enhances the T_g of the resulting glass [1-3]. One interesting aspect of GaO_6, the structural unit of Ga_2O_3, is the absence of non-bridging oxygen (NBO) sites [4]. However, the lower electronegativity of gallium (1.79) compared to other elements such as vanadium (1.91) and tungsten (2.08) [5] suggests that the nature of the O−H bonds in −Ga−O−P−O−H linkages may exhibit increased ionic character, owing to high ionicity of Ga−O bond, consequently the covalency of the P–O bonds increases. This variation in bonding properties has the potential to significantly influence the overall behavior of the glass system. Therefore, I specifically selected Ga_2O_3 as a candidate for my study to investigate its role as a conditional glass former.

Previous studies on xGa$_2$O$_3$−(100−x)NaPO$_3$ have reported that Ga ions tend to exhibit a high coordination number of 6, particularly in low Ga$_2$O$_3$ content glasses up to 6-7 mol% [1]. Despite this high coordination, T_g of these compositions has been found to vary within a range of 280-380 °C [1]. Therefore, it is essential to use glasses with a glass transition temperature (T_g) of at least 400 °C for the APS. This is because the T_g of the glasses decreases significantly around 150-200 °C after APS [6], and there is a high possibility that the glasses will crystalize since APS temperature might exceed the crystallization temperature (T_c) of the glasses. Therefore, to further enhance T_g and enable the conduction of APS, I incorporated GeO$_2$ and NbO$_{5/2}$ oxides into the compositions containing a maximum of 6 mol% GaO$_{3/2}$ [7-8]. This approach not only aimed to enhance T_g but also expanded the dataset for future statistical analysis, providing a comprehensive understanding of the system.

In this chapter, the focus of the experimental investigation was to examine the effect of GaO$_{3/2}$ addition on thermal stability and proton mobility in 30HO$_{1/2}$−xGaO$_{3/2}$−6NbO$_{5/2}$−(6−x)GeO$_2$−58PO$_{5/2}$ (x = 0, 2, 4, and 6) glasses, referred to as xGa-glass. The results of the experiments confirmed that substituting GeO$_2$ with GaO$_{3/2}$ resulted in an increase in both the T_g and μ_H at T_g. To gain a deeper understanding of these effects, the structure of the glasses and the characteristics of O−H and P−O bonds were analyzed. Similar to the influence of WO$_3$ and VO$_{5/2}$, the observed increase in T_g was attributed to the presence of P−O−Ga linkages that formed strong cross-linking between the phosphate chains. However, unlike the case of WO$_3$, the enhanced proton mobility was not due to a decrease in the migration barrier caused by an increased number of proton migration paths through non-bridging oxygens (NBOs) of WO$_6$ octahedra. In the case of GaO$_{3/2}$, infrared (IR) spectra results indicated the presence of strong O−H bonding, suggesting limited proton mobility as GaO$_{3/2}$ was substituted with GeO$_2$. Conversely, X-ray photoelectron spectroscopy (XPS) analysis of the P 2p core level revealed that the P−O bonding became more covalent with the substitution of GaO$_{3/2}$ with GeO$_2$. This observation implied that the O−H bond in −Ga−O−P−O−H linkages became more ionic, resulting in reduced proton dissociation energy and thus higher proton mobility. Although the IR and P 2p core level XPS results appeared contradictory, with the exact reason for the experimentally observed enhanced proton mobility not yet fully understood, the IR results provided direct evidence of the nature of O−H bonding. Therefore, it was concluded that the reduced activation energy (E_a) resulted from a decreased migration energy based on the proton hopping mechanism.

5-2 Experimental

5-2-1　Preparation of precursor glasses

I prepared precursor glasses of 30NaO$_{1/2}$−xGaO$_{3/2}$−6NbO$_{5/2}$−(6−x)GeO$_2$−58PO$_{5/2}$ (x = 0, 2, 4, and 6) using reagent-grade chemicals purchased from FUJIFILM Wako Chemicals, Japan, through a standard melt quenching method. Stoichiometric amounts of Na$_2$CO$_3$, Ga$_2$O$_3$, Nb$_2$O$_5$, GeO$_2$, and H$_3$PO$_4$ (aq. 85%) were thoroughly mixed and melted at 1400 °C for 1 hour in an air atmosphere, utilizing a platinum
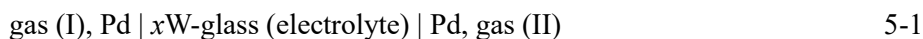
crucible. The molten mixture was then poured into carbon molds and annealed at 450 °C for 20 minutes. Subsequently, the glasses were cooled slowly to room temperature at a rate of 20 °C per hour. Henceforth in this chapter, the glasses will be referred to as 0Ga, 2Ga, 4Ga, and 6Ga for ease of discussion.

5-2-2 Proton injection by APS

To facilitate proton injection, the cylindrical-shaped precursor glass obtained after annealing was cut into 0.8 mm thick disks with an 18 mm diameter as shown in Figure 3-2 (a) in chapter 3. A 100 nm thick palladium (Pd) thin film was deposited on one surface of the disk using magnetron sputtering (JFC-1600, JEOL, Japan). The disk, with the Pd-film side facing upwards, was placed in a sample holder where the other side was in contact with a molten tin cathode in an H_2 atmosphere. I performed APS on all four glasses by applying a DC voltage of 10 V in the temperature range of 333 °C for 8-10 hours using the apparatus as shown in Figure 3-2 (b) in chapter 3. Detailed information about the APS apparatus and working conditions can be found in chapter 1 [9-10]. I checked the glass nature of the specimens after APS by conducting X-ray diffraction (XRD) using Cu Kα radiation (SmartLab, Rigaku, Japan).

5-2-3 Electrical properties

To evaluate the electrical properties, disk-shaped glasses were used. Gold (Au) thin-film electrodes with a thickness of 200 nm were deposited on both surfaces of the disk using magnetron sputtering. I employed an AC impedance method and an impedance analyzer (ModuLab, Solartron Analytical, UK) to measure the electrical conductivity in a dry 5% H_2/95% N_2 atmosphere. The mean transport number of protons in the glasses was determined by measuring the electromotive force (EMF) of a hydrogen concentration cell:

$$\text{gas (I), Pd} \mid x\text{W-glass (electrolyte)} \mid \text{Pd, gas (II)} \qquad 5\text{-}1$$

In gas (I), the hydrogen partial pressure was regulated at 1 atm through the continuous flow of H_2 gas, while in gas (II), the hydrogen partial pressure was controlled by diluting H_2 with N_2.

5-2-4 Characterization

For characterization purposes, I determined the glass transition temperature (T_g) using thermomechanical analysis (TMA) with a TD5000SA instrument (Bruker AXS, US). The test samples were subjected to an applied load of 68 mN mm^{-2}, and the temperature was increased at a rate of 20 °C min^{-1}. The sodium concentrations (C_{Na}) in the glass before and after APS were determined using an energy dispersive X-ray spectrometry (EDX) system (JED 2300, JEOL, Japan) integrated into a field emission scanning electron microscopy (FE-SEM) instrument (SU6600, Hitachi, Japan). Fourier-

transform infrared spectroscopy (FT-IR; FT/IR-6100, JASCO, Japan) was employed to obtain infrared absorption spectra in the O−H stretching vibration region (v_{OH}) for evaluating O–H bonding characteristics and the concentration of OH groups corresponding to proton concentration. The concentration of OH groups, denoted as C_{OH} and measured in cm^{-3}, was determined from the maximum absorption intensity v_{OH} ($\alpha(v_{OH})$), by employing Equation 5-2 [11]:

$$C_{OH} = 1.03 \times 10^{19} \times \alpha(v_{OH}) \qquad\qquad 5\text{-}2$$

Raman spectra were obtained using a laser Raman spectrometer (NRS-3100, JASCO, Japan) with an excitation wavelength of 532 nm. The P 2p core level X-ray photoelectron spectra (XPS) were examined using a PHI5600 spectrometer (ULVAC-PHI Inc., Japan) equipped with a hemispherical electron analyzer. Excitation was achieved using monochromatic Al-Kα radiation (hv=1486.6 eV) as the source. To ensure surface integrity, all glass samples were prepared under a dry N_2 atmosphere and scraped to expose a fresh surface immediately prior to analysis. The samples were then placed on a gastight sample holder and loaded into the preparation chamber of the XPS apparatus, ensuring no exposure to air. During spectra recording, the residual pressure in the analyzing chamber was maintained at approximately 5×10^{-7} Pa. The binding energy of the system was calibrated at 284.8 eV using the C 1s core level for reference to account for residual carbon contamination [12-13].

5-3 Results and discussion

5-3-1 Proton injection by APS

Figure 5-1 (a) illustrates the depth profiles of Na and OH concentrations (C_{Na} and C_{OH}) in the 0Ga-glass before and after APS (dashed lines). Following APS, more than 95% of Na ions were discharged from the glass, while a substantial amount of OH was introduced into the glass. The absolute changes, ΔC_{Na} and ΔC_{OH}, were both determined to be -7.4×10^{21} cm^{-3} and 6.7×10^{21} cm^{-3}, indicating the successful electrochemical substitution of Na^+ ions with protons. The concentration profiles of Na and OH, denoted as C_{Na} and C_{OH} respectively, were analyzed in the 2Ga, 4Ga, and 6Ga-glasses both before and after APS, as shown in Figure 5-1 (b), (c), and (d) respectively. After-APS, it was observed that over 95% of Na ions were discharged from the glass, while a considerable amount of OH was introduced into the glass. The absolute changes, ΔC_{Na} and ΔC_{OH}, in these glasses exhibited slight variations, indicating that the 2Ga, 4Ga, and 6Ga-glasses after APS did not possess the same OH concentration as the Na ion concentration in the glass before APS. Nonetheless, the depth profiles of C_{Na} and C_{OH} indicated the successful electrochemical substitution of Na^+ ions with protons. XRD analysis confirmed that all after APS specimens remained in a glassy state as shown in Figure 5-2. Thus, successful synthesis of $30HO_{1/2}-xGaO_{3/2}-6NbO_{5/2}-(6-x)GeO_2-58PO_{5/2}$ (x = 0, 2, 4, and 6) was achieved through APS. After APS, all the glasses exhibited a colorless appearance.
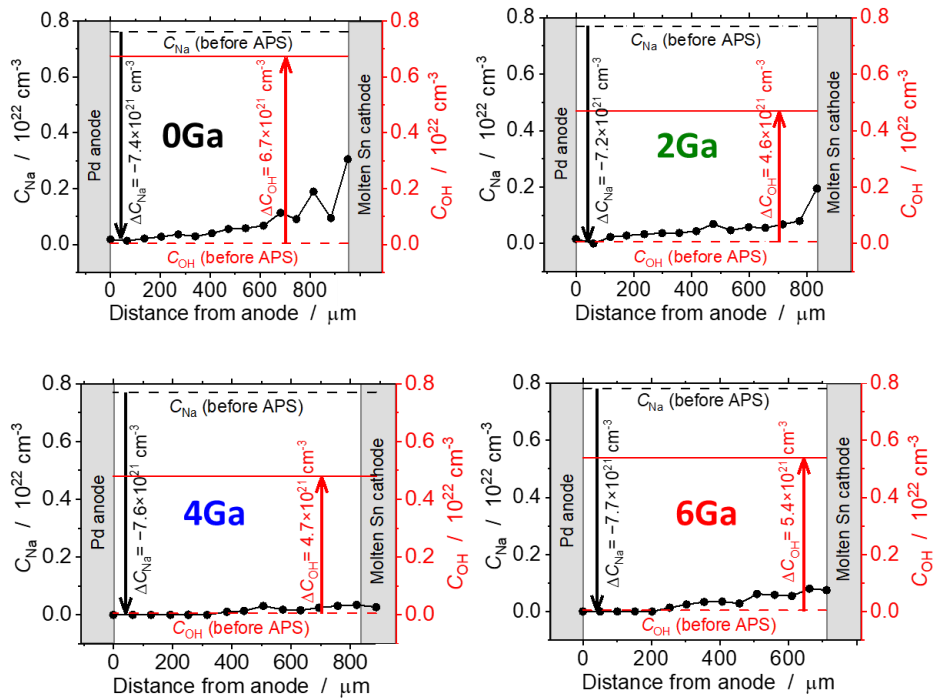
Figure 5-1 Depth profiles for glass (a) 0Ga, (b) 2Ga, (c) 4Ga and (d) 6Ga of C_{Na} (black dots) and C_{OH} (red solid line) for xGa-glass after alkali-proton substitution (APS). The black and red dashed lines indicate C_{Na} and C_{OH}, respectively, for the xGa-glass before APS.

5-3-2 Thermal stability

Figure 5-3 illustrates the relationship between the glass transition temperature (T_g) and the content of GaO$_{3/2}$ in the glasses. The data demonstrates that T_g slightly increased from 204 to 208 °C as the GaO$_{3/2}$ content increases, indicating that the substitution of GeO$_2$ with GaO$_{3/2}$ enhances the thermal stability of the glasses. However, it is important to consider the effect of decreasing GeO$_2$ since GeO$_2$ is known to enhance T_g. Predictive analysis suggests a 0.6 °C decrease in T_g for every 1 mol% decrease in GeO$_2$ [14]. Considering the substitution from 6 to 0 mol% GeO$_2$, a reduction of 3.6 °C in T_g should be taken into account. Therefore, it can be concluded that the addition of GaO$_{3/2}$ indeed enhances T_g and provides high thermal stability to the glasses. This phenomenon of increased T_g has been reported in various phosphate glasses and is attributed to the formation of heteroatomic P−O−Ga bonds, which create strong cross-links between the phosphate glass networks [1,4] and as also in the case of WO$_3$ and V$_2$O$_5$. As a result, the enhanced T_g observed in our glasses with higher GaO$_{3/2}$ content can be attributed to the formation of P−O−Ga linkages. Further insights into the glass structure will be discussed based on Raman spectra.
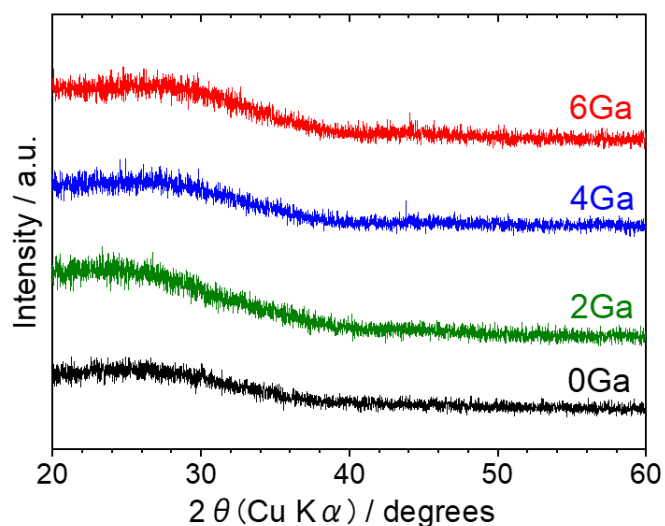
Figure 5-2 XRD patterns of the *x*Ga glasses after APS.
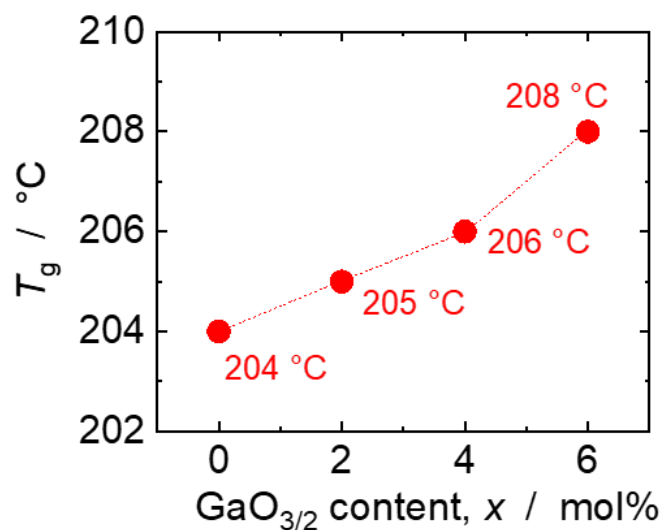
Figure 5-3 Variation of the glass transition temperature (T_g) of the glasses after alkali-proton substitution (APS) as a function of the GaO$_{3/2}$ content (x).

5-3-3 Proton conductivity

Figures 5-4 present the results of electromotive force (EMF) measurements conducted on hydrogen concentration cells, using glasses as electrolytes after APS. The measurements were carried out at a temperature of 260 °C. The proton transport numbers (t_H) obtained from these measurements are summarized in Table 5-1. The results indicate that all the glasses exhibit a t_H value of unity, indicating that all the glasses are pure proton-conducting electrolytes.
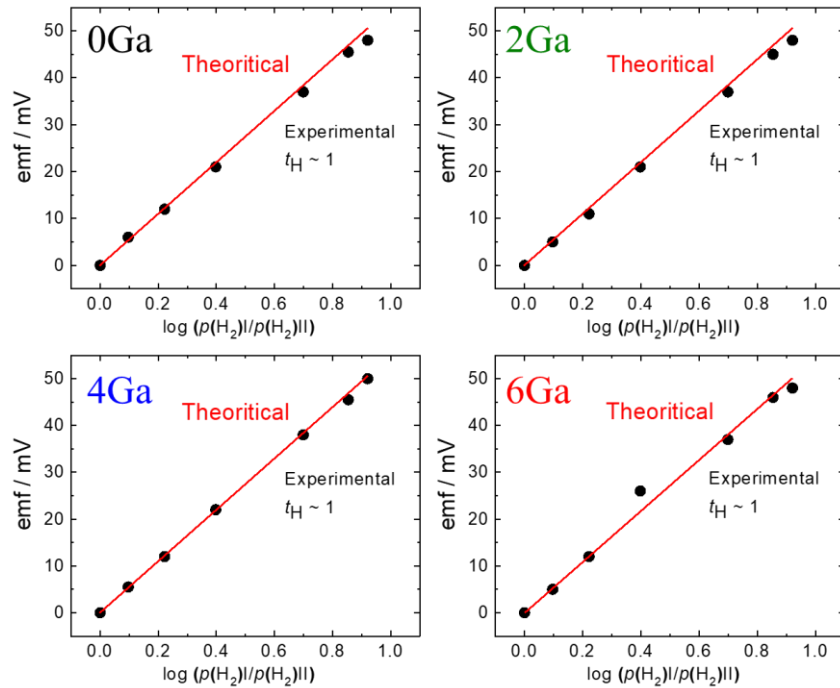
Figure 5-4 Electromotive forces (EMFs) for the hydrogen concentration cell as a function of logarithmic hydrogen partial pressure, $p(H_2)$, ratio at 260 °C for xGa glass after alkali-proton substitution (APS). The theoretical emfs calculated using the Nernst equation, E= $(RT/2F)$ ln(p(H$_2$)$_{high}$/p(H$_2$)$_{low}$) are shown as red lines.

Table 5-1 Proton transport number (t_H) at 260 °C of the xGa-glasses after alkali-proton substitution (APS) determined by measuring the electromotive force (EMF) of the hydrogen concentration cells.

Glass	Proton transport number, t_H
0Ga	1
2Ga	1
4Ga	1
6Ga	1

Figure 5-5 illustrates the Arrhenius plot of the proton conductivity for the glasses. The proton conductivity corresponds to the total conductivity observed in all the glasses. The measured proton conductivity ranges from 10^{-8} to 10^{-4} S cm^{-1} over a temperature range of 120 °C to 320 °C. Throughout this temperature range, the conductivities of all the glasses remain within the same order of magnitude. Although no significant variation in conductivity based on GaO$_{3/2}$ content is observed, the activation energy (E_a) for proton hopping conduction, obtained from the ln(σT) vs. $1/T$ plot, gradually decreases from 1.17 to 1.05 eV as the GaO$_{3/2}$ content increases from 0 to 6 mol% (Figure 5-6a). Figure 5-6b displays the proton mobility (μ_H) at the glass transition temperature (T_g), which is calculated from the proton conductivity at T_g and the proton carrier density (n_H) assuming that all protons forming OH groups are mobile (n_H=C_{OH}). The data clearly demonstrates that log (μ_H at T_g [cm^2 V^{-1} s^{-1}]) increased from −9.23 to −8.57 as the GaO$_{3/2}$ content increases from 0 to 6 mol%. Considering the substitution of

$GaO_{3/2}$ with GeO_2, which affects proton mobility, a predicted decrease of 0.12 in log (μ_H at T_g [cm^2 V^{-1} s^{-1}]) is observed for every 1 mol% decrease in GeO_2 [14]. With the substitution from 6 to 0 mol% GeO_2, a reduction of 0.72 is expected. Therefore, it can be concluded that the addition of $GaO_{3/2}$ significantly enhances μ_H at T_g. The reduction in E_a and increased μ_H at T_g indicate a reduction in the energy barrier for proton conduction as the $GaO_{3/2}$ content increases.
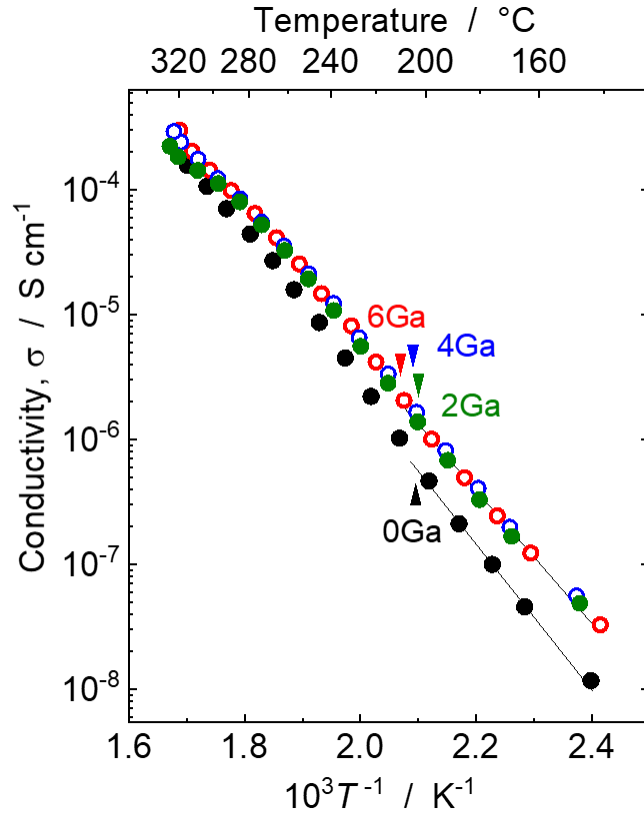
Figure 5-5 Arrhenius plot of the proton conductivity of the *x*Ga-glasses after alkali-proton substitution (APS). The triangles correspond to the proton conductivities at the glass transition temperature (T_g) of each glass.
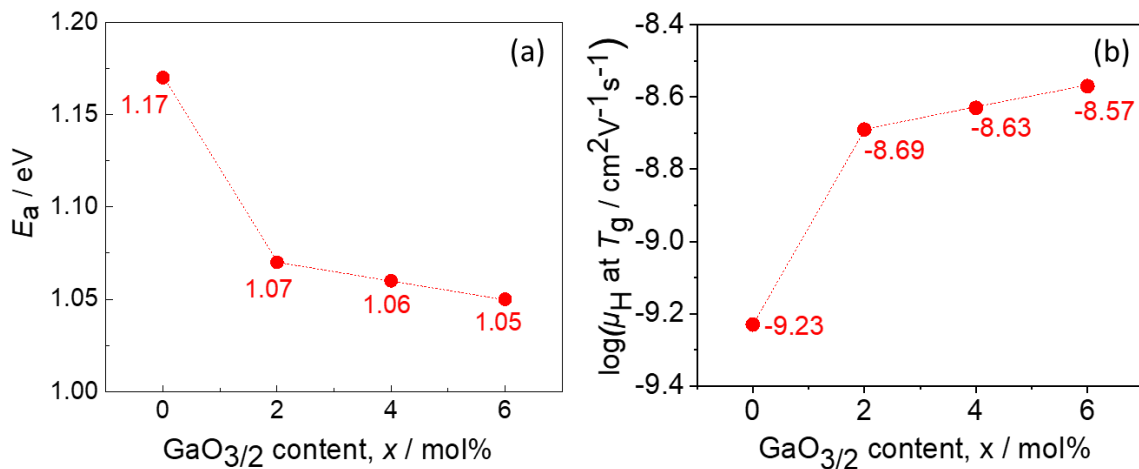
Figure 5-6 Variation of (a) activation energy (E_a) of the proton conduction, and (b) proton mobility (μ_H) at the glass transition temperature (T_g) as a function of the $GaO_{3/2}$ content (*x*).

In summary, the experimental findings demonstrate that the substitution of $GaO_{3/2}$ with GeO_2 in phosphate glasses enhances their thermal stability and proton mobility, resulting in improved proton conductivity. Both T_g and μ_H at T_g increased with higher $GaO_{3/2}$ content. These results suggest that $GaO_{3/2}$ is a suitable oxide component for enhancing the properties of proton-conducting phosphate glasses.

5-4 Origin of enhanced thermal stability and proton mobility

5-4-1 Thermal stability

The Raman spectra of the glasses after APS, as shown in Figure 5-7 and summarized in Table 5-2 [15-22], provide significant insights into the glass structure characteristics of the xGa-glasses. The prominent bands observed in the range of 900-1000 cm^{-1} correspond to the stretching modes of Nb−O bonds (v_{NbO^-}), indicating the presence of NbO_6 octahedra. The bands located around ~700 cm^{-1} and ~1200 cm^{-1} are attributed to the symmetric stretching vibrations of the P−O−P bond for the Q^2 unit ($v_{sym}(P-O-P)Q^2$) and the symmetric stretching vibrations of the O−P−O bond for the Q^2 unit ($v_{sym}(PO_2)Q^2$), respectively. These spectral features primarily represent the phosphate framework of the glasses. The consistent wavenumber of the ($v_{sym}(P-O-P)Q^2$) and ($v_{sym}(PO_2)Q^2$) bands across all the glasses, despite varying $GaO_{3/2}$ and GeO_2 content, indicates that the length of the phosphate chain remains unchanged. In the glass 0Ga, 2Ga, and 4Ga, a small shoulder observed at 800 cm^{-1}. The intensity of this shoulder decreases with the decreasing GeO_2 content in the glasses and finally disappears in 0 mol% GeO_2, i.e., 6Ga glass. This shoulder can be attributed to the stretching vibration of the P–O–Ge bond ($v_{(P-O-Ge)}$). In the 2Ga, 4Ga, and 6Ga glasses, an additional band at approximately 360 cm^{-1} is observed, which is attributed to the symmetric bending vibrations of Ga–O–P linkages. Furthermore, the band at 320 cm^{-1}, detected in the spectra of the 2Ga, 4Ga, and 6Ga glasses, is attributed to GaO_6 vibrational groups. These findings suggest the incorporation of GaO_6 units into the glass structure. Notably, despite the presence of $GaO_{3/2}$, there is no indication of the formation of homoatomic Ga−O−Ga linkages in any of the glasses. Instead, the preference for heteroatomic P−O−Ga linkages, as reported in previous studies, is confirmed. This indicates that the introduction of $GaO_{3/2}$ into the glass composition promotes the formation of strong bonds between phosphate chains, contributing to the structural stability of the glasses.

The substitution of GeO_2 with $GaO_{3/2}$ in the glasses introduces changes in the structural composition that need to be considered. Ge atoms in the 0Ga, 2Ga, and 4Ga glasses are six-fold coordinated with oxygen atoms, forming strong heteroatomic P–O–Ge linkages [7]. These linkages play a crucial role in bridging the $(PO^{3-})_l$ phosphate chains and contribute to the formation of rigid phosphate frameworks, resulting in higher T_g. When $GaO_{3/2}$ replaces GeO_2, it is expected that the P–O–Ge heteroatomic linkages will be reduced. This substitution could potentially weaken the phosphate frameworks and lead to a decrease in T_g. However, the observed increase in T_g, even if only slight, suggests that the introduction

of Ga ions results in stronger cross-linking of the phosphate chains compared to Ge ions. The increasing $GaO_{3/2}$ reinforces the structural integrity of the glasses, potentially through the formation of strong heteroatomic P–O–Ga linkages. These linkages contribute to the enhanced cross-linking between the phosphate chains, leading to a more robust glass structure. This contributes to the increased T_g and improved thermal stability of the glasses.
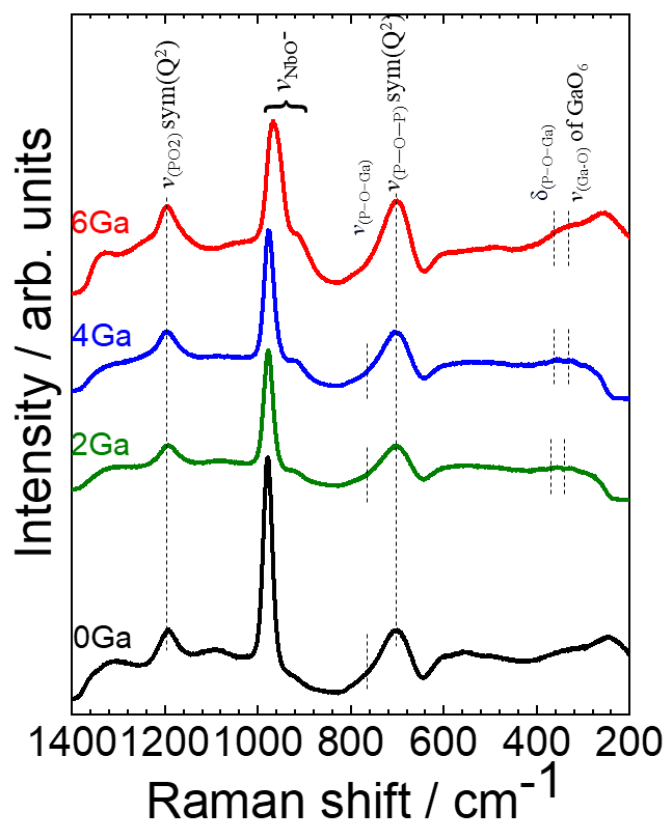

Figure 5-7 Raman spectra of the xGa-glasses after alkali-proton substitution (APS).

Table 5-2 Assignment of the Raman bands observed for xGa-glass after alkali-proton substitution (APS).

Assignment	Position / cm^{-1}					Ref.
	0Ga	2Ga	4Ga	6Ga		
ν_{Ga-O} of GaO_6	-	326	326	326	GaO_6 vibrational groups	15-16
δ_{P-O-Ga}	-	358	358	358	Symmetric bending vibrations of Ga–O–P linkages	15-16
$\nu_{P-O-P,\ sym}$ (Q^2)	701	701	701	701	Symmetric stretching mode of the P–O–P bond for the Q^2 unit	17-18
ν_{P-O-Ge}	793	792	791	-	Symmetric stretching vibrations of Ge–O–P linkages	19-20
ν_{Nb-O^-}	-, 978	923, 977	918, 976	913, 965	Stretching mode of the Nb–O$^-$ bond of NbO$_6$ octahedra	21-22
$\nu_{O-P-O,\ sym}$ (Q^2)	1195	1195	1195	1195	Symmetric stretching mode of NBOs for the Q^2 unit	17-18

5-4-2　Proton mobility

Based on the hopping mechanism, the activation energy (E_a) can be expressed as the sum of two contributions: the energy barrier (E_d) for proton dissociation from the O−H bonding and the energy barrier (E_m) for proton migration, as represented by Equation (5-3) [23].

$$E_a = E_d + E_m \tag{5-3}$$

To determine the dominant contribution responsible for the observed reduction in E_a upon replacing GeO_2 with $GaO_{3/2}$ (as depicted in Figure 5-9), I first investigated O−H stretching vibration that reflect O−H bond strength affecting E_d.

Figure 5-8 presents the infrared (IR) spectra in the OH stretching vibration region (ν_{OH}) of the xGa-glasses after the APS. By substituting $GaO_{3/2}$ with GeO_2, changes in the peak positions are observed. Specifically, the peak shifts from 2627 cm^{-1} in the 0Ga glass to 2659 cm^{-1} in the 2Ga glass and exhibits a slight increase from the 2Ga to the 6Ga glass. These observations suggest that the substitution of 2 mol% $GaO_{3/2}$ with GeO_2 results in the strengthening of the O−H bond, while the substitution from 2 mol% to 6 mol% leads to only a slight strengthening of the O−H bond. Typically, a band at such lower wavenumbers is associated with the ν_{OH} vibrations of the OH groups present in Q^2 units, which correspond to the internal PO_4 units within $(PO_3^{3-})_l$ chains [24]. Therefore, the IR spectra results indicate strong proton trapping by oxygen atoms and, consequently, an increase in proton dissociation energy with the increasing substitution of $GaO_{3/2}$ with GeO_2 content.

The nature of O−H bonding in proton-conducting phosphate glasses depends on the characteristics of P−O bonding. The extent of electron transfer between the phosphorus and oxygen atoms determines whether the P−O−H bond is ionic or covalent [7]. In cases where P−O bonding is highly ionic, the phosphorus atom donates electrons to the oxygen atom, thereby reducing the electron donation from the hydrogen atom to the oxygen atom. As a result, the excessive electron density on the oxygen atom is diminished, leading to a more covalent nature of the O−H bonding. Conversely, when P−O bonding is highly covalent, the O−H bonding becomes more ionic to maintain the appropriate electron density on the oxygen atom [25]. Consequently, the ν_{OH} band appears at a higher frequency when P−O bonding is ionic, indicating stronger O−H bonding. Conversely, in the case of highly covalent P−O bonding, the O−H bonding is weakened, resulting in the ν_{OH} band appearing at a lower frequency.

The P 2p core-level X-ray photoelectron spectroscopy (XPS) provides valuable insights into the ionicity or covalency of P−O bonds, offering a means to investigate the ν_{OH} band. Even slight variations in the nature of P−O bonding, leading to shifts in the frequency of the ν_{OH} band by tens of cm^{-1}, can be detected as peak shifts of 0.3 to 0.5 eV [7,26]. Figure 5-9 illustrates the changes in binding energy and full width at half maximum (FWHM) of the P 2p core-level peak, which consistently shift to lower binding energies with increasing substitution of $GaO_{3/2}$ with GeO_2. Specifically, the peak shifts from 134.97 eV in the 0Ga glass to 134.87 eV in the 4Ga glass, with a slightly larger increase of 0.1 eV observed from the 4Ga to the 6Ga glass. These observations indicate that the substitution of 2 mol% to

4 mol% of $GaO_{3/2}$ with GeO_2 results in a slight increase in the covalency of the P−O bond, while the substitution from 4 mol% to 6 mol% leads to a somewhat larger increase in covalency. In summary, these findings suggest a progressive shift towards a more covalent nature of the P−O bond with increasing $GaO_{3/2}$ content. Consequently, as the P−O bond becomes more covalent, the O−H bond becomes more ionic. This finding contrasts with the results obtained from the IR spectra, which directly indicate the nature of O−H bonding.
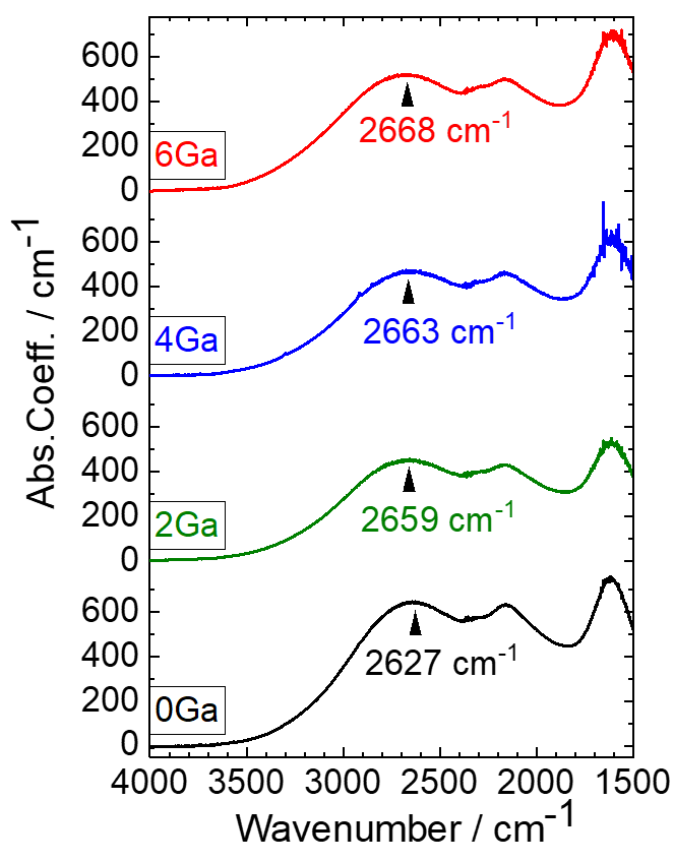
Figure 5-8 Infrared spectra in the ν_{OH} region of the xGa-glasses after alkali-proton substitution (APS).

With the slightly stronger O−H bonding nature with increasing substitution of GeO_2 with $GaO_{3/2}$ in xGa-glasses, the contribution of E_d in the proton hopping process slightly increased. Consequently, it can be concluded that the reduction in E_a with increasing $GaO_{3/2}$ content primarily arises from the decrease in E_m rather than E_d of the OH group. However, the contrasting results from the IR spectra and the P 2p core-level XPS analysis highlight the complexity of the bonding environment in these glasses. It suggests that the relationship between P−O bonding and O−H bonding is not straightforward and may involve other factors. Further investigations and a comprehensive understanding of the interplay between P−O bonding, O−H bonding, and their influence on proton conduction mechanisms are necessary.
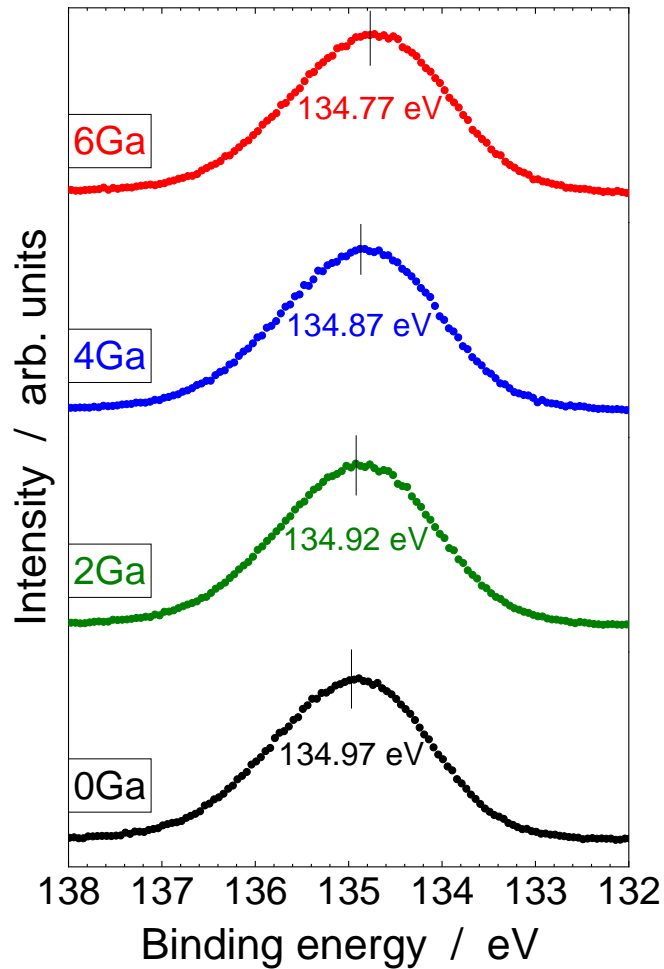
Figure 5-9 P 2p core-level X-ray photoelectron spectroscopy (XPS) spectra of the xGa-glasses after alkali-proton substitution (APS).

5-5 Conclusion

The effect of Ga_2O_3 on the T_g and μ_H at T_g was experimentally investigated in $30HO_{1/2}-xGaO_3-6NbO_{5/2}-(6-x)LaO_{3/2}-58PO_{5/2}$ glasses. The experimental investigation demonstrated that the substitution of GeO_2 with $GaO_{3/2}$ in phosphate glasses leads to enhanced glass transition temperature (T_g) and proton mobility (μ_H). The enhanced T_g can be attributed to the introduction of six-fold coordinated Ga atoms that tightly cross-link phosphate ion chains, forming P-O-Ga heteroatomic linkages. As a result, the T_g is increased due to the presence of a large number of P-O-Ga bonds. This increased covalency causes a rise in the ionicity of O-H bonds, weakening proton trapping and leading to increased proton mobility (μ_H). However, the inconsistency between the infrared (IR) and X-ray photoelectron spectroscopy (XPS) results regarding the nature of O-H bonding highlights the need for further research to fully understand this phenomenon. It was suggested that the enhanced proton mobility was due to a reduction in proton migration energy, although the exact mechanism is still unknown. Overall, the addition of $GaO_{3/2}$ exhibits positive effects on both T_g and μ_H, playing a role similar to

conditional glass formers such as WO_3, contributing to the formation of a three-dimensional network in the studied glasses. The observed enhancement in μ_H differs from the effect of WO_3 addition, suggesting distinct mechanisms at play.

References

1. A. Caron, B. Doumert, G. Tricot, Mater. Chem. Phys., 2014, **147**, 1165-1170.

2. U. Hoppe, D. Ilieva, J. Neuefeind, Z. Naturforsch., 2002, **57a**, 709-715.

3. P. Bet-thet, E. Bretey, J. Berthon, F. d'Yvoire, Solid State Ion., 1994, **70/71**, 476-481.

4. D. M. Pickup, R. M. Moss, D. Qiu, R. J. Newport, S. P. Valappil, J. C. Knowles, M. E. Smith, J. Chem. Phys., 2009, **130**, 064708.

5. J. C. A. Boeyens, Z. Naturforsch., 2008, **63b**, 199-209.

6. T. Yamaguchi, S. Tsukuda, T. Ishiyama, J. Nishii, T. Yamashita, H. Kawazoe, T. Omata, J. Mater. Chem. A, 2018, **6**, 23628-23637.

7. T. Omata, A. Sharma, T. Kinoshita, I. Suzuki, T. Ishiyama, S. Kohara, K. Ohara, M. Ono, T. Fang, Y. Ren, M. Fujioka, G. Zhao, J. Nishii, J. Mater. Chem. A, 2021, **9**, 20595-20606.

8. A. Senapati, S. K. Barik, R. V. Krishnan, S. Chakraborty, H. Jena, J. Therm. Anal., 2023, **148**, 355-369.

9. T. Ishiyama, S. Suzuki, J. Nishii, T. Yamashita, H. Kawazoe, T. Omata, J. Electrochem. Soc., 2013, **160**, E143-E147.

10. T. Ishiyama, S. Suzuki, J. Nishii, T. Yamashita, H. Kawazoe, T. Omata, Solid State Ion., 2014, **262**, 856-859.

11. Y. Abe, D. E. Clark, J. Mater. Sci. Lett., 1990, **9**, 244-245.

12. Y. Goto, K. Taniguchi, T. Omata, S. Otsuka-Yao-Matsuo, N. Ohashi, S. Ueda, H. Yoshikawa, Y. Yamashita, H. Oohashi, K. Kobayashi, Chem. Mater., 2008, **20**, 4156-4160.

13. D. Fang, F. He, J. Xie, L. Xue, J. Wuhan Univ. Technol. Mater. Sci. Ed., 2020, **35**, 711-718.

14. T. Omata, I. Suzuki, A. Sharma, T. Ishiyama, J. Nishii, T. Yamashita and H. Kawazoe, RSC Adv., 2021, **11**, 3012-3019.

15. G. L. Flower, M. S. Reddy, G. S. Baskaran, N. Veeraiah, Opt. Mater., 2007, **30**, 357-363.

16. A. Belke´bir, J. Rocha, A.P. Esculcas, P. Berthet, B. Gilbert, Z. Gabelica, G. Llabres, F. Wijzen, A. Rulmont, Spectrochim. Acta A Mol. Biomol. Spectrosc., 2000, **56**, 435-446.

17. R. K. Brow, J. Non Cryst. Solids, 2000, **263-264**, 1-28.

18. R. K. Brow, D. R. Tallant, J. J. Hudgens, S. W. Martin, A. D. Irwin, J. Non Cryst. Solids, 1994, **177**, 221-228.

19. L.Y. Zhang, H. Li b, L.L. Hu, J. Alloys Compd., 2017, **698**, 103-113.

20. Sundeep Kumar, S. Murugavel, K. J. Rao, J. Phys. Chem. B, 2001, **105**, 5862-5873.

21. M. G. Donato, M. Gagliardi, L. Sirleto, G. Messina, A. A. Lipovskii, D. K. Tagantsev, G. C. Righini, Appl. Phys. Lett., 2010, **97**, 231111.

22. A. El Jazouli, J. C. Viala, C. Parent, G. Le Flem, P. Hagenmuller, J. Solid State Chem., 1988, **73**, 433-439.

23. T. Ishiyama, T. Yamaguchi, J. Nishii, T. Yamashita, H. Kawazoe, T. Omata, J. Electrochem. Soc., 2022, **169**, 034517.

24. A. Naruse, Y. Abe, H. Inoue, J. Ceram. Assoc. Jpn., 1968, **76**, 36.

25. T. L. Barr, Modern Esca: The Principles and Practice of X-Ray Photoelectron Spectroscopy, 1994.

26. T. Yamaguchi, Y. Saito, Y. Kuwahara, H. Yamashita, T. Ishiyama, J. Nishii, T. Yamashita, H. Kawazoe, T. Omata, J. Mater. Chem. A, 2017, **5**, 12385-12392.

Chapter 6 Conclusions

In this thesis, the compositional dependence of log (μ_H at T_g) and T_g in proton-conducting phosphate glasses was investigated. A linear regression approach based on principal component analysis was employed to develop models for predicting μ_H at T_g and T_g across a wide range of glass compositions. The models, although lacking physical significance, provided valuable insights into the effects of individual component oxides on μ_H at T_g and T_g. The incorporation of specific conditional glass former oxides, namely WO_3, V_2O_5, and Ga_2O_3, has been found to significantly enhance either or both thermal stability and proton mobility of proton-conducting phosphate glasses.

The findings of this study can be summarized as follows:

Chapter 2, I utilized a linear regression approach based on principal component analysis to develop models that describe the compositional dependence of log (μ_H at T_g) and T_g for proton-conducting phosphate glasses. These models allowed us to predict μ_H at T_g and T_g for a wide range of phosphate glass compositions and revealed that the concentration of $HO_{1/2}$ and $PO_{5/2}$ had a primary influence on μ_H at T_g, with an increase in μ_H at T_g associated with higher $HO_{1/2}$ concentration and lower $PO_{5/2}$ concentration. The component oxides were categorized into three groups based on their effects on μ_H at T_g and T_g. Group 1 oxides ($HO_{1/2}$, MgO, BaO, $LaO_{3/2}$, and $BO_{3/2}$) acted as glass modifiers, increasing μ_H at T_g and decreasing T_g. Group 2 oxides (WO_3 and GeO_2) increased both μ_H at T_g and T_g. Group 3 oxides ($NbO_{5/2}$) increased T_g without significantly affecting μ_H at T_g. These insights are valuable for designing purpose-specific glasses, particularly in the field of proton-conducting phosphate glasses.

Chapter 3 experimentally investigated the effect of WO_3 on T_g and μ_H at T_g, confirming the predicted enhancement. The incorporation of WO_3 led to an increase in both T_g and μ_H at T_g. The increase in T_g was attributed to the formation of P−O−W linkages, which increased cross-linking within the glass network. The increase in μ_H at T_g was attributed to the reduction in the energy barrier for inter-phosphate chain proton migration facilitated by P−O−W linkages, which provided more migration paths for proton conduction.

Chapter 4 focused on the effect of incorporating $VO_{5/2}$ into the glass composition. The addition of $VO_{5/2}$ resulted in higher T_g due to the formation of tight cross-linkages between phosphate ion chains through P−O−V heteroatomic linkages via VO_6 octahedra units. However, it led to lower proton mobility due to strong proton trapping resulting from high proton dissociation energy. The difference in behavior between WO_3 and $VO_{5/2}$ can be attributed to the specific characteristics of non-bridging oxygen (NBOs) associated with each oxide.

Chapter 5 the experimental investigation conducted on the substitution of GeO_2 with $GaO_{3/2}$ results in enhanced both T_g and μ_H at T_g. The increased T_g is attributed to the introduction of six-fold coordinated Ga atoms, which effectively cross-link phosphate ion chains through P−O−Ga heteroatomic linkages. This structural modification leads to a higher number of P−O−Ga bonds, increasing the covalency within the glass and subsequently influencing the ionicity of O−H bonds. It is important to note that the

inconsistency observed between the infrared (IR) and X-ray photoelectron spectroscopy (XPS) results regarding the nature of O−H bonding necessitates further research for a comprehensive understanding of this phenomenon. It was suggested that the enhanced proton mobility was due to a reduction in proton migration energy, although the exact mechanism is still unknown. Overall, the addition of $GaO_{3/2}$ in the studied glasses has a positive effect on both T_g and μ_H at T_g, similar to conditional glass formers like WO_3. However, it is noteworthy that the observed enhancement in μ_H differs from the effect of WO_3 addition, suggesting distinct underlying mechanisms at play.

This thesis provides valuable insights into the compositional dependence of proton-conducting phosphate glasses. The developed models and experimental investigations shed light on the effects of various component oxides on μ_H at T_g and T_g. The choice of oxide components in proton-conducting phosphate glasses plays a crucial role in determining their properties. While WO_3 and Ga_2O_3 exhibit favorable characteristics as conditional glass formers, the inclusion of V_2O_5 units hinders proton mobility.

In light of the findings, future progress in this area could involve exploring the effects of additional conditional glass former oxides addition in the glass compositions and their interactions with other components in proton-conducting phosphate glasses. Investigating the glass structure and chemical characteristics of the resulting glasses would deepen the understanding of the mechanisms underlying enhanced thermal stability and proton mobility. Moreover, further exploration of the O−H bonding nature through advanced analytical techniques would contribute to the comprehensive understanding of proton conduction mechanisms in these glasses. The findings contribute for future advancements in glass design and contribute to the development of innovative materials for various proton-conductive applications.

Achievement List

(Papers submitted for publication on this study) Peer-reviewed.

1. "Understanding the effect of oxide components on proton mobility in phosphate glasses using a statical analysis approach" T. Omata, I. Suzuki, A. Sharma, T. Ishiyama, J. Nishii, T. Yamashita, H. Kawazoe, RSC Adv. 11, 3012−3019(2021). doi: 10.1039/D0RA10327F.

2. "Enhancing proton mobility and thermal stability in phosphate glasses with WO_3: The mixed glass former effect in proton conducting glasses", A. Sharma, I. Suzuki, T. Ishiyama, T. Omata, Phys. Chem. Chem. Phys., 2023, 25, 18766-18774, doi: 10.1039/D3CP01453C ("2023 Hot Article" award).

3. "Proton conductivity in vanadium phosphate glass after injecting high proton carriers` concentration: Investigating the effects on thermal stability, proton mobility, and suppressed electronic conductivity, A. Sharma, I. Suzuki, T. Omata, under preparation.

Publications：Others

4. "Investigating the role of GeO_2 in enhancing the thermal stability and proton mobility of proton-conducting phosphate glasses", T. Omata, A. Sharma, T. Kinoshita, I. Suzuki, T. Ishiyama, S. Kohara, K. Ohara, M. Ono, T. Fang, Y. Ren, M. Fujioka, G. Zhao, J. Nishii, J. Mater. Chem. A, 9, 20595−20606(2021). doi: 10.1039/D1TA04445A.

5. "Anhydrous silicophosphoric acid glass: Thermal properties and proton conductivity", T. Omata, A. Sharma, I. Suzuki, T. Ishiyama, S. Kohara, K. Ohara, M. Ono, Y. Ren, K. Zagarzusem, M. Fujioka, G. Zhao, J Nishii, ChemPhysChem, 23, e2021008 (2022). doi: 10.1002/cphc.202100840

List of Publications

(Presentations on this research at international conferences and symposium)

1. "Experimental study of the effect of WO_3 on proton mobility and thermal stability of proton conducting phosphate glasses", A. Sharma, I. Suzuki, T. Omata, 17th Asian Conference on Solid State Ionics (ACSSI-2020), Nagoya, Japan, September 12th, 2022. (Oral presentation)

2. "Experimental study of the effect of WO_3 on proton mobility and thermal stability of proton conducting phosphate glasses", A. Sharma, I. Suzuki, T. Omata, Korea-Japan Students' Symposium, November 14th, 2022. (Poster Presentation)

(Awards)

1. "2023 Hot Article" award for paper in Physical Chemistry Chemical Physics journal, Royal Society of Chemistry.
2. IMRAM Director award: Best poster (Dec 2022).
3. Prestigious Monbukagakusho (MEXT) scholarship award issued by Japanese Government (2020-2023, Japan).

Acknowledgement